

Do the Earth, Jupiter and Mercury cause the sunspots?

Lauri Jetsu ¹••

© The author(s) •••

Abstract The mainstream dynamo models predict that the sunspot cycle is stochastic. The official Solar Cycle Prediction Panel forecasts only the ongoing sunspot cycle because any forecast beyond one cycle is considered impossible. We analyse the sunspot data using the Discrete Chi-square Method (DCM), which can detect many periodic signals superimposed on an arbitrary trend. Our DCM model predictions are longer and more accurate than the official Solar Cycle Prediction Panel forecast. We detect the signals of planets, especially those of the Earth and Jupiter. If the Flux Transfer Events (FTE) of these planets cause the sunspots, there would be a relatively simple explanation for the sunspots cycles, the Hale's law, the differential rotation and many other phenomena observed in the Sun. Unfortunately, our study has become excessively long because the fighting against the mainstream windmills has taken its toll.

Keywords: Solar cycle, Observations - Sunspots, Statistics - Magnetic fields, Interplanetary

1. Introduction

Schwabe (1844) discovered the 10 years cycle in the number of sunspots. Wolf (1852) revised the cycle period to 11.1 years. This period is not constant but varies between 8 and 17 years (Lassen and Friis-Christensen, 1995). The amplitude of the sunspot number modulation follows a cycle of about 80 years (Gleissberg, 1945). All solar cycles have not been discovered from the sunspots, like the $P_{\text{Rieger}} = 154$ days Rieger cycle discovered from the solar flares (Rieger et al., 1984) and the 205 years Suess-de Vries cycle discovered from the terrestrial radiocarbon ^{14}C record (Wagner et al., 2001). These observations indicate that the sunspot data are multiperiodic. Multiple periods have been detected in the sunspot data with different time series analysis methods (Ohtomo et al., 1994; Zhu and Jia, 2018; Jayalekshmi, Pant, and Prince, 2022). There is no “phase-lock” in the observed sunspot cycle minimum and the maximum epochs (Weisshaar, Cameron, and Schüssler, 2023; Biswas et al., 2023). Such a “phase-lock” would not exist, if the sunspot data were multiperiodic.

The solar surface magnetic field is strongest in the sunspots. The polarity of this field is reversed at the beginning of each solar cycle. Therefore, the field geometry returns to its original state during the Hale cycle of about 22 years (Hale et al., 1919). One persistent solar cycle regularity has been the Gnevyshev–Ohl rule: every odd numbered sunspot cycle has had a higher amplitude than the preceding even numbered sunspot cycle (Gnevyshev and Ohl, 1948).

L. Jetsu
 lauri.jetsu@helsinki.fi

¹ Department of Physics, P.O. Box 64, FI-00014 University of Helsinki, Finland

Table 1. Recent prolonged periods of weak sunspot activity.

Minimum	Duration	Reference
Dalton	1790 - 1830	Komitov and Kaftan (2004)
Maunder	1640 - 1720	Usoskin, Solanki, and Kovaltsov (2007)
Spörer	1390 - 1550	Usoskin, Solanki, and Kovaltsov (2007)
Wolf	1270 - 1340	Usoskin, Solanki, and Kovaltsov (2007)
Oort	1010 - 1070	Usoskin, Solanki, and Kovaltsov (2007)

There have been prolonged periods when very few sunspots, or even none at all, were observed. The four most recent prolonged grand sunspot minima were identified by Usoskin, Solanki, and Kovaltsov (2007), who did not classify the Dalton minimum (Komitov and Kaftan, 2004) as a grand sunspot minimum. We give the epochs of these five most recent prolonged activity minima in our Table 1. The Earth's climate temperature rises during strong solar activity (e.g. Van Geel et al., 1999). Thus, the current prolonged solar activity minimum helps us to cope with the human-induced climate change.

Parker (1955) presented the dynamo model, where the solar magnetic field arises from interaction between internal differential rotation and convection. Babcock (1961) and Leighton (1969) presented the first models of how this dynamo may generate the sunspot cycle. In his review of the current dynamo models of the solar cycles, Charbonneau (2010) stated that all physical mechanisms causing the solar cycles are not yet fully understood. He noted that the physical processes regulating the magnetic amplitude of the solar cycle are still unknown. It is also not known how the sunspot-forming magnetic flux ropes are produced by the dynamo-generated mean magnetic field. Very recently, Vasil et al. (2024) proposed that the solar magnetic cycles are caused by a dynamo resulting from near-surface magneto-rotational instability.

The solar magnetic field is frozen-in the outward-streaming solar wind (Parker, 1958, Figure 6). Dungey (1961) presented the idea that the magnetic reconnection is the primary physical process in the interaction between the solar wind and the Earth's magnetosphere. The Earth's and the Sun's magnetic field lines reconnect intermittently on the dayside of the Earth during Flux Transfer Events (Russell, 2003; Kivelson and Bagenal, 2007, FTEs). These FTEs occur in bursts lasting on average about two minutes and having a repeat period of about eight minutes (Lockwood and Wild, 1993; Russell, 1995, 2003). In an FTE, the high-energy particles flow through the FTE magnetic flux rope, which acts like a portal connecting the Earth and the Sun (Glenn, 2019; Paul, Vaidya, and Strugarek, 2022). These FTE magnetic flux ropes show a tendency to form above the Earth's equator, from where they roll over the Earth's pole pointing away from the Sun, the winter pole (Raeder, 2006; Fear, Palmroth, and Milan, 2012; Nakariakov et al., 2016; Zhang et al., 2022). The FTEs are also observed in the magnetic fields of Mercury, Jupiter and Saturn (Sun et al., 2022). Many outstanding studies of the solar dynamo mention only the physical processes inside the Sun and therefore do not even mention the FTEs (e.g. Charbonneau, 2010; Vasil et al., 2024).

The official sunspot number forecast for the ongoing solar cycle 25 was made in the year 2019 by the Solar Cycle Prediction Panel, representing NOAA, NASA and the International Space Environmental Services (ISES). These forecasts are made only for one cycle at the time, because it is widely accepted that this stochastic variability is unpredictable beyond one solar cycle (Petrovay, 2020). Nevertheless, countless sunspot cycle predictions are constantly published (e.g. Asikainen and Mantere, 2023; Javaraiah, 2023; Krasheninnikov and Chumakov, 2023). The physical models for solar cycle prediction were recently reviewed by Bhowmik et al. (2023).

Wolf (1859) already argued that the variations in the sunspot cycle period may depend on Jupiter, Saturn, the Earth and Venus. There have been numerous attempts to find the connection between the planetary motions and the sunspot numbers (e.g. Schuster, 1911; Hantzsch, 1978). Recently, Stefani, Giesecke, and Weier (2019) formulated a solar-dynamo model, where planetary tidal forcing causes the sunspot cycle. Scafetta and Bianchini (2022) showed that the planetary tidal forces may alter the solar structure and cause the sunspot cycle. Charbonneau (2022) argued that the weak periodic tidal interaction signal of planets requires constant amplification because internal solar dynamo mechanisms can otherwise mask this signal.

The problem with the deterministic “planetary-influence-theory” is that long-term sunspot cycle predictions fail. At the moment, in the year 2024, the “solar-dynamo-theory” of a stochastic sunspot cycle is mainstream, while the “planetary-influence-theory” of a deterministic sunspot cycle is not. Here, we present successful deterministic sunspot number predictions, which are more accurate and extend over longer time intervals than the official Solar Cycle Prediction Panel forecast.

Section 2 describes the sunspot data. Section 3 introduces the Discrete Chi-square Method (DCM). Sections 4-6 present the results of our statistical DCM time series analysis of the sunspot data. Section 7 describes our combined statistical and astrophysical search for planetary signals. Section 8 presents our Discrete Fourier Transform (DFT) cross-check for the DCM signal detections. We discuss our results in Section 9 and draw our conclusions in Section 10.

2. Data

We retrieved the sunspot data from the Solar Influences Data Analysis Center¹ in December 2022. The monthly mean total sunspot number data begin in January 1749 and end to November 2022 (Table 2: $n = 3287$). After January 1818, the monthly mean standard deviation (S_i) of the input sunspot numbers from individual stations are available, as well as the total number of observations (N_i).

The yearly mean total sunspot number data begin in the year 1700 and end to 2021 (Table 3: $n = 322$). The S_i and N_i estimates are available after 1818.

The standard errors

$$\sigma_i = S_i / \sqrt{N_i} \quad (1)$$

for these data give the weights $w_i = \sigma_i^{-2}$. The normalised weights are

$$w_{\text{nor},i} = nw_i / \sum_{i=1}^n w_i. \quad (2)$$

If all errors were equal, the normalised weight $w_{\text{nor},i}$ for every observation would be one. For all monthly data, the normalised weights show that one observation out of $n = 2458$ observations has the largest weight $w_{\text{nor},\text{max}} = 381$ (Table 4, Line 1). The four most accurate, $N_{1/2} = 4$, observations influence the modeling more than the remaining $n - 4 = 2454$ observations. These monthly data statistics improve slightly if the more accurate data after the year 2000 are removed, which gives $N_{1/2} = 64$ for sample size $n = 2183$. All yearly data show an extreme case, $N_{1/2} = 1$, where the weight $w_{\text{nor},\text{max}} = 135$ of one observation exceeds the weight of all other $n - 1 = 203$ observations. Again, the statistics improve slightly if the more accurate data after the year 2000 are removed.

¹Source: WDC SILSO, Royal Observatory of Belgium, Brussels

Table 2. Times t_i of monthly mean total sunspot numbers y_i ($n = 3287$). The standard deviation (S_i) and the total number of estimates (N_i) are available from January 1818 onward. Values -1 indicate cases having no S_i and N_i estimate. This table shows only the first and the last lines, because all data is available in electronic form.

t_i (y)	y_i (-)	S_i (-)	N_i (-)
1749.042	96.7	-1	-1
...
2022.873	77.6	14.1	881

Table 3. Yearly mean total sunspot numbers ($n = 322$), otherwise as in Table 2

t_i (y)	y_i (-)	S_i (-)	N_i (-)
1700.5	8.3	-1	-1
...
2021.5	29.6	7.9	15233

For these biased normalised weights, the period and the amplitude error estimates for the weighted data signals would be dramatically larger than the respective errors for the non-weighted data signals. For example, the bootstrap reshuffling (see Equation 25) of the four $N_{1/2} = 4$ most accurate monthly values, or the one $N_{1/2} = 1$ most accurate yearly value, resembles Russian roulette, where the majority of remaining other data values do not seem to need to fit to the model at all. We emphasise that the weighted data itself causes this bias, not our period analysis method.

We solve this statistical bias of errors σ_i by using the Sigma-cutoff weights

$$\begin{cases} w'_i = 1, & \text{if } \sigma_i \leq K\bar{\sigma} \\ w'_i = (K\bar{\sigma}/\sigma_i)^x, & \text{if } \sigma_i > K\bar{\sigma}, \end{cases} \quad (3)$$

where $\bar{\sigma}$ is the mean of all σ_i , and the K and x values can be freely chosen (Handler, 2003; Breger et al., 2002). We use the same $K = 1$ and $x = 2$ values as Rodríguez et al. (2003), which gives

$$\begin{cases} \sigma'_i = 1, & \text{if } \sigma_i \leq \bar{\sigma} \\ \sigma'_i = \sigma_i/\bar{\sigma} > 1, & \text{if } \sigma_i > \bar{\sigma}. \end{cases} \quad (4)$$

Our chosen K and x values are reasonable, because they give 55 percent of monthly data having full weight 1, and 25 percent having weight below 1/2. The respective values for the yearly data are 53 and 24 percent.

Table 4. Normalised weights $w_{\text{nor},i}$ for Equation 2. (1) Sample. (2) Sample size. (3,4) Maximum and minimum $w_{\text{nor},i}$. (5) Number of largest $w_{\text{nor},i}$ having a sum exceeding $n/2$.

(1) Sample	(2) n	(3) $w_{\text{nor},\text{max}}$	(4) $w_{\text{nor},\text{min}}$	(5) $N_{1/2}$
	(-)	(-)	(-)	(-)
Monthly data				
All	2458	381	2.02×10^{-5}	4
Before 2000	2183	48.9	1.83×10^{-3}	64
Yearly data				
All	204	135	1.08×10^{-3}	1
Before 2000	182	21.6	1.11×10^{-2}	6

Table 5. Eight sunspot data samples. (1) Table from where sample is drawn. (2) Sample name. (3-4) Sample first and last observing time. (5) Sample time span. (6) Sample size. (7) Sample electronic file name.

(1) Table	(2) Name	(3) t_1 (y)	(4) t_n (y)	(5) ΔT (y)	(6) n (-)	(7) File
Table 2	Rmonthly	1749.0	2022.8	273.8	3287	Rmonthly.dat
Table 2	Rmonthly2000	1749.0	1999.9	250.9	3012	Rmonthly2000.dat
Table 2	Cmonthly	1818.0	2022.8	204.8	2458	Cmonthly.dat
Table 2	Cmonthly2000	1818.0	1999.9	181.9	2182	Cmonthly2000.dat
Table 3	Ryearly	1700.5	2021.5	321.0	322	Ryearly.dat
Table 3	Ryearly2000	1700.5	1999.5	299.0	300	Ryearly2000.dat
Table 3	Cyearly	1818.5	2021.5	203.0	204	Cyearly.dat
Table 3	Cyearly2000	1818.5	1995.5	181.0	182	Cyearly2000.dat

There are four exceptional cases. We use the sigma cutoff weights $w'_i = 1$ for the three exceptional cases $y_i = 0$, $S_i = 0$ and $N_i > 0$, which solves the infinite weight $w_i = \sigma_i^{-2} = 0^{-2} = \infty$ problem. Finally, we compute no error estimate for the one exceptional case, $S_i > 0$ and $N_i = 0$.

We analyse eight samples. The first four samples are monthly sunspot data drawn from Table 2. The last four samples are yearly sunspot data drawn from Table 3. All eight samples are published only in electronic form. We summarise the sample contents and sample naming abbreviations in Table 5.

2.1. Rmonthly and Rmonthly2000

Rmonthly is our largest sample ($n = 3287$, $\Delta T = 274^y$). It contains all t_i and y_i values from Table 2. Since the error estimates σ_i are unknown before January 1818, we use an arbitrary error $\sigma_i = 1$ for all data in this sample. We perform a non-weighted period analysis, which is based on the sum of squared residuals (Equation 11: R). Hence, the chosen $\sigma_i = 1$ value has no effect to our analysis results, because every observation has an equal weight. The particular file name Rmonthly is used because the period analysis is based on a non-weighted R test statistic.

Rmonthly2000 contains observations from **Rmonthly**, which were made before the year 2000 ($n = 3012$, $\Delta T = 251^y$). Number “2000” refers to the omitted data after the year 2000.

2.2. **Cmonthly** and **Cmonthly2000**

Cmonthly contains all t_i and y_i observations having an error estimate σ'_i computed from Equation 4 ($n = 2458$, $\Delta T = 205^y$). For this sample, we apply the weighted period analysis, which utilises the error σ'_i information (Equation 12: χ^2). The sample name begins with letter “C”, because our analysis is based on the weighted Chi-square test statistic (Equation 18).

Cmonthly2000 contains those **Cmonthly** observations, which were made before the year 2000 ($n = 2182$, $\Delta T = 182^y$). We refer to the omitted data after the year 2000 by using the number “2000”.

2.3. **Ryearly** and **Ryearly2000**

Ryearly is our longest sample ($\Delta T = 321^y$) containing $n = 322$ yearly mean total sunspot number observations over more than three centuries. Since no error estimates are available for observations before 1818, the value $\sigma_i = 1$ is used for all data. We perform a non-weighted period analysis based on the R test statistic (Equation 11), and therefore, the sample name begins with the letter “R”.

Ryearly2000 contains observations from **Ryearly** that were made before the year 2000.

2.4. **Cyearly** and **Cyearly2000**

Cyearly is the smallest sample ($n = 204$, $\Delta T = 204^y$). It contains all yearly mean total sunspot numbers having an error estimate σ'_i (Equation 4). We perform a weighted period analysis based on the χ^2 test statistic (Equation 12), and therefore, the sample name begins with the letter “C”.

Cyearly2000 contains all **Cyearly** data before the year 2000.

3. Discrete Chi-Square Method (DCM)

In this section, we give a thorough description the Discrete Chi-Square Method (DCM), because this is essential for understanding the results of our sunspot data analysis. Jetsu (2020, Paper I) formulated this method. He used DCM to discover the periods of a third and a fourth body from the O-C data of the eclipsing binary XZ And. An improved DCM version revealed the presence of numerous new companion candidates in the eclipsing binary Algol (Jetsu, 2021, Paper II). DCM is designed for detecting many signals superimposed on an arbitrary trend.

The sunspot number data notations are observations $y_i = y(t_i) \pm \sigma_i$, where t_i are the observing times and σ_i are the errors ($i = 1, 2, \dots, n$). The units are $[y_i] = \text{dimensionless}$, $[\sigma_i] = \text{dimensionless}$ and $[t_i] = \text{years}$. The time span of data is $\Delta T = t_n - t_1$. The mid point is $t_{\text{mid}} = t_1 + \Delta T/2$. Our notations for the mean and the standard deviation of all y_i values are m and s , respectively.

DCM model

$$g(t) = g(t, K_1, K_2, K_3) = h(t) + p(t). \quad (5)$$

is a sum of a periodic function

$$h(t) = h(t, K_1, K_2) = \sum_{i=1}^{K_1} h_i(t) \quad (6)$$

$$h_i(t) = \sum_{j=1}^{K_2} B_{i,j} \cos(2\pi j f_i t) + C_{i,j} \sin(2\pi j f_i t), \quad (7)$$

and an aperiodic function

$$p(t) = p(t, K_3) = \begin{cases} 0, & \text{if } K_3 = -1 \\ \sum_{k=0}^{K_3} p_k(t), & \text{if } K_3 = 0, 1, 2, \dots \end{cases} \quad (8)$$

where

$$p_k(t) = M_k \left[\frac{2(t - t_{\text{mid}})}{\Delta T} \right]^k. \quad (9)$$

The periodic $h(t)$ function is a sum of K_1 harmonic $h_i(t)$ signals having frequencies f_i .

The signal order is K_2 . For simplicity, we refer to $K_2 = 1$ order models as “pure sine” models, and to $K_2 = 2$ order models as “double wave” models. The former category of signal curves are pure sines. The latter category of signal curves can deviate from a pure sine.

The $h_i(t)$ signals are superimposed on the aperiodic K_3 order polynomial trend $p(t)$. Function $h(t)$ repeats itself in time. Function $p(t)$ does not repeat itself, except when $p(t) = 0$ for $K_3 = -1$ or $p(t) = M_0 = \text{constant}$ for $K_3 = 0$.

DCM model residuals are

$$\epsilon_i = y(t_i) - g(t_i) = y_i - g_i. \quad (10)$$

Our notations for the mean and standard deviation of the residuals are m_ϵ and s_ϵ . These residuals give the sum of squared residuals

$$R = \sum_{i=1}^n \epsilon_i^2, \quad (11)$$

and also the Chi-square

$$\chi^2 = \sum_{i=1}^n \frac{\epsilon_i^2}{\sigma_i^2}. \quad (12)$$

If the data errors σ_i are known, we use χ^2 to estimate the goodness of our model. For unknown errors σ_i , we use R .

Our notation for K_1 , K_2 and K_3 order DCM model $g(t)$ is “ $\mathcal{M}_{K_1, K_2, K_3, R}$ ” or “ $\mathcal{M}_{K_1, K_2, K_3, \chi^2}$ ”. The last subscripts “ R ” or “ χ^2 ” refer to the use of Equation 11 or 12 in estimating the goodness of our model, respectively.

The free parameters of model $g(t)$ are

$$\boldsymbol{\beta} = [\beta_1, \beta_2, \dots, \beta_\eta] = [B_{1,1}, C_{1,1}, f_1, \dots, B_{K_1, K_2}, C_{K_1, K_2}, f_{K_1}, M_0, \dots, M_{K_3}], \quad (13)$$

where

$$\eta = K_1 \times (2K_2 + 1) + K_3 + 1 \quad (14)$$

is the number of free parameters. We divide the free parameters β into two groups

$$\beta_I = [f_1, \dots, f_{K_1}] \quad (15)$$

$$\beta_{II} = [B_{1,1}C_{1,1}, \dots, B_{K_1, K_2}, C_{K_1, K_2}, M_0, \dots, M_{K_3}] \quad (16)$$

The first frequency group β_I makes the $g(t)$ model non-linear, because all free parameters are not eliminated from all partial derivatives $\partial g / \partial \beta_i$. If these β_I frequencies are fixed to the constant known tested numerical values, none of the partial derivatives $\partial g / \partial \beta_i$ contain any free parameters. In this case, the model becomes *linear*, and the solution for the second group of free parameters, β_{II} is *unambiguous*. Our concepts like “linear model” and “unambiguous result” refer to this type of models and their free parameter solutions.

For every tested frequency combination $\beta_I = [f_1, f_2, \dots, f_{K_1}]$, we compute the DCM test statistic

$$z = z(f_1, f_2, \dots, f_{K_1}) = \sqrt{R/n} \quad (17)$$

$$z = z(f_1, f_2, \dots, f_{K_1}) = \sqrt{\chi^2/n} \quad (18)$$

from a linear model least squares fit. We use Equation 17 or Equation 18, for unknown or known σ_i errors, respectively.

For two signal $K_1 = 2$ model, the sum $h(t)$ of signals $h_1(t)$ and $h_2(t)$ does not depend on the order in which these signals are added. This causes the symmetry $z(f_1, f_2) = z(f_2, f_1)$ for all tested frequency pairs f_1 and f_2 . The same symmetry applies to any other K_1 number of signals. Therefore, we compute z test statistic only for all combinations

$$f_{\max} \geq f_1 > f_2 > \dots > f_{K_1} \geq f_{\min}, \quad (19)$$

where f_{\min} and f_{\max} are the minimum and maximum tested frequencies, respectively. In the long search, we test an evenly spaced grid of n_L frequencies between f_{\min} and f_{\max} . This gives us the best frequency candidates $f_{1,\text{mid}}, \dots, f_{K_1,\text{mid}}$. In the short search, we test a denser grid of n_S frequencies within an interval

$$[f_{i,\text{mid}} - a, f_{i,\text{mid}} + a], \quad (20)$$

where $a = c(f_{\max} - f_{\min})/2$ and $i = 1, \dots, K_1$. In this study, we use $c = 0.05$ which means that the tested short search frequency interval represents 5% of the tested long search interval.

We search for periods between $P_{\min} = 1/f_{\max} = 5$ years and $P_{\max} = 1/f_{\min} = 200$ years. We will also briefly discuss the reasons for not detecting periods below $P_{\min} = 5$ years (Section 7.1).

The best linear model for the data gives the global periodogram minimum

$$z_{\min} = z(f_{1,\text{best}}, f_{2,\text{best}}, \dots, f_{K_1,\text{best}}) \quad (21)$$

at the tested frequencies $f_{1,\text{best}}, f_{2,\text{best}}, \dots, f_{K_1,\text{best}}$.

The scalar z periodogram values are computed from K_1 frequency values. For example, $K_1 = 2$ two signal periodogram $z(f_1, f_2)$ could be plotted like a map, where f_1 and f_2 are the coordinates, and $z = z(f_1, f_2)$ is the height. For three or more signals, such a direct graphical presentation

becomes impossible, because it requires more than three dimensions. We solve this problem by presenting only the following one-dimensional slices of the full periodogram

$$\begin{aligned}
 z_1(f_1) &= z(f_1, f_{2,\text{best}}, \dots, f_{K_1,\text{best}}) \\
 z_2(f_2) &= z(f_{1,\text{best}}, f_2, f_{3,\text{best}}, \dots, f_{K_1,\text{best}}) \\
 z_3(f_3) &= z(f_{1,\text{best}}, f_{2,\text{best}}, f_3, f_{4,\text{best}}, \dots, f_{K_1,\text{best}}) \\
 z_4(f_4) &= z(f_{1,\text{best}}, f_{2,\text{best}}, f_{3,\text{best}}, f_4, f_{5,\text{best}}, f_{K_1,\text{best}}) \\
 z_5(f_5) &= z(f_{1,\text{best}}, f_{2,\text{best}}, f_{3,\text{best}}, f_{4,\text{best}}, f_5, f_{K_1,\text{best}}) \\
 z_6(f_6) &= z(f_{1,\text{best}}, f_{2,\text{best}}, f_{3,\text{best}}, f_{4,\text{best}}, f_{5,\text{best}}, f_6).
 \end{aligned} \tag{22}$$

Using the above $K_1 = 2$ map analogy, the slice $z_1(f_1)$ represents the height z at a f_1 coordinate when moving along the constant line $f_2 = f_{2,\text{best}}$ that crosses the global minimum z_{\min} (Equation 21) at the coordinate point $(f_{1,\text{best}}, f_{2,\text{best}})$.

The best frequencies detected in the short search give the initial values for the first group of free parameters $\beta_{\text{I,initial}} = [f_{1,\text{best}}, \dots, f_{K_1,\text{best}}]$ (Equation 15). The linear model with these constant $[f_{1,\text{best}}, \dots, f_{K_1,\text{best}}]$ frequency values gives the unambiguous initial values for the second group $\beta_{\text{II,initial}}$ of free parameters (Equation 16). The final non-linear iteration is performed from

$$\beta_{\text{initial}} = [\beta_{\text{I,initial}}, \beta_{\text{II,initial}}] \rightarrow \beta_{\text{final}}. \tag{23}$$

DCM determines the following parameters for $h_i(t)$ signals

$$\begin{aligned}
 P_i &= 1/f_i = \text{Period} \\
 A_i &= \text{Peak to peak amplitude} \\
 t_{i,\min,1} &= \text{Deeper primary minimum epoch} \\
 t_{i,\min,2} &= \text{Secondary minimum epoch (if present)} \\
 t_{i,\max,1} &= \text{Higher primary maximum epoch} \\
 t_{i,\max,2} &= \text{Secondary maximum epoch (if present)},
 \end{aligned}$$

as well the M_k parameters of the $p(t)$ trend. For the sunspots, the most interesting parameters are the signal periods P_i , the signal amplitudes A_i , and signal primary minimum epochs $t_{\min,1}$ (Appendix: Tables 17 - 28).

The subtraction

$$y_{i,j} = y_i - [g(t_i) - h_j(t_i)] \tag{24}$$

shows how well all observations y_i are connected to any signal $h_j(t)$, where $j = 1, \dots, K_1$. In other words, the full model $g(t_i)$ is subtracted from the data y_i , except for the $h_j(t_i)$ signal itself. We shall later show examples of this subtraction in Figure 5. This subtraction resembles the Discrete Fourier Transform de-trending procedure (e.g. Murphy, 2012), but here we remove both the trend and all other signals, except for the $h_j(t_i)$ signal.

The DCM model parameter errors are determined with the bootstrap procedure (Efron and Tibshirani, 1986). We have previously used this same bootstrap procedure in our TSPA- and CPS-methods (Jetsu and Pelt, 1999; Lehtinen et al., 2011). A random sample ϵ^* is selected from the residuals ϵ of the DCM model (Equation 10). In this reshuffling of ϵ_i residuals, any ϵ_i can be chosen as many times as the random selection happens to favour it. This random sample of residuals gives the *artificial* bootstrap data sample

$$y_i^* = g_i + \epsilon_i^*. \tag{25}$$

We create numerous such \mathbf{y}^* random samples. The DCM model for each \mathbf{y}^* sample gives one estimate for every model parameter. The error estimate for each particular model parameter is the standard deviation of all estimates obtained from all \mathbf{y}^* bootstrap samples.

DCM models are nested. For example, a one signal model is a special case of a two signal model. DCM uses the Fisher-test to compare any pair of simple $g_1(t)$ and complex $g_2(t)$ models. Their number of free parameters are $\eta_1 < \eta_2$. Their sums of squared residuals (R_1, R_2) and Chi-squares (χ_1, χ_2) give the Fisher-test test statistic

$$F_R = \left(\frac{R_1}{R_2} - 1 \right) \left(\frac{n - \eta_2 - 1}{\eta_2 - \eta_1} \right) \quad (26)$$

$$F_\chi = \left(\frac{\chi_1^2}{\chi_2^2} - 1 \right) \left(\frac{n - \eta_2 - 1}{\eta_2 - \eta_1} \right). \quad (27)$$

The Fisher-test null hypothesis is

H_0 : “The complex model $g_2(t)$ does not provide a significantly better fit to the data than the simple model $g_1(t)$.”

Under H_0 , both test statistic parameters F_R and F_χ have an F distribution with (ν_1, ν_2) degrees of freedom, where $\nu_1 = \eta_2 - \eta_1$ and $\nu_2 = n - \eta_2$ (Draper and Smith, 1998). The probability for F_R or F_χ reaching values higher than F is called the critical level $Q_F = P(F_R \geq F)$ or $Q_F = P(F_\chi \geq F)$. We reject the H_0 hypothesis, if

$$Q_F < \gamma_F = 0.001, \quad (28)$$

where γ_F is the pre-assigned significance level. This γ_F represents the probability of falsely rejecting H_0 hypothesis when it is in fact true. If H_0 is rejected, we rate the complex $g_2(t)$ model better than the simple $g_1(t)$ model.

The basic idea of the Fisher-test is simple. The H_0 hypothesis rejection probability increases for larger F_R values having smaller Q_F critical levels. The complex model R_2 or χ_2^2 values decrease when the η_2 number of free parameters increases. This increases the first $(R_1/R_2 - 1)$ and $(\chi_1^2/\chi_2^2 - 1)$ terms in Equations 26 and 27. However, the second $(n - \eta_2 - 1)/(\eta_2 - \eta_1)$ penalty term decreases at the same time. This second penalty term prevents over-fitting, i.e. accepting complex models having too many η_2 free parameters.

The key ideas of DCM are based on the following robust, thoroughly tested statistical approaches

1. The DCM model $g(t)$ is *non-linear* (Equation 5). This model becomes *linear* when the frequencies $\beta_I = [f_1, \dots, f_{K_1}]$ (Equation 15) are fixed to their tested numerical values. This linear model gives *unambiguous* results for the other free parameters, β_{II} (Equation 16).
2. The short search $f_{1,\text{best}} > f_{2,\text{best}} > \dots > f_{K_1,\text{best}}$ grid combination that minimises the z test statistic gives the best initial β_{initial} values for the non-linear iteration of Equation 23.
3. DCM tests a dense grid of all possible frequency combinations $f_{\max} \geq f_1 > f_2 > \dots > f_{K_1} \geq f_{\min}$ (Equation 19). For every frequency combination, the *unambiguous linear* model least squares fit gives the test statistic $z = \sqrt{\chi^2/n}$ (errors σ_i known) or $z = \sqrt{R/n}$ (errors σ_i unknown).
4. All model parameter error estimates are determined with the bootstrap method (Equation 25).
5. The best model is identified using the Fisher-test, which compares all different tested K_1, K_2 and K_3 order combinations for nested models (Draper and Smith, 1998; Allen, 2004).

DCM has the following restrictions

1. If the frequency grid $f_1 > f_2 > \dots > f_{K_1}$ contains n_L values in the long search, then the total number of all tested frequency combinations is

$$\binom{n_L}{K_1} = \frac{n_L!}{K_1!(n_L - K_1)!}. \quad (29)$$

For example, it took about two days for a cluster of processors to compute the four signal DCM model for the `Rmonthly` sample (Figures 3-6).

2. An adequately dense tested frequency grid eliminates the possibility that the best frequency combination is missed. The restriction is that denser grids require more computation time. If the tested frequency grid is sufficiently dense, no abrupt periodogram jumps occur, because the z values for all close tested frequencies correlate. Hence, the frequencies of the minima of these periodograms are accurately determined. There is no need to test an even denser grid, because this would not alter the final result of the non-linear iteration of Equation 23.
3. Some DCM models are unstable. They are simply wrong models for the data, like a wrong $p(t)$ trend order K_3 or a search for too few or too many K_1 signals (e.g., Paper I: Figures 5-10). This causes model instability. We denote such unstable models with “UM” in Tables 17-28. The signatures of such unstable models are

“IF” = Intersecting frequencies
 “AD” = Dispersing amplitudes
 “LP” = Leaking periods

Intersecting frequencies “IF” occur when the frequencies of two signals are very close to each other. For example, if frequency f_1 approaches frequency f_2 , the $h_1(t)$ and $h_2(t)$ signals become essentially one and the same signal. This ruins the least squares fit. It makes no sense to add the same signal twice.

Dispersing amplitudes “AD” also occur when two signal frequencies are close to each other, like in the above-mentioned “IF” cases. The least squares fit uses two high amplitude signals which cancel out. Hence, the sum of these two high amplitude signals is one low amplitude signal that fits to the data.

We take extra care to identify the suspected “IF” and “AD” unstable model cases. The reshuffling of bootstrap ϵ^* residuals provides a good test for identifying such unstable models from the DCM analysis of numerous artificial bootstrap data samples \mathbf{y}^* (Equation 25). If we encounter any signs of instability, we test combinations $n_L = 100 \& c = 0.05$, $n_L = 100 \& c = 0.10$, $n_L = 120 \& c = 0.05$ and $n_L = 120 \& c = 0.10$. If there is instability in any of these combinations, we reject the model as unstable (“UM”). If there is no instability, we take the n_L and c combination that gives the lowest value for R (non-weighted data) or χ^2 (weighted data).

Leaking periods “LP” instability refers to the cases, where the detected frequency f is outside the tested frequency interval between f_{\min} and f_{\max} , or the period $P = 1/f$ of this frequency is longer than the time span ΔT of the data.

We use the DCM model $g(t_i, \beta)$ to predict the future and the past data. The three samples used in these predictions are the predictive data, the predicted data and all data. We use the following notations for the time points, the observations and the errors of these three samples.

- Predictive data: n values of t_i , y_i and σ_i
- Predicted data: n' values of t'_i , y'_i and σ'_i
- All data: $n'' = n + n'$ values of t''_i , y''_i and σ''_i from predictive and predicted data

We also compute the monthly or yearly time points during past activity minima of Table 1. Our notations for these time points are

- Activity minimum data: n''' values of t_i'''

DCM gives the best free parameter β values for the predictive data model $g_i = g(t_i, \beta)$, where the “old” t_{mid} and ΔT values are computed from the predictive data time points t_i . These “old” predictive data t_{mid} and ΔT values are used to compute the predicted data model values

$$g'_i = g(t'_i, \beta)$$

In other words, we do not compute “new” t_{mid} and ΔT values from the predicted data time points t'_i . There is an obvious reason for this. The predictive data free parameter values β give the correct g'_i values only for the “old” predictive data t_{mid} and ΔT values. The residuals

$$\epsilon'_i = y'_i - g'_i$$

of the predicted data give the *predicted test statistic*

$$z_{\text{pred}} = z \text{ test statistic for predicted data (Equation 17 or 18),} \quad (30)$$

which measures how well the prediction obtained from the predictive data works.

The best DCM model $g(t_i'', \beta)$ for all data uses the “old” t_{mid} and ΔT values computed from t_i'' time points of all data. We use these “old” t_{mid} and ΔT values to compute the predicted model values

$$g'''_i = g(t'''_i, \beta) \quad (31)$$

for the monthly or yearly time points t_i''' during the chosen activity minimum of Table 1. These g'''_i values give the *predicted mean level*

$$m_{\text{pred}} = \frac{1}{n'''} \sum_{i=1}^{n'''} g'''_i \quad (32)$$

during the selected activity minimum of Table 1.

It is essential to understand how and why the above two predictive parameters of Equations 30 and 32 are computed. The former parameter, z_{pred} , is computed from the *known* t'_i , y'_i and σ'_i values of the predicted data. If our predictions are correct, the following regularities should occur

z_{pred} decreases, if DCM detects real new signals in the predictive data
 z_{pred} increases, if DCM detects unreal new signals in the predictive data

For the latter m_{pred} parameter, the t_i''' , y_i''' or σ_i''' data values during the past activity minima are *unknown*, but we can create the n''' monthly or yearly t_i''' time points during these minima of Table 1. We can then compute the g_i''' values from these t_i''' values (Equation 31). This gives us the mean m_{pred} value (Equation 32) that can be compared to the mean level m for all data. If our predictions for the past activity minima of Table 1 are correct, the following regularities should occur

m_{pred} falls below m , if DCM detects real new signals in all data

m_{pred} decreases, if DCM detects real new signals in all data
 m_{pred} increases, if DCM detects unreal new signals in all data

Our model is non-linear (Equations 5 - 9). We find a unique solution for this ill-posed problem. The stages of finding this solution are

1. We fix the numerical values of the tested frequencies β_I (Equation 15). The model becomes linear and the solution for the other free parameters β_{II} is unique (Equation 16).
2. We test all possible β_I frequency combinations (Equation 19). The linear model for every tested frequency combination β_I gives a unique value for the test statistic z (Equations 17 and 18). We select the best frequency combination $\beta_{I,\text{best}}$ that minimises z . The model for this best frequency combination is unique and the free parameter values $\beta_{\text{initial}} = [\beta_{I,\text{best}}, \beta_{II,\text{best}}]$ of this model are unique.
3. These unique initial free parameter values β_{initial} are used in the non-linear iteration (Equation 23) that gives the unique final free parameter values β_{final} . This solution is unique.
4. We use the Fisher-test to compare many different non-linear models against each other. The selection criterion for the best model is unique (Equation 28).

After the selection of the tested non-linear models, these four stages give a unique the solution for this ill-posed problem.

4. Analysis: general description

We know that our DCM signal detections from the sunspot data can raise a controversy about the actual astrophysical origin of these signals. For this reason, we will first concentrate only on the statistical (not astrophysical) analysis of these data (Sections 4-6). We want to confirm beyond any reasonable doubt, that our signal detections are based only on the numerical values of the data, regardless of the phenomenon behind these numbers. This requires numerous tables and figures. We try to achieve a compact and clear presentation by giving the numerical results for all eight samples in our Appendix (Tables 17 - 28). This paper would have become extremely difficult to read if we had allowed these large tables to interrupt the main text twelve times. In all twelve tables, the four first $\mathcal{M}=1-4$ models, are computed for the original y_i data. The next four $\mathcal{M}=5-8$ models are computed for the ϵ_i residuals of the $\mathcal{M}=4$ model. The total number of tested DCM models in these twelve tables is 80. All signal detections are consistent. If a new signal is detected, the previously detected signal periods, amplitudes and phases are also re-detected. Without this consistency, our analysis could be considered unreliable. Inside each table, we use the Fisher-test to compare all models in an orderly fashion against each other. The extremely high² Fisher-test critical level estimates, $Q_F < 10^{-16} \ll \gamma = 0.001$ (Equation 28), confirm that these signal detections are very significant.

We present a detailed full DCM analysis description only for one sample `Rmonthly2000` (Section 6.1.1). For this particular sample, we explain thoroughly how to read all the results given in Table 17. Our aim is to make it as easy as possible to read and understand the results presented in the other eleven Tables 18-28.

We use the following four criteria to evaluate the reliability of our DCM analysis results.

C1: Sampling and consistency. DCM detects the same signals for
 Monthly and yearly data

²The highest achievable accuracy for the computational `f.cdf` subroutine in `scipy.optimize` python library is 10^{-16} .

Non-weighted and weighted data
 Pure sine and double wave models
 All data samples and their subsets: predictive data samples

C2: Predictivity. When the predictive data sample is used to predict the predicted data sample, the following predicted test statistic z_{pred} (Eq 30) regularities occur

z_{pred} decreases, if DCM detects real new signals in the predictive data
 z_{pred} increases, if DCM detects unreal new signals in the predictive data

C3: Predictivity. When an all data sample is used to predict the mean sunspot number during some past prolonged activity minimum in Table 1, the following predicted mean level m_{pred} (Eq 32) regularities occur

m_{pred} falls below m , if DCM detects real new signals in all data
 m_{pred} decreases, if DCM detects real new signals in all data
 m_{pred} increases, if DCM detects unreal new signals in all data

C4: Identification. Some periods detected in all data samples are connected to the orbital periods of planets.

The first two criteria C1 and C2 are purely statistical because the phenomenon behind the data is irrelevant (Sections 5 and 6). The evaluation of third criterion C3 in Section 6 is not purely statistical because we check if the DCM models can predict particular phenomena: the past prolonged activity minima in Table 1. The evaluation of last criterion C4 requires statistical and astrophysical comparison between the detected signal periods and the orbital periods of planets (Section 7). Finally, we apply the Discrete Fourier Transform (DFT) to cross-check our DCM analysis results (Section 8).

The two alternative theories for the origin of the sunspot cycle are the stochastic solar-dynamo-theory and the deterministic planetary-influence-theory. The easiest way to refer to these two alternative theories is to formulate these hypotheses:

H_{Dynamo} : “*The solar dynamo is a stochastic process. Therefore, deterministic sunspot number predictions longer than one solar cycle fail.*”
 H_{Planet} : “*Planetary motions are deterministic. Therefore, deterministic sunspot number predictions longer than one solar cycle can succeed.*”

The proponents of the mainstream H_{Dynamo} hypothesis argue that our four criteria can not be fulfilled. The proponents of the H_{Planet} hypothesis can not prove that these criteria are fulfilled.

5. Sampling and consistency criterion C1

In this section, we evaluate the sampling and consistency criterion C1. We analyse eight samples and detect only nine signals in the period range between 5 and 200 years (Tables 17-28). This leaves very little room for inconsistency. The periods and the amplitudes of the nine signals are summarised in Table 6, where we introduce the following signal abbreviations S_{11y} , S_{10y} , $S_{11.y86}$, S_{110y} , $S_{10.y6}$, $S_{8.y4}$, S_{53y} , S_{8y} and S_{66y} . The numerical values in the subscripts of our signal abbreviations refer to the signal period in Earth years. These signals are arranged into the order of decreasing strength, or equivalently, of decreasing amplitude. We use the signal ranking based on the signal amplitudes in the first analysed sample $R_{\text{monthly2000}}$ (Table 17), because this order for signal amplitudes varies slightly in different samples. For each particular sample, we

give the exact signal ranking order in Table 6. The two strongest detected signals in all samples are the S_{11y} and S_{10y} signals, and always in this order.

We must introduce the “double sinusoid” concept before we can evaluate the C1 criterion. The shape of these double sinusoid signals resembles that of a pure sinusoid (Figures 1a-g). All seven double sinusoids are highlighted with the notation “ $2\times$ ” in Table 6. For example, we detect only one signal for the double wave $K_2 = 2$ model of **Cmonthly** sample (Table 6: Column 9, Figure 1a). The period of this S_{11y} signal is $P = 21.667 \pm 0.014 = 2 \times (10.834 \pm 0.007)$ years. The period of this double sinusoid signal is about two times longer than the S_{11y} signal periods detected in all other eleven samples. In other words, including the **Cmonthly** sample, DCM detects this same S_{11y} signal in all twelve samples.

5.1. Results for monthly and yearly data

We detect seven double sinusoids (Figure 1, Table 6: “ $2\times$ ”). Since the periods of these double sinusoids can be divided by two, the detected five strongest S_{11y} , S_{10y} , $S_{11.y86}$, S_{110y} and $S_{10.y6}$ signals are the same in the monthly data (Table 6: Columns 2-9) and the yearly data (Table 6: Columns 10-13). There are minor differences in the detections of the four weaker $S_{8.y4}$, S_{53y} , S_{8y} and S_{66y} signals.

DCM detects the same five strongest signals in the monthly and yearly data.

5.2. Results for non-weighted and weighted data

We detect less signals in the weighted data (Table 6: Columns 7-8 and 12-13) than in the non-weighted data (Table 6: Columns 2-5 and 10-11). The most logical explanation for this result is that we have more non-weighted data. The four strongest S_{11y} , S_{10y} , $S_{11.y86}$ and S_{110y} signals detected in the weighted data samples are also detected in the non-weighted data samples. The only minor difference is the weakest S_{8y} signal detected in the weighted data, which is not detected in the two non-weighted **Ryearly** and **Ryearly2000** samples.

DCM detects the same four strongest signals in the weighted and the non-weighted data.

Table 6: Signals in monthly and yearly sunspot numbers. (1) Signal abbreviation. (2) Rmonthly2000 sample results for pure sines (Table 17: $K_2 = 1$). All six detected signals are given in order of decreasing peak to peak amplitude A . (3-13) Results for other samples with chosen K_2 values. Double sinusoid signals are denoted with “ $\times 2$ ”. Notes below give an example of how to read this table.

(1)	(2)	(3)	(4)	(5)	(6)	(7)	(8)	(9)	(10)	(11)	(12)	(13)
Monthly2000	Recently	Recently2000	Monthly	Monthly2000	Monthly	Monthly	Monthly2000	Monthly	Yearly2000	Yearly	Yearly2000	Yearly
$K_2 = 1$	$K_2 = 1$	$K_2 = 2$	$K_2 = 2$	$K_2 = 1$	$K_2 = 1$	$K_2 = 2$	$K_2 = 2$	$K_2 = 1$	$K_2 = 1$	$K_2 = 1$	$K_2 = 1$	$K_2 = 1$
Table 17	Table 18	Table 19	Table 20	Table 21	Table 22	Table 23	Table 24	Table 25	Table 26	Table 27	Table 28	Table 29
Rank (-)	Rank (-)	Rank (-)	Rank (-)	Rank (-)	Rank (-)	Rank (-)	Rank (-)	Rank (-)	Rank (-)	Rank (-)	Rank (-)	Rank (-)
$P(y)$	$P(y)$	$P(y)$	$P(y)$	$P(y)$	$P(y)$	$P(y)$	$P(y)$	$P(y)$	$P(y)$	$P(y)$	$P(y)$	$P(y)$
$A(-)$	$A(-)$	$A(-)$	$A(-)$	$A(-)$	$A(-)$	$A(-)$	$A(-)$	$A(-)$	$A(-)$	$A(-)$	$A(-)$	$A(-)$
S_{11y}	(1) 11.0324±0.0048	(1) 11.0033±0.0064	(1) 11.0234±0.0068	(1) 10.9875±0.0051	(1) 10.805±0.013	(1) 10.8585±0.0048	(1) 10.8075±0.012	(1) 21.667±0.0142 \times	(1) 11.0065±0.017	(1) 10.9815±0.020	(1) 10.8135±0.029	(1) 10.8635±0.022
	98.8±2.6	101.5±2.5	102.9±2.7	104.6±2.3	118.2±3.7	117.5±2.9	123.5±3.0	132.6±3.4	90.4±4.7	98.3±7.8	119.2±8.5	119.3±7.5
S_{10y}	(2) 9.9842±0.0075	(2) 10.0001±0.0081	(2) 9.9882±0.0061	(2) 20.0063±0.0088 \times	(2) 10.196±0.027	(2) 10.0655±0.0077	(2) 10.1965±0.017	(2) 9.9805±0.016	(2) 9.9755±0.017	(2) 10.1845±0.064	(2) 10.0585±0.026	(2) Ryearly2000
	77.4±2.2	65.5±2.1	78.6±2.6	75.2±2.7	61.9±3.9	59.3±2.8	62.1±3.7	64.6±7.6	62.8±6.1	62.3±6.8	61.0±9.6	$K_2 = 1$
$S_{11,y86}$	(3) 11.846±0.012	(3) 11.807±0.012	(4) 23.6865±0.0182 \times	(4) 11.7705±0.011	(4) 11.7705±0.011	(4) 11.8635±0.021	(4) 11.8635±0.021	(5) 11.8635±0.034	(5) 11.8205±0.027	(5) 11.8565±0.068	(5) 11.8565±0.068	(4) 43.8±7.9
	60.0±2.2	56.4±2.4	69.4±2.7	62.7±2.6	43.3±2.0	42.6±4.1	40.5±3.3	42.6±4.1	40.5±3.3	42.6±4.1	40.5±3.3	$K_2 = 1$
S_{110y}	(4) 96.2±1.0	(4) 99.9±2.0	(3) 104.1±0.59	(3) 104.1±0.59	(3) 104.2±0.68	(3) 116.7±1.3	(3) 100.3±2.1	(4) 100.3±2.1	(4) 101.4±2.4	(3) 115.6±3.6	(3) 115.6±3.6	(4) 53.8±5.2
	50.1±2.8	51.8±2.3	50.4±3.6	68.1±2.7	52.9±2.5	52.4±6.3	52.4±6.3	52.4±6.3	51.7±4.9	51.7±4.9	51.7±4.9	$K_2 = 1$
$S_{10,y6}$	(5) 10.541±0.014	(5) 10.569±0.020	(5) 10.5372±0.0075	(5) 10.5407±0.0060	(5) 10.6205±0.033	(5) 10.6595±0.031	(5) 59.9±8.6	(5) 52.4±8.5	(5) 52.4±8.5	(5) 52.4±8.5	(5) 52.4±8.5	$K_2 = 1$
	45.0±1.8	51.0±1.8	51.2±1.8	55.6±2.3	52.4±8.5	52.4±8.5	52.4±8.5	52.4±8.5	52.4±8.5	52.4±8.5	52.4±8.5	$K_2 = 1$
$S_{8,y4}$	(6) 16.781±0.0342 \times	(6) 44.9±4.0	(6) 16.755±0.0272 \times	(6) 41.2±3.1	(7) 8.4605±0.027	(7) 33.0±4.4	(7) 31.1±4.8	(7) 8.4665±0.016	(7) 31.1±4.8	(7) 8.4665±0.016	(7) 31.1±4.8	$K_2 = 1$
	33.9±2.0	52.6±0.27	33.9±2.0	52.6±0.27	53.24±0.78	53.83±0.76	53.3±6.3	53.24±0.78	53.83±0.76	53.24±0.78	53.83±0.76	$K_2 = 1$
$S_{5,3y}$	(6) 8.1054±0.0084	(7) 8.1087±0.0076	(8) 8.1735±0.011	(8) 8.1695±0.014	(5) 8.0095±0.017	(6) 35.5±3.3	(6) 25.6±2.5	(8) 65.4±1.3	(8) 66.7±1.4	(8) 65.4±1.3	(8) 66.7±1.4	$K_2 = 1$
	36.5±1.7	33.6±1.6	37.6±4.8	35.5±3.3	25.6±2.5	25.6±2.5	25.6±2.5	29.0±4.7	29.0±4.7	29.0±4.7	29.0±4.7	$K_2 = 1$
S_{66y}	(7) 136.43±0.992 \times	(7) 42.3±2.2	(7) 37.3±2.7	(7) 37.3±2.7	(8) 6.05±0.058	(8) 24.0±7.0	(8) 24.0±7.0	(8) 24.0±7.0	(8) 24.0±7.0	(8) 24.0±7.0	(8) 24.0±7.0	$K_2 = 1$

Notes. For example, signal S_{11y} is detected in sample Rmonthly2000 (Column 2). Rank="1" means that this S_{11y} signal is strongest of all six signals in Table 17. Signal S_{11y} has period $P = 11.0324 \pm 0.0048$ and peak to peak amplitude $A = 98.8 \pm 2.6$.

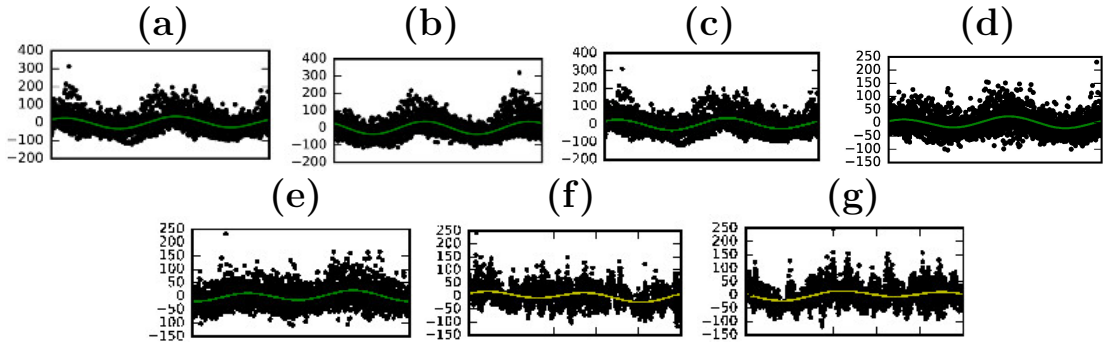


Figure 1. Double sinusoids $^{2\times}$ (Table 6). (a) **Cmonthly**: S_{11y} signal period $21.667 \pm 0.014 = 2 \times (10.834 \pm 0.007)$. (b) **Rmonthly**: S_{10y} signal period $20.0062 \pm 0.0088 = 2 \times (10.0031 \pm 0.0044)$. (c) **Rmonthly2000**: $S_{11.y86}$ signal period $23.686 \pm 0.018 = 2 \times (11.843 \pm 0.009)$. (d) **Rmonthly2000**: $S_{8.y4}$ signal period $16.781 \pm 0.034 = 2 \times (8.390 \pm 0.017)$. (e) **Rmonthly**: $S_{8.y4}$ signal period $16.753 \pm 0.027 = 2 \times (8.376 \pm 0.014)$. (f) **Rmonthly2000**: S_{66y} signal period $136.43 \pm 0.99 = 2 \times (68.22 \pm 0.50)$. (g) **Rmonthly**: S_{66y} signal period $143.39 \pm 0.99 = 2 \times (71.70 \pm 0.50)$. Numbers and labels for x-axis phases ϕ between 0 and 1 are missing, because these figures are extracts from larger figures, like Figure 5. Period units are x-axis $[\phi]$ = dimensionless and y-axis $[y]$ = dimensionless.

5.3. Results for pure sine and double wave models

The pure sine and double wave model results can be compared only for the *same sample*.

For both non-weighted samples **Rmonthly2000** and **Rmonthly**, the pure sine and the double wave models give the same five strongest signals S_{11y} , S_{10y} , $S_{11.y86}$, S_{110y} and $S_{10.y6}$ (Table 6: Columns 2-5). The detected weak signal S_{8y} is also the same. The minor differences are the two double sinusoid $S_{8.y4}$ signals detected only in the **Rmonthly** and **Rmonthly2000** samples, and the pure sine S_{53y} signal detected only in the **Rmonthly** sample.

For the weighted sample **Cmonthly2000** sample, results for pure sine and double wave models give the same S_{11y} and S_{10y} signals (Table 6: Columns 6 and 8).

For the weighted sample **Cmonthly**, the pure sine DCM models detect five signals S_{11y} , S_{11y} , S_{10y} , $S_{11.y86}$, S_{110y} and S_{8y} (Table 6: Column 7). For the double wave DCM model, only the double sinusoid $^{2\times}$ counterpart of S_{11y} signal is detected in this **Cmonthly** sample (Table 6: Column 9).

We do not apply the double wave models to the small yearly data samples (Table 6: Column 10-13). Therefore, pure sine and double wave model results can not be compared for these samples.

For the pure sine and double wave models, DCM detects the same strongest signals in each individual sample.

5.4. Results for all data samples and their subsets: predictive data samples

The results for pairs of predictive data and all data are given in consecutive columns of Table 6.

The same six signals S_{11y} , S_{10y} , $S_{11.y86}$, S_{110y} , $S_{10.y6}$ and S_{8y} are detected in the sample pair **Rmonthly2000** and **Rmonthly** (Table 6: Columns 2-3). The only minor difference is the weak signal S_{53y} , which is detected only in the larger sample **Rmonthly**.

The same eight signals are detected in the sample pair **Rmonthly** and **Rmonthly2000** (Table 6: Columns 4-5).

For the **Cmonthly2000** and **Cmonthly** pair, the two strongest detected S_{11y} and S_{10y} signals are the same (Table 6: Columns 6-7). The other three weaker $S_{11.y86}$, S_{110y} and S_{8y} signals are detected only in the larger all data sample **Cmonthly**.

The S_{11y} signal is detected in the pair **Cmonthly2000** and **Cmonthly** (Table 6: Columns 8-9). The S_{10y} signal is detected only in the smaller predictive data sample **Cmonthly2000**.

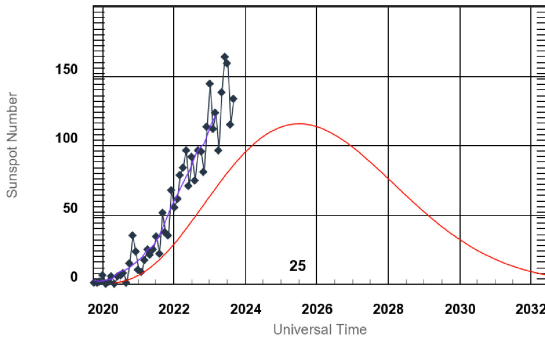


Figure 2. Solar Cycle Prediction Panel forecast for solar cycle 25. Red curve shows predicted monthly sunspot numbers after December 2019. Grey shaded area shows prediction error. Black curve denotes observed monthly sunspot number up to September 2024. Blue line denotes observed smoothed 13 months mean.

We detect the same eight signals in the $R_{\text{yearly}2000}$ and R_{yearly} (Table 6: Columns 10-11).

For the last $C_{\text{yearly}2000}$ and C_{yearly} pair, the detected S_{11y} and S_{10y} signals are the same (Table 6: Columns 12-13). The $S_{11,y86}$, S_{110y} and S_{8y} signals are detected only in the larger C_{yearly} sample.

If some signal is detected, its period is the same in the pairs of predictive and all data.

Our period detections in all eight samples are extremely consistent (Sections 5.1-5.4). We conclude that the sampling and consistency criterion C1 is certainly fulfilled.

6. Predictability criteria C2 and C3

Before the evaluation of our C2 and C3 predictability criteria, it is crucial to check what level of predictability has already been reached. In the year 2019, the Solar Cycle Prediction Panel representing NOAA, NASA and the International Space Environmental Services (ISES) made the official forecast for solar cycle 25. The red curve in Figure 2 shows the synthesis of about 50 different forecasts received from the scientific community. During the current sunspot cycle 25, the maximum difference between the smoothed monthly sunspot number and the predicted values has been

$$s_{\text{ISES}} = \pm(117.0 - 66.3) \approx \pm 50 \quad (33)$$

on March 2024.³ This gives an estimate for the accuracy that could be achieved in sunspot number predictions for the past four years after 2019. We do not argue that this is the best achievable accuracy, but this is the current best official published forecast. However, this accuracy would certainly be worse if this forecast covered more than one solar cycle. The s_{ISES} parameter of Equation 33 is hereafter referred as the four year “ISES limit”. If our model prediction deviates less than s_{ISES} from the predicted observations, we state that the prediction is “within the ISES limit”. In such cases, our prediction deviates less than s_{ISES} from the the smoothed thirteen monthly sunspot data..

The evaluation of the predictivity criteria C2 and C3 requires detailed analysis, where each one of the six pairs of predictive and all data samples is studied separately. For each pair, we use the predictive and the predicted data samples to evaluate the C2 criterion. The all data samples

³Space Weather Prediction Center on October 2nd, 2024.

are used to evaluate the C3 criterion. We use the red continuous and dotted lines to denote the model and the model errors, respectively. The sliding thirty years mean of this model and the sliding mean error are denoted with the green continuous and dotted curves. We will show many predictions extending to time intervals before and after the analysed samples (Figures 7, 8, 9, 10 and 11). The thirty years sliding mean predictions are always more accurate than the model predictions (Figures 7-11: red curves). Therefore, the green curve errors (dotted green lines) are always smaller than the red curve errors (dotted red lines). The red model curve predictions are shown only for the first few cycles after the newest, most accurate sunspot data. Since the oldest sunspot data are sparse and inaccurate, we show no red curve predictions before these data. The thirty years sliding mean green curve predictions are shown for the time intervals before and after the sunspot data. To ensure easy readability of all Figures 7-11, we surround the realm of our predictions with black dash-dotted rectangles. We also use long black horizontal arrows to highlight the direction of these predictions in time. The dash-dotted cyan lines in all model residuals ϵ_i plots denote the four year ISES limits $\pm s_{\text{ISES}}$ (Equation 33).

6.1. Non-weighted monthly sunspot data

6.1.1. Pure sines

In this section, we describe the DCM pure sine model analysis of `Rmonthly2000` sample in great detail. We do not describe the details of the analyses for other samples, because we analyse these other samples exactly same way as sample `Rmonthly2000`. For this particular `Rmonthly2000` sample, we first explain how to read the results presented in Table 17. We then explain the DCM periodogram (Figure 3), the DCM model (Figure 4), the DCM signals (Figure 5), the DCM bootstrap results (Figure 6), and the DCM model predictions (Figure 7a-c).

DCM pure sine model analysis of `Rmonthly2000` sample is summarised in Table 17. Here, we give detailed instructions of how to read this table.

The first one signal $\mathcal{M}=1$ model is $\mathcal{M}_{1,1,0,R}$, where the model orders are $K_1 = 1$, $K_2 = 1$ and $K_3 = 0$, and the subscript “ R ” refers to a non-weighted DCM analysis based on R test statistic (Equation 11). This model has $\eta = 4$ free parameters (Equation 14). The sum of squared residuals of this model is $R = 1.09 \times 10^7$ (Equation 11). The first signal period is $P_1 = 11.0336 \pm 0.0074$ years. The dimensionless peak to peak amplitude of this one signal is $A_1 = 92.2 \pm 2.8$. The primary minimum epoch of this one signal is at year $t_{\min,1} = 1755.30 \pm 0.12$.

Every new model is more complex when going down in our Table 17, because the number η of free parameters increases. The Fisher-test between the simple $\mathcal{M}=1$ model and the complex $\mathcal{M}=2$ model gives a test statistic value $F_R = 255$ (Equation 26) reaching a critical level $Q_F < 10^{-16}$. The Fisher-test null hypothesis H_0 is rejected because the criterion $Q_F < \gamma = 0.001$ is fulfilled (Equation 28). Therefore, an upward arrow “ \uparrow ” indicates that the $\mathcal{M}=2$ model is a better model than the $\mathcal{M}=1$ model. A leftward arrow “ \leftarrow ” would have been used if model $\mathcal{M}=1$ were better. The electronic control file `Rmonthly2000K110R14.dat` can be used to repeat⁴ whole DCM analysis of model $\mathcal{M}=1$. The four first signals are detected from the original data in electronic file `Rmonthly2000.dat`. The next four $\mathcal{M}=5-8$ model signals are detected from the residuals of model $\mathcal{M}=4$, which are stored to electronic file `RmonthlyK410R14Residuals.dat`. The best model for the `Rmonthly2000` sample is the six signal $\mathcal{M}=6$ model, because the $\mathcal{M}=7$ and 8 models are unstable (“UM”). These two unstable models suffer from the amplitude dispersion

⁴All analysed data and the DCM Python code are available in <https://zenodo.org/uploads/11503698>, where we give detailed instructions for repeating the whole analysis presented in Tables 17-28.

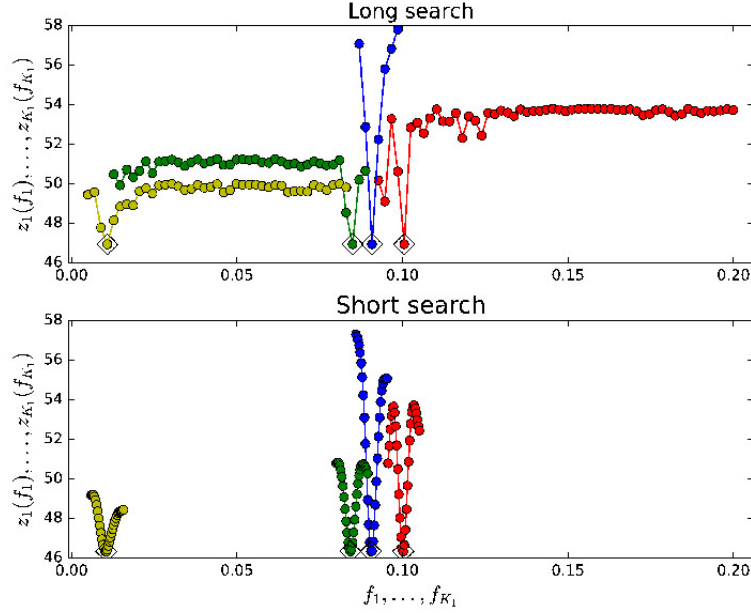


Figure 3. Rmonthly2000 sample four pure sine signal model $\mathcal{M}=4$ (Table 17). Periodograms are computed between $P_{\min} = 5$ and $P_{\max} = 200$ years for grids having $n_L = 100$ and $n_S = 30$ tested frequencies. Upper panel shows long search $z_1(f_1)$ (red), $z_2(f_2)$ (blue), $z_3(f_3)$ (green), and $z_4(f_4)$ (yellow) periodograms (Equation 22). Best frequencies are marked with diamonds. Lower panel shows short search periodograms for a denser frequency grid having an interval width $c = 0.05 \equiv 5\%$ (Equation 20). Otherwise as in upper panel. Units in both panels are x-axis $[f] = 1/\text{years}$ and y-axis $[z] = \text{dimensionless}$.

("AD"). Intersecting frequencies ("IF") or leaking periods ("LP") are not encountered in any of the eight $\mathcal{M}=1\text{-}8$ models in Table 17.

The best model for the Rmonthly sample, the six signal model in Table 17, is the $g(t)$ model $\mathcal{M}=4$ added to the $g(t)$ model $\mathcal{M}=6$. We refer to this six signal model simply as the $\mathcal{M}=6$ model.

We show the four pure sine signal $\mathcal{M}=4$ model periodograms between $P_{\min} = 5$ and $P_{\max} = 200$ years in Figure 3. All four z_1 , z_2 , z_3 and z_4 periodograms are continuous. Since the close-by periodogram values correlate, there are no abrupt deviations from the smooth periodogram changes, and a denser grid of tested frequencies would give exactly the same initial values β_{initial} for the non-linear iteration (Equation 23). The minima denoted with diamonds are well defined. The narrow, sharp shapes of these periodogram minima strongly support the idea that DCM detects real periods.

The four pure sine signal $g(t)$ model for sample Rmonthly2000 is shown in Figure 4. The remaining additional $\mathcal{M}=5$ and 6 model signals, which are still undetected at this stage, cause some of the regularities seen in the blue circles denoting the ϵ_i residuals. The four signals of $\mathcal{M}=4$ model are shown separately in Figure 5. When we plot these signals as a function of phase in the right-hand panels, they appear strong, clear and convincing. The time span of these four signals covers about 25 ($\sim 274/11$) sunspot cycles, and their changes as a function of phase, certainly do not appear stochastic (Figure 5: Right-hand panels). Finally, we emphasise that the bootstrap estimates for the frequencies and amplitudes of these four signals are stable (Figure 6).

Sample Rmonthly2000 contains the predictive data. The predicted data are the Rmonthly sample observations after the year 2000. The whole Rmonthly sample represents all data.

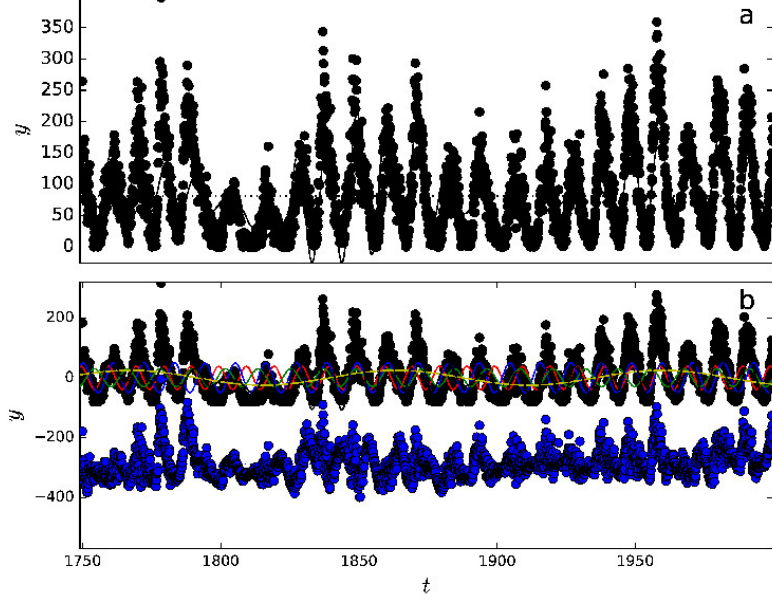


Figure 4. Rmonthly2000 sample four pure sine signal model $\mathcal{M}=4$ (Table 17). Upper panel shows data y_i (black circles), $g(t)$ (continuous black curve) and constant trend $p(t) = M_0 = 81.3$ (dotted black curve). Lower panel shows data minus trend $y_i(t) - p(t)$ values (black circles), and $g(t) - p(t)$ (black curve), $h_1(t)$ (red curve), $h_2(t)$ (blue curve), $h_3(t)$ (green curve) and $h_4(t)$ (yellow curve). Residuals (blue circles) are offset to $y = -300$ level. Signal periods are $P_1 = 9.9842$, $P_2 = 11.0234$, $P_3 = 11.846$ and $P_4 = 96.2$ years. Units in both panels are x-axis $[t] = \text{years}$ and y-axis $[y] = \text{dimensionless}$.

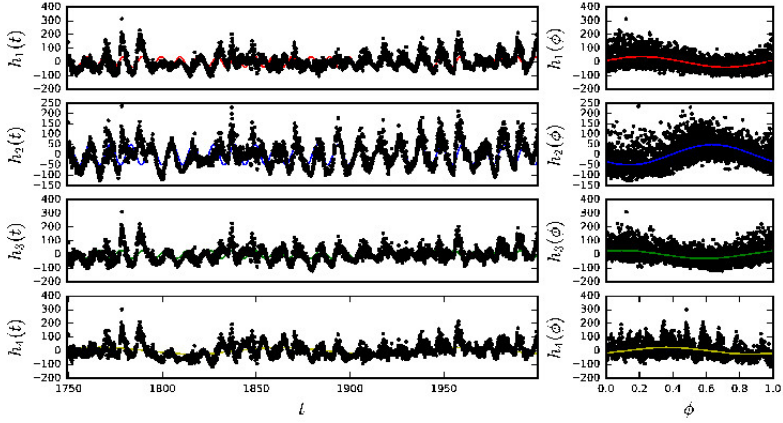


Figure 5. Rmonthly2000 sample four pure sine signal model $\mathcal{M}=4$ (Table 17). Left-hand panels. Values of $h_j(t)$ and $y_{i,j}$ (Equation 24) for four signals as a function of time. Signal periods in years are $P_1 = 9.9842$ (red curve), $P_2 = 11.0234$ (blue curve), $P_3 = 11.846$ (green curve), and $P_4 = 96.2$ (yellow curve). Units are x-axis $[t] = \text{years}$ and y-axis $[h_j(t)] = [y_{i,j}] = \text{dimensionless}$. Right-hand panels. Same signals as a function of phase ϕ . Units are x-axis $[\phi] = \text{dimensionless}$ and y-axis $[h_j(t)] = [y_{i,j}] = \text{dimensionless}$.

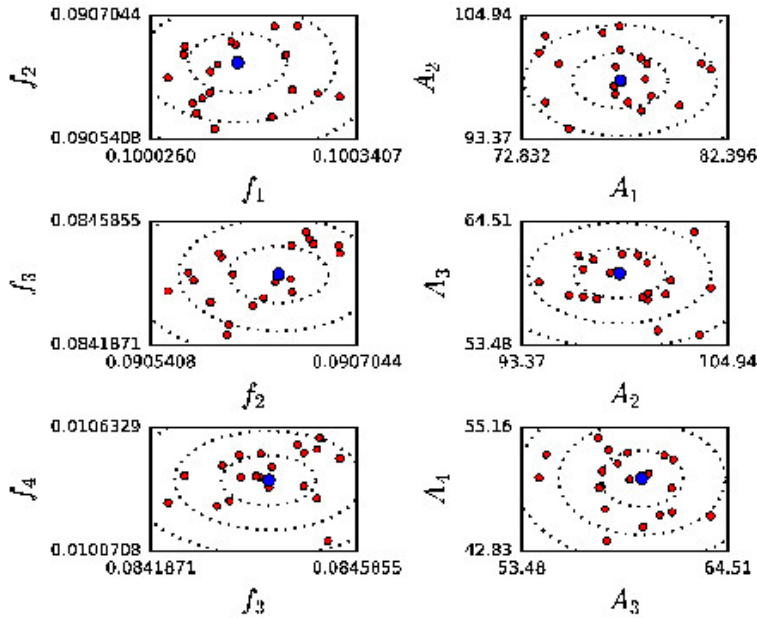


Figure 6. Rmonthly2000 sample four pure sine signal model $\mathcal{M}=4$ (Table 17). Left-hand panels show bootstrap signal frequency estimates (f_1, f_2, f_3, f_4). Units are $[f_i] = 1/\text{years}$. Right-hand panels show respective peak to peak amplitude estimates (A_1, A_2, A_3, A_4). Units are $[A_i] = \text{dimensionless}$. Larger blue circles denote values for original data. Smaller red circles denote values for bootstrap random samples y_i^* (Equation 25). Dotted lines denote one, two and three sigma error limits.

The smallest predicted test statistic z_{pred} (Equation 30) value is achieved for the five pure sines $\mathcal{M}=5$ model (Figure 7a). Predictability is better for one signal than for two signals. Then, this z_{pred} predictability improves for three, four and five signals. This z_{pred} improvement trend indicates that these five first signals are deterministic, not stochastic. Six signals give nearly the same predictability. For more than six signals, predictability becomes worse. Furthermore, the seven and eight signal models are unstable (Table 17: “UM” models $\mathcal{M}=7$ and 8). We compute z_{pred} values also for these unstable models, just to verify, if predictability stops improving due to instability. Criterion C2 is fulfilled.

For the predictive Rmonthly2000 data sample, the five signal prediction after 2000 succeeds quite well until a clear deviation from the data occurs in the year 2013 (Figure 7b). Most of the blue dots denoting the predictive model residuals are within the horizontal cyan dash dotted lines of ISES limit (Equation 33).

The five pure sines model can reproduce the Dalton minimum because it is inside the predictive data (Figure 7c). There is a dip at the end of the Maunder minimum, but the prediction for the duration of the Maunder minimum fails.

The DCM pure sine model analysis results for Rmonthly are given in Table 18. This all data sample gives the predicted mean level m_{pred} (Equation 32) values for the past activity minima. These predictions are not convincing (Figure 7d). Only the blue and yellow circles denoting Sporer and Oort minima are below the black horizontal dotted line denoting the mean level $m = 81.6$ of all sunspot numbers. Criterion C3 is not fulfilled. Rmonthly sample pure sines prediction indicates that the current prolonged low solar activity level has just ended (Figure 7e: green curve). The long-term past and future predictions are shown in Figure 7f.

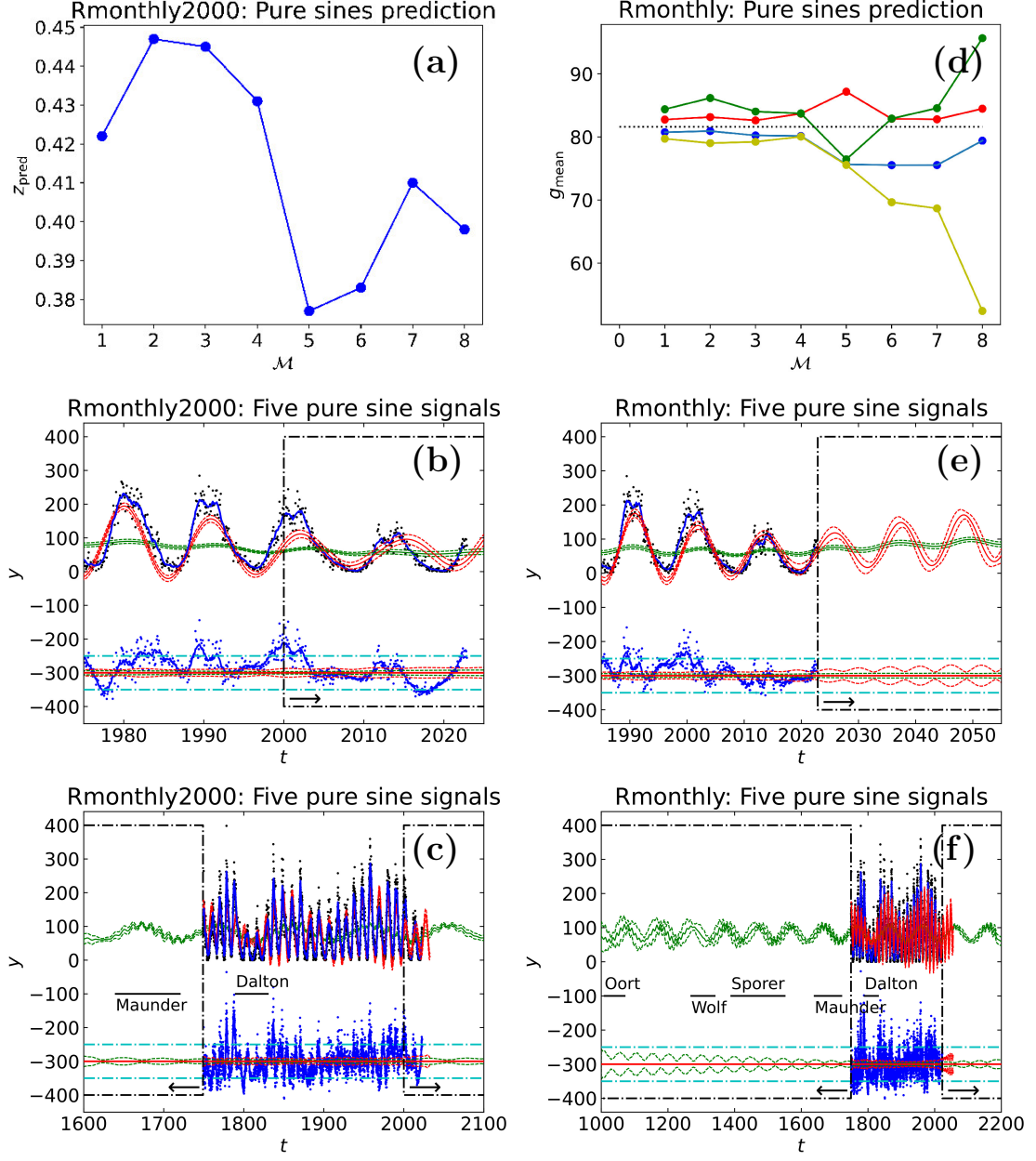


Figure 7. (a) Rmonthly2000 predictions for pure sines (Table 17). (a) Predicted test statistic z_{pred} (Equation 30) for pure sine models $\mathcal{M}=1-8$. Best model $\mathcal{M}=5$ minimises z_{pred} . Units are x-axis $[\mathcal{M}]$ =dimensionless and y-axis $[z_{\text{pred}}]$ = dimensionless. (b) Black dots denote data y_i . Blue continuous line denotes 13 month smoothed data. Red continuous line denotes $g(t)$ model $\mathcal{M}=5$. Dotted red lines denote $\pm 3\sigma$ model error limits for $g(t)$. Green continuous line denotes model $g(t)$ thirty years sliding mean. Dotted green lines show $\pm 3\sigma$ error limits for this sliding mean. Predictive data ends at vertical dash-dotted black line. Predicted data, predicted model and predicted thirty years mean are surrounded by this black dash-dotted line. Black arrow shows prediction direction in time. Blue dots denote residuals ϵ_i offset to level -300, which is outlined with red continuous line. Dash-dotted cyan lines denote ISES prediction SIES error limit (Equation 33). Units are x-axis $[t]$ = years and y-axis $[y]$ = dimensionless. (c) Horizontal black continuous lines outline time intervals of Dalton and Maunder minima. Except for a longer time span, otherwise as in “b”. (d) Rmonthly predictions for pure sines (Table 18): Predicted mean level m_{pred} (Equation 32) for pure sine $\mathcal{M}=1-8$ models during Maunder (red), Sporer (blue), Wolf (green) and Oort (yellow) minima. Dotted black line shows the mean $m = 81.6$ for all y_i data. Units are x-axis $[\mathcal{M}]$ =dimensionless and y-axis $[m_{\text{pred}}]$ = dimensionless. (e) $\mathcal{M}=5$ model for modern times and its prediction after year 2022. Otherwise as in “b”. (f) $\mathcal{M}=5$ model for long-term past and future. Otherwise as in “c”

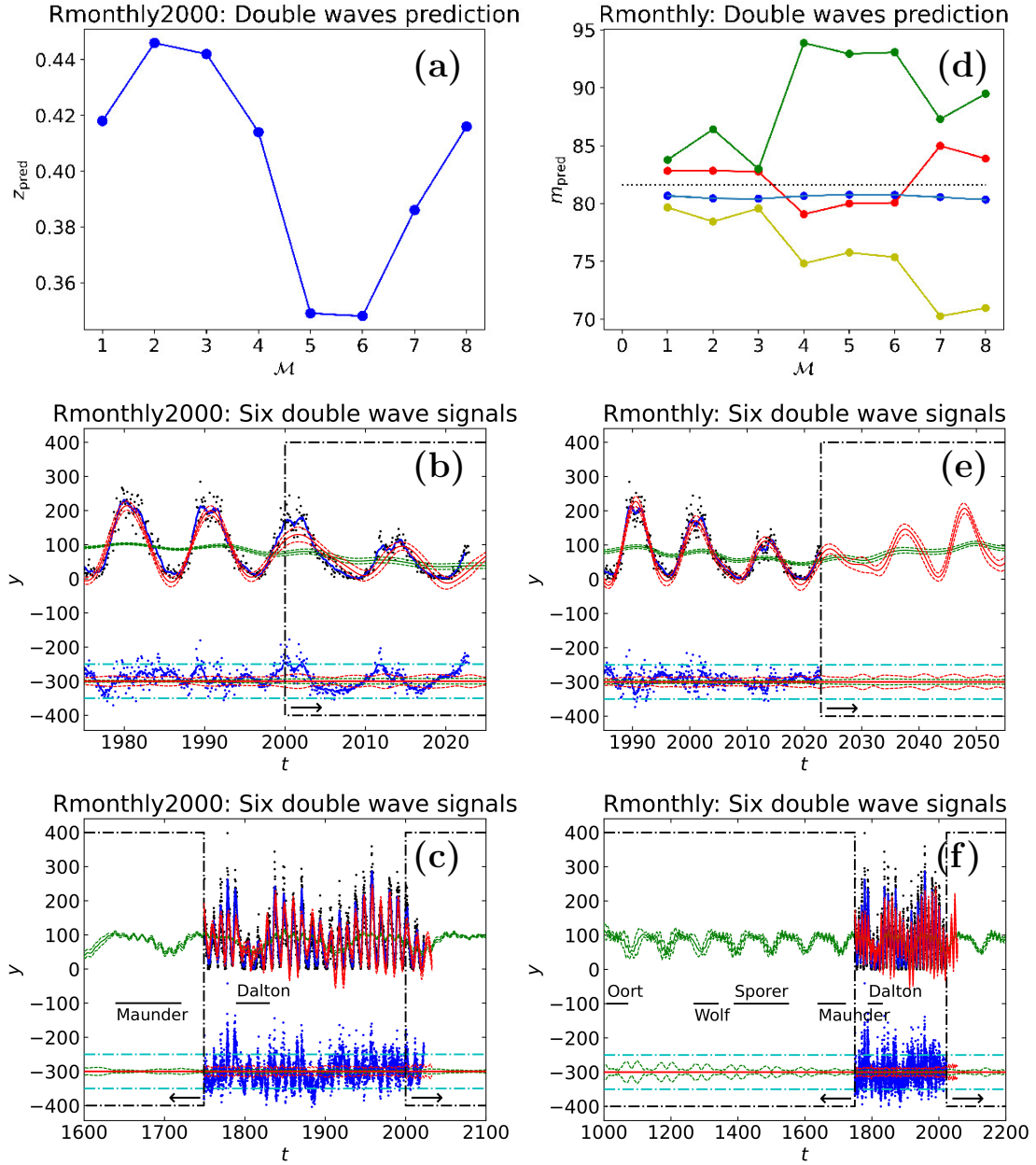


Figure 8. Rmonthly2000 predictions for double waves (Table 19). (a-c) Best double wave model $\mathcal{M}=6$ minimises z_{pred} (Equation 30). Otherwise as in Figures 7a-c. (d-f) Rmonthly predictions for double waves (Table 20). Otherwise as in Figures 7d-f.

6.1.2. Double waves

The predictive data sample is Rmonthly2000 . All data sample is Rmonthly . The Rmonthly sample values after the year 2000 are the predicted data.

The DCM double wave model results for Rmonthly2000 and Rmonthly samples are given Tables 19 and 20, respectively. For both samples, the periods and amplitudes of the eight strongest double wave signals are summarised in Table 6 (Columns 4 and 5).

The prediction test statistic z_{pred} (Equation 30) decreases until six signals are detected. Then, z_{pred} begins to increase for seven and eight signals (Figure 8a). This indicates that the first six detected signals are real, but the next seventh and eighth signals are not. These z_{pred} changes confirm that criterion C2 is fulfilled.

The prediction obtained from the predictive data Rmonthly2000 sample begins after the black vertical dash-dotted line at the year 2000 (Figure 8b). For twenty years, the majority of predictive model residuals (blue dots) are within the ISES limit (Equation 33: cyan dash dotted lines). The six signal double wave DCM model can reproduce the Dalton minimum inside Rmonthly2000 . The thirty years sliding mean shows a dip at the end of the Maunder minimum. This dip outside sample Rmonthly2000 does not cover the whole Maunder minimum era (Figure 8c: green curve).

The predictive data Rmonthly2000 sample z_{pred} (Equation 30) values indicate the presence of six signals (Figure 8a). The all data Rmonthly sample mean level prediction m_{mean} (Equation 32) for the Maunder minimum supports this result. The predicted mean level m_{mean} curve for the Maunder minimum fulfils criterion C3 (Figure 8d: red curve). For the first three $\mathcal{M}=1-3$ signals, this red m_{pred} curve is above the all data mean level m denoted with dotted black line. For the next three $\mathcal{M}=4-6$ signals, the m_{pred} values fall below the m mean level. Finally, these m_{mean} values for $\mathcal{M}=7$ and 8 signals rise again above the mean level m .

The Maunder minimum is outside all data sample Rmonthly . It is the closest activity minimum before the beginning of this sample. This could explain why only this particular deterministic activity minimum prediction succeeds. The m_{pred} predictions fail for the other activity minima, probably because these minima are further away in the past than the Maunder minimum. The decreasing Oort minimum m_{mean} trend deserves to be mentioned (Figure 8d: yellow curve).

The six double wave DCM model for all data Rmonthly sample predicts that the mean level of solar activity begins to rise in the near future (Figure 8e: green curve). This model predicts a turning point at 2029, which does not necessarily represent the beginning of a new activity cycle (Figure 8e: red curve). The long-term thirty years sliding mean shows a clear dip during the end of Maunder minimum (Figure 8f: green curve).

6.2. Weighted monthly sunspot data

The Cmonthly2000 sample contains the predictive data. The Cmonthly sample contains all data, where the observations after the year 2000 are the predicted data.

For the predictive data Cmonthly2000 sample, both pure sine and double wave models are unstable for more than two signals (Tables 21 and 23: “UM”). The detected signals are given in Table 6 (Columns 6 and 8). It is of no use to study criterion C2 for only two detected signals in sample Cmonthly2000 .

For all data sample Cmonthly , all double wave models for two or more signals are unstable (Table 24: “UM”). The only detected signal is given in Table 6 (Column 9). It would make no sense to study criterion C3 for only one signal detected in sample Cmonthly .

Fortunately, we can detect five pure sine signals in all data sample Cmonthly (Table 22). These signals are given in Table 6 (Column 7). This allows us to study criterion C3 for pure sine

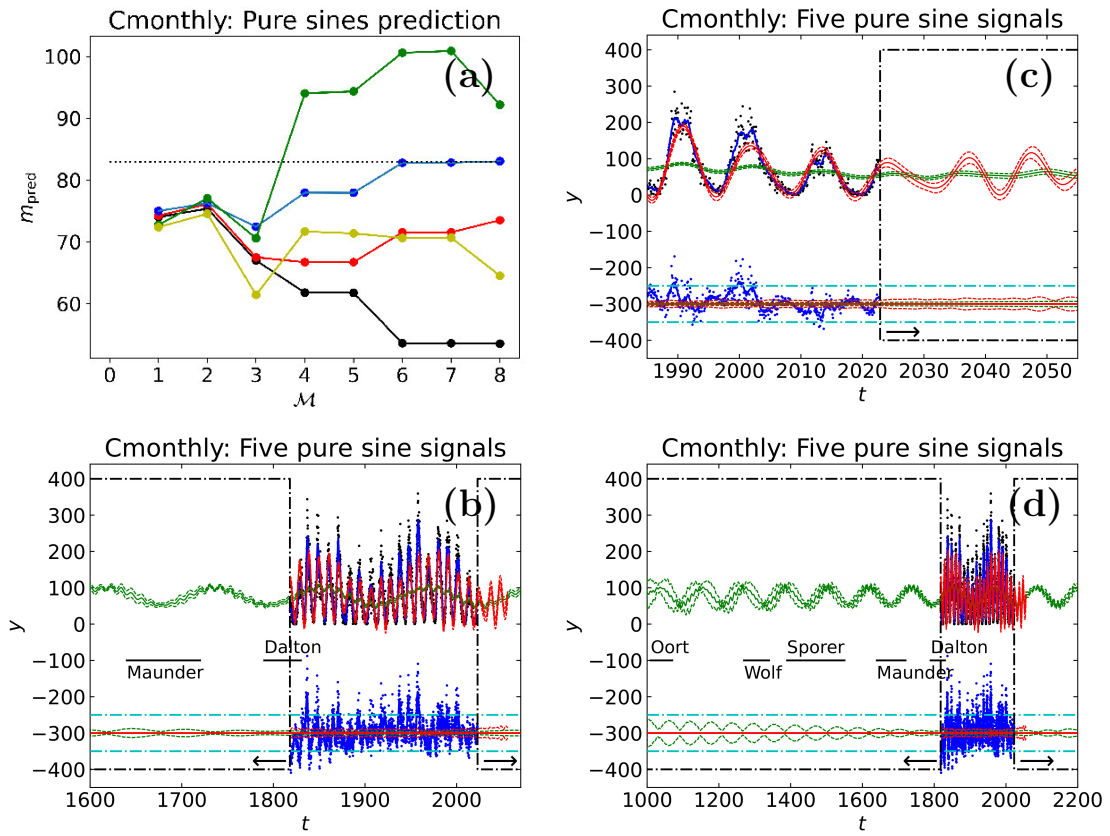


Figure 9. Cmonthly predictions for pure sines (Table 22). (a) Pure sine $M=1-8$ model predictions for m_{pred} (Equation 32) during Dalton (black), Maunder (red), Sporer (blue), Wolf (green) and Oort (yellow) minima. Otherwise as in Figure 7d. (b) Model $M=5$ pure sine prediction for near past. Otherwise as in Figure 7c. (c) Model $M=5$ pure sine prediction for near future. Otherwise as in Figure 7e. (d) Model $M=5$ pure sine long-term predictions. Otherwise as in Figure 7f.

models. The predicted mean level m_{pred} (Equation 32) curves are promising (Figure 9a). The m_{pred} curves for all activity minima in Table 1 show a dip at model $M=3$. This dip is clearly below the dotted black line denoting the mean $m = 81.6$ of all monthly sunspot numbers. Except for the green Wolf minimum curve, all m_{pred} curves stay below this mean m . The predicted mean level m_{pred} curve for the Dalton minimum fulfills the criterion C3 convincingly (Figure 9a: black curve), most probably because this activity minimum between 1790 and 1830 partly overlaps the Cmonthly sample between 1818 and 2022. Furthermore, the predicted mean level m_{pred} curve for the second closest Maunder minimum is good (Figure 9a: red curve). Criterion C3 is definitely fulfilled.

The deterministic predictions for the Dalton and the Maunder minima are illustrated in Figure 9b (green curve). These curves can reproduce the duration of these activity minima, but not the low values of sunspots. The errors for the predicted model (red dotted lines) and the predicted sliding 30 years mean (green dotted lines) are far smaller than the ISES limit (Equation 33: dashed dotted cyan lines). This deterministic prediction is obtained for the two past centuries before the beginning of data. The time span of this successful prediction is about twenty times longer than the one sunspot cycle limit of stochastic H_{Dynamo} hypothesis predictions. Since this

model can predict the time intervals of past weak activity, it should also be able to predict the time intervals of future weak activity. The same five pure sine signal prediction for the next decades is shown in Figure 9c (red curve). The long-term prediction confirms the result already obtained earlier for other samples: the activity level of the Sun increases during the next half a century (Figure 9d: green curve).

6.3. Non-weighted yearly sunspot data

The four and eight signal DCM double wave models have $\eta = 21$ and $\eta = 21 + 20$ free parameters, respectively. The yearly sunspot data sample **Ryearly2000** contains only $n = 300$ observations. To avoid over-fitting, we analyse these yearly data only with the four and eight signal DCM pure sine models having $\eta = 13$ and $\eta = 13 + 12$ free parameters.

The **Ryearly** sample contains all data, where observations after 2000 are the predicted data. The **Ryearly2000** sample observations are the predictive data.

The predictive data sample **Ryearly2000** DCM analysis gives the predicted test statistic z_{pred} (Equation 30) values shown in Figure 10a. The best six signal model gives the smallest z_{pred} value. The z_{pred} values for the seven and eight signal models are larger.

This six signal model gives an amazingly accurate prediction for the twenty years of predicted data after the year 2000 (Figure 10b: red curve after the vertical black dash-dotted line). *All* predicted data values are between the dotted red lines denoting $\pm 3\sigma$ prediction error limits. About half of these black dots denoting the predicted data overlap the continuous red line denoting the predicted model. *All* residuals of predicted data (blue dots) are significantly smaller than the ISES limit (Equation 33: cyan dash dotted lines). Had we been able to apply DCM to the **Ryearly2000** sample in the year 2000, we could have predicted the yearly sunspots number for the next two decades! The time span of this successful deterministic prediction is about two times longer than the stochastic one sunspot cycle prediction limit of H_{Dynamo} hypothesis. Criterion C2 is certainly fulfilled.

For **Ryearly2000** sample, the six signal model can reproduce the Dalton minimum inside the predictive data, but not the Maunder minimum, which is outside this sample (Figure 10c: green curve).

The predicted mean levels m_{pred} (Equation 32) for the all data sample **Ryearly** are shown in Figure 10d. Even the red curve for the Maunder minimum, which is closest to the beginning of this **Ryearly** sample, stays above the mean level $m = 78.4$ of all data. These predicted mean level m_{pred} estimates for the past activity minima do not fulfil criterion C3. The six pure sine signal model for the next decades predicts rising solar activity (Figure 10e: green line).

6.4. Weighted yearly sunspot data

The predictive data sample is **Cyearly2000**. Sample **Cyearly** is all data, where the observations after the year 2000 are the predicted data. We study only the pure sine DCM models, because the **Cyearly** and **Cyearly2000** samples are both too small ($n = 204$ and 182) for the DCM double wave model analysis.

We detect only two pure sine signals in the predictive data sample **Cyearly2000**. Additional signals give unstable models (Table 27: “UM”). Therefore, we can not study criterion C2.

Five pure sine signals are detected in all data sample **Cyearly** (Table 28). We give the periods and amplitudes of these five signals in Table 6 (Column 13).

The pure sine signal DCM models $M=1-8$ give the predicted mean level m_{pred} (Equation 32) values shown in Figure 11a. The black and red m_{pred} curves for the Dalton and the Maunder minima fall clearly below the mean level $m = 82.8$ of all yearly sunspot data. After this, these two

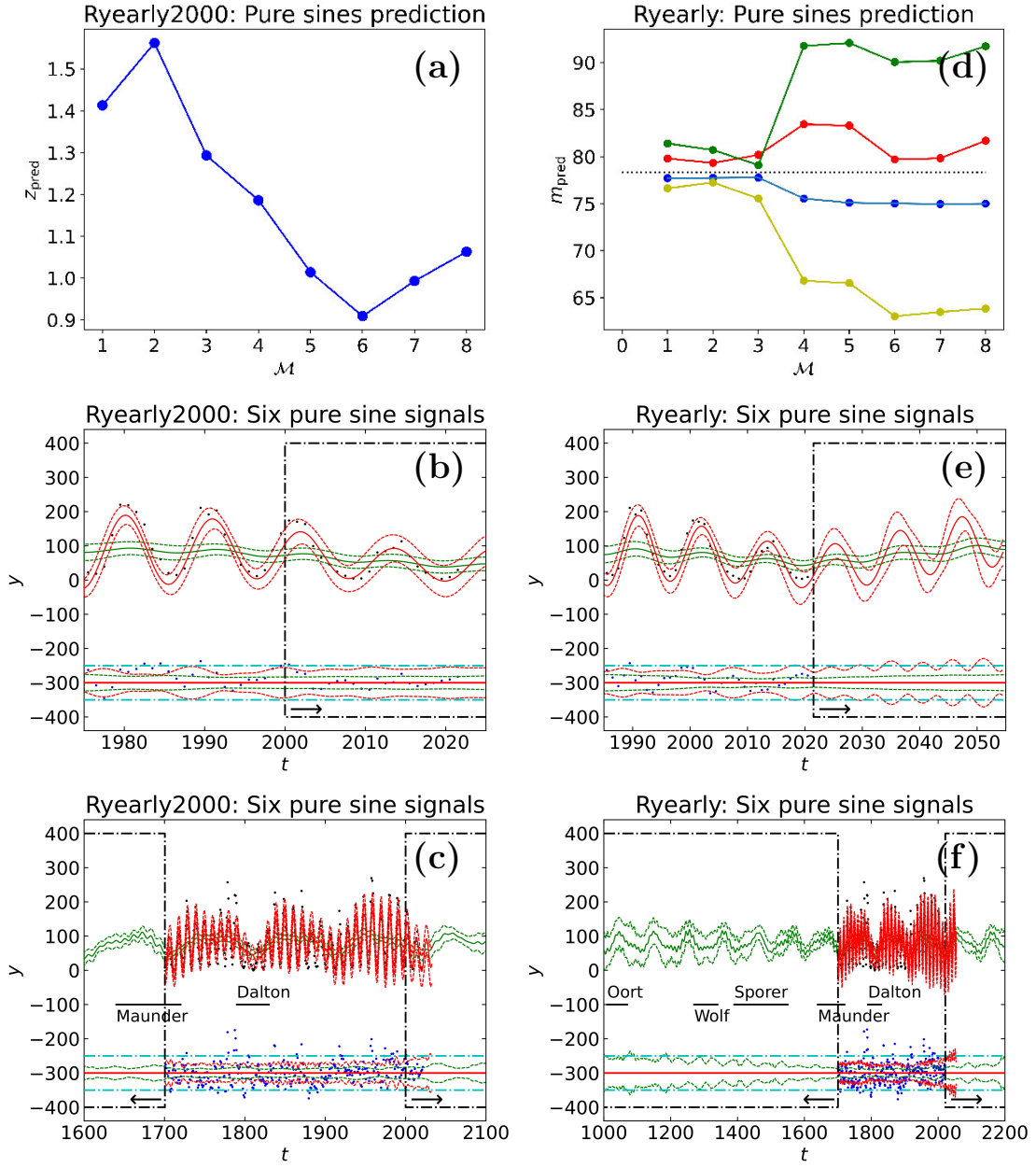


Figure 10. (a-c) Ryearly2000 predictions for pure sines (Table 25). Otherwise as in Figure 7a-c. Ryearly predictions for pure sines (Table 26). Otherwise as in Figure 7d-f.

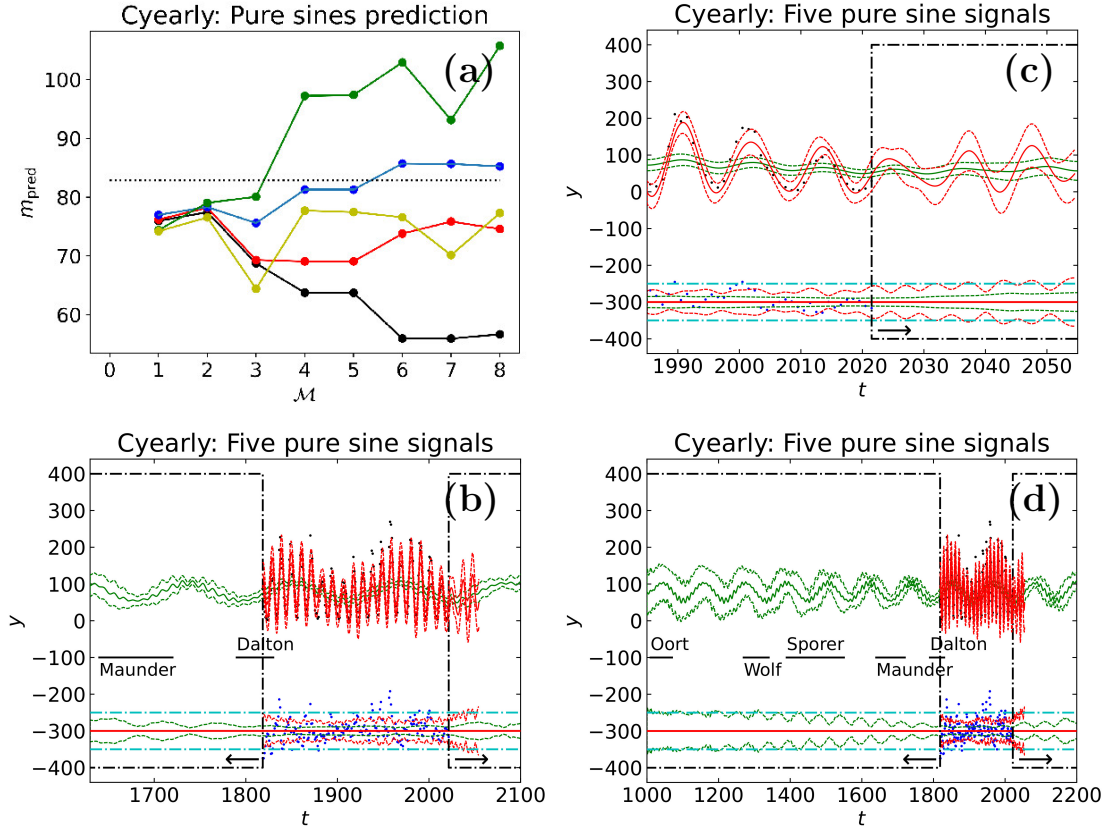


Figure 11. (a-d) Cyearly predictions (Table 28). Otherwise as in Figure 9a-d.

curves also stay below this m level. These results are not unexpected because the Dalton and the Maunder minima are the closest activity minima before the beginning of the Cyearly sample. Criterion C3 is certainly fulfilled.

The all data sample Cyearly prediction for the time intervals of the Dalton and the Maunder minima is excellent (Figure 11b: green curve). However, the prediction can not reproduce the low number of sunspots during the Maunder minimum. The green dotted lines denoting the error of the predicted 30 years sliding mean stay well below the ISES limit denoted with cyan dash-dotted lines (Equation 33). This successful deterministic prediction for the Maunder minimum time interval covers two centuries backwards, before the beginning of the analysed data sample Cyearly. This time interval is about twenty times longer than the stochastic H_{Dynamo} hypothesis predictability limit of only one solar cycle. It is actually quite unexpected that only about 200 years of data can predict so well the activity mean level for the past 200 years without any data. This can succeed only if the model is correct and deterministic. It also means that our prediction for the future can be considered reliable. This Cyearly sample future prediction for the next decades is shown in Figure 11c. The long-term prediction indicates rising solar activity during the next half a century (Figure 11d).

Our best predictive models are very consistent because the number of signals is either five (Figures 7a, 9a and 11a) or six (Figures 8a and 10a). We conclude that the predictions presented in Sections 6.1-6.4 confirm that the predictability C2 and C3 criteria are definitely fulfilled.

Table 7. Predictions for next three sunspot cycle minima and maxima. (1) Sample: Figure showing predictions. (2-3) Sunspot cycle 25. Maximum epoch ($t_{\max,25}$), sunspot number at maximum epoch ($y_{\max,25}$), minimum epoch ($t_{\min,25}$) and sunspot number at minimum epoch ($y_{\min,25}$). (4-5) Sunspot cycle 26. Otherwise as in “2-3”. (6-7) Sunspot cycle 27. Otherwise as in “2-3”. Line below each group of five estimates gives their weighted mean.

(1)	(2)	(3)	(4)	(5)	(6)	(7)
Sample: Figure	Maximum 25		Maximum 26		Maximum 27	
	$t_{\max,25}$ (y)	$y_{\max,25}$ (-)	$t_{\max,26}$ (y)	$y_{\max,26}$ (-)	$t_{\max,27}$ (y)	$y_{\max,27}$ (-)
Rmonthly: Figure 7e	2025.86 \pm 0.16	118.4 \pm 5.9	2037.40 \pm 0.20	148.7 \pm 5.7	2048.41 \pm 0.22	170.9 \pm 5.4
Rmonthly: Figure 8e	2024.42 \pm 0.20	88.6 \pm 4.8	2037.6 \pm 4.9	146 \pm 30	2047.9 \pm 5.1	207 \pm 18
Cmonthly: Figure 9c	2024.07 \pm 0.19	89.4 \pm 4.1	2037.39 \pm 0.13	102.8 \pm 5.3	2047.48 \pm 0.15	116.6 \pm 5.4
Ryearly: Figure 10e	2025.28 \pm 0.39	106 \pm 14	2036.62 \pm 0.41	145 \pm 16	2047.40 \pm 0.41	185 \pm 15
Cyearly: Figure 11c	2024.36 \pm 0.78	90 \pm 10	2037.4 \pm 1.3	112 \pm 22	2047.5 \pm 2.0	126 \pm 21
Weighted mean:	2024.94 \pm 0.79	95 \pm 12	2037.34 \pm 0.19	125 \pm 22	2047.72 \pm 0.41	148 \pm 30
	Minimum 25		Minimum 26		Minimum 27	
	$t_{\min,25}$ (y)	$y_{\min,25}$ (-)	$t_{\min,26}$ (y)	$y_{\min,26}$ (-)	$t_{\min,27}$ (y)	$y_{\min,27}$ (-)
Rmonthly: Figure 7e	2031.57 \pm 0.18	16.8 \pm 6.1	2042.82 \pm 0.20	22.4 \pm 5.5	2053.76 \pm 0.23	34.0 \pm 5.0
Rmonthly: Figure 8e	2032.7 \pm 5.0	25 \pm 10	2043.4 \pm 5.0	6 \pm 15	2054.1 \pm 5.4	39.4 \pm 6.8
Cmonthly: Figure 9c	2031.77 \pm 0.28	19.2 \pm 4.4	2042.35 \pm 0.14	0.3 \pm 4.4	2052.58 \pm 0.18	28.8 \pm 5.2
Ryearly: Figure 10e	2030.77 \pm 0.38	-15 \pm 15	2041.79 \pm 0.38	16 \pm 16	2052.62 \pm 0.41	38 \pm 17
Cyearly: Figure 11c	2031.8 \pm 1.1	16 \pm 13	2042.3 \pm 2.0	-1 \pm 19	2052.7 \pm 2.2	28 \pm 17
Weighted mean:	2031.52 \pm 0.31	17.4 \pm 7.4	2042.44 \pm 0.29	9 \pm 10	2052.98 \pm 0.56	33.0 \pm 4.3

6.5. Future sunspot maxima and minima predictions

We give the predictions for the next three sunspot cycle maxima and minima in Table 7.

The lowest possible real sunspot number is zero. We can not prevent DCM from utilising negative model $g(t)$ values. For this reason, two predicted cycle minimum sunspot number estimates out of all fifteen estimates, $y_{\min,25} = -15 \pm 15$ and $y_{\min,26} = -1 \pm 19$, are negative (Table 7). However, in these two exceptional cases the sunspot number can be zero within $\pm 1\sigma$.

The ISES prediction for the cycle 25 maximum epoch was $t_{\max,25} = \text{July } 2025 \pm 8.0 \text{ months} = 2025.54 \pm 0.67$. Their smoothed maximum sunspot number prediction was $y_{\max,25} = 115$. Our predictions $t_{\max,25} = \text{December } 2024 \pm 9.5 \text{ months} = 2024.94 \pm 0.79$ and $y_{\max,25} = 95 \pm 12$ differ 0.76σ and 1.67σ from the ISES prediction.

Our prediction error ± 0.79 for the cycle 25 maximum epoch is much larger than our prediction errors ± 0.79 and ± 0.41 for the next two maximum epochs (Table 7). This is a real statistical effect. The predicted peak of this next cycle 25 maximum is lower than, and not so sharp as, the predicted peaks of the next cycle 26 and 27 maxima (Figures 7e, 8e, 9c, 10e, and 11c).

The six double wave model predictions for the largest Rmonthly sample are not very accurate in Table 7 (Rmonthly: Figure 8e). The probable reason for this inaccuracy is the large number $\eta = 21 + 10$ of the free parameters (Table 20: model $M=6$). This is also the only model that has a turning point in the year 2029 (Figure 8e).

We predict that the mid-point of the next prolonged grand sunspot minimum is approximately in the year 2100 (Figures 7f, 8f, 9d, 10f and 11d: green curve).

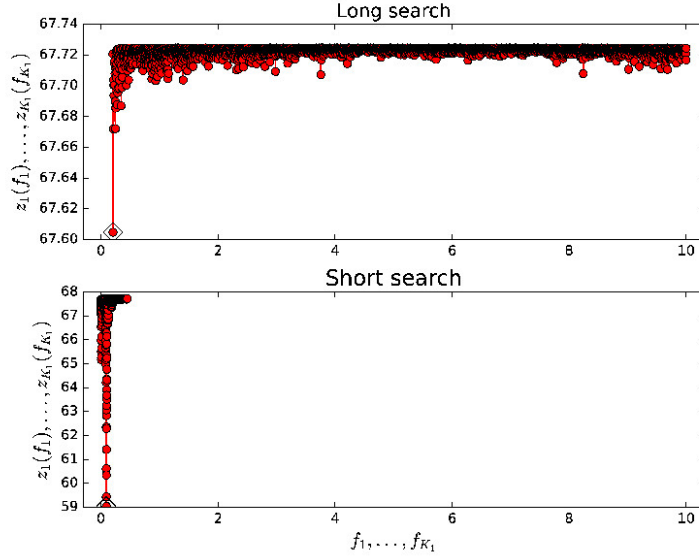


Figure 12. R_{monthly} one pure sine signal model. (Upper panel) Long search periodogram between $P_{\min} = 0.1$ and $P_{\max} = 5$ years. Tested grid contains $n_L = 3000$ frequencies. Diamond denotes best 4.84 year period. (Lower panel) Short search periodogram for $n_S = 1000$ and $c = 0.05$. Diamond denotes best 11.00 year period.

7. Planet identification criterion C4

The evaluation of consistency criterion C1 and the predictability criterion C2 is pure statistical analysis. The predictability criterion C3 evaluation is also mainly based on statistical analysis, where we check how the model predicts past prolonged activity minima. In this current astrophysical analysis section, we compare the detected signals to the known periods of planets. We underline this difference between our statistical and astrophysical analyses for a good reason. We want to avoid the possible false impression that we somehow detect these signals by searching for correlations between planetary motions and sunspot data. We do not. DCM would detect the same signal periods, if the numerical values of our data represented any other arbitrary phenomenon than the sunspots or the planets. We have treated these periods just as numbers.

The following possible misunderstandings must be corrected. Firstly, all detected signals are already given in Table 6. We are not fitting multiples of planetary signals into the data. Secondly, the identification of these multiples is not numerology. We are only trying to identify the most obvious multiples that could be connected to the planets.

7.1. Statistics for planetary signal identification

So far, we have refrained from identifying planetary signals among the best detected periods. The evaluation of criterion C4 requires such an identification. We have applied DCM to search for periods between 5 and 200 years. The periods of the inner planets Mercury (P_{Mercury}), Venus (P_{Venus}), the Earth (P_{Earth}) and Mars (P_{Mars}) are outside this interval. We can not search for these planets in the yearly sunspot data, because these planetary periods are close to, or below, the one-year window period. However, the monthly sunspot data can be used to search for these shorter planetary periods.

Here, we apply DCM to search for periods between $P_{\min} = 0.1$ and $P_{\max} = 5$ years from the non-weighted monthly sunspot R_{monthly} sample. This sample is our largest one. The one pure

Table 8. Relative tidal forces of planets (Equation 34). (1) Planet. (2) Major axis. (3) Mass. (4) Relative tidal force.

Planet	(1) a (a_{Earth})	(2) m (m_{Earth})	(4) R_{Tidal} (-)
Mercury	0.39	0.055	0.95
Venus	0.72	0.82	2.16
Earth	1.00	1.00	1.00
Mars	1.52	0.11	0.030
Jupiter	5.20	318	2.26
Saturn	9.53	95.3	0.11
Uranus	19.2	14.5	0.0020
Neptune	30.1	17.3	0.00063

sine signal DCM model periodogram is shown in Figure 12. The long search grid contains an extremely large number of $n_L = 3000$ tested frequencies, because we do not want to miss any of the inner planet periods. For all shorter periods, the long search z_1 periodogram continuum is nearly constant, between 67.70 and 67.73 (Figure 12: upper panel). The diamond denoting the best detected long search 4.84 year period is at the edge of the tested period interval. The short search grid also contains a large number of $n_S = 1000$ tested frequencies (Figure 12: lower panel). The tested frequency interval is 5% of the full tested long search frequency interval ($c = 0.05$). For the best 11.00 years period denoted with a diamond, the short search periodogram shows a dramatic dip to the level $z_1 = 59$, which is far below the ~ 67.7 continuum of the long search periodogram. This best 11 year “leaking period” is outside the tested period interval upper limit $P_{\text{max}} = 5$ years (“LP”). What we have here is a clearly unstable model case (“UM”).

For the same $P_{\text{min}} = 0.1$ and $P_{\text{max}} = 5$ year interval, the one pure sine signal DCM model for the weighted monthly sunspots **Cmonthly** sample also gives an unstable model result (“LP, UM”).

In our earlier DCM search for periods between 5 and 200 years, we classified the “LP” cases as unstable “UM” models, and stopped searching for additional signals. For the same reason, we can conclude that periods of Mercury, Venus, the Earth and Mars can not be found *directly* from the monthly sunspot data. This does not, however, mean that we can not search for multiples of these periods above the five year limit $P_{\text{max}} = 5$. These periods iP_{Planet} are called “integer multiple periods”, where P_{Planet} is planet’s orbital period and $i = 1, 2, 3\dots$ is an integer.

There are theories of how the tidal forcing of planets may modulate the solar cycle (e.g. Stefani, Giesecke, and Weier, 2019; Cionco, Kudryavtsev, and Soon, 2023). The mass m_{Earth} and major axis a_{Earth} of Earth give the dimensionless relative tidal force

$$R_{\text{Tidal}} = \frac{m}{m_{\text{Earth}}} \left(\frac{a_{\text{Earth}}}{a} \right)^3, \quad (34)$$

exerted by each planet to the Sun, where the planet’s mass is m and its major axis is a . The tidal forces of Mars, Saturn, Neptune and Uranus are negligible (Table 8). Therefore, we search for the periods of Mercury, Venus, the Earth and Jupiter from the detected signals of Table 6.

We have introduced the following nine signal abbreviations S_{11^y} , S_{10^y} , $S_{11.786^y}$, S_{110^y} , $S_{10.76^y}$, $S_{8.74^y}$, S_{53^y} , S_{8^y} and S_{66^y} in Table 6, where these signals were arranged in the order of decreasing strength, or equivalently, decreasing signal amplitude. The numerical value given in the signal subscript refers to the approximate signal period in Earth years.

Table 9. Signals detected in all data samples. (1) Signal parameters. (2-6) Samples: pure sine model ($K_2 = 1$) and double wave models ($K_2 = 2$). Three double sinusoid signals are denoted with “ $2\times$ ”. Notes below give detailed instructions of how to read column (1) signal parameters.

(1)	(2) Rmonthly: $K_2 = 1$	(3) Rmonthly: $K_2 = 2$	(4) Cmonthly: $K_2 = 1$	(5) Ryearly: $K_2 = 1$	(6) Cyearly: $K_2 = 1$
Signal $S_{8y} \cong 13 \times P_{Venus} \cong 8 \times P_{Earth}$					
Rank	(7)	(8)	(5)		(5)
P	8.1087 ± 0.0076	8.169 ± 0.014	8.009 ± 0.017		8.005 ± 0.058
$t_{\min,1}$	1751.29 ± 0.14	1750.90 ± 0.51	1818.07 ± 0.24		1826.09 ± 0.68
$t_{\max,1}$	1755.34 ± 0.14	1754.37 ± 0.26	1822.08 ± 0.24		1822.09 ± 0.70
$P/P_{Mercury}$	33.674 ± 0.032	33.924 ± 0.058	33.260 ± 0.070		33.24 ± 0.24
P/P_{Venus}	13.180 ± 0.012	13.279 ± 0.023	13.018 ± 0.028		13.012 ± 0.094
$P/P_{Jupiter}$	0.68359 ± 0.00064	0.6887 ± 0.0012	0.6752 ± 0.0014		0.6748 ± 0.0049
Signal $S_{8,y,4} \cong 35 \times P_{Mercury}$					
Rank	(6)		(7)		
P	16.753 ± 0.027 ^{2×}		8.466 ± 0.016		
$t_{\min,1}$	1759.19 ± 0.23		1707.10 ± 0.35		
$t_{\max,1}$	1754.70 ± 0.26		1702.86 ± 0.35		
$P/P_{Mercury}$	69.57 ± 0.11 ^{2×}		35.158 ± 0.066		
P/P_{Venus}	27.232 ± 0.044 ^{2×}		13.761 ± 0.026		
$P/P_{Jupiter}$	1.4123 ± 0.0023 ^{2×}		0.7137 ± 0.0013		
Signal $S_{10y} \cong 41.5 \times P_{Mercury} \cong 10 \times P_{Earth}$					
Rank	(2)	(2)	(2)	(2)	(2)
P	10.0001 ± 0.0081	20.0062 ± 0.0088 ^{2×}	10.0659 ± 0.0077	9.975 ± 0.017	10.058 ± 0.026
$t_{\min,1}$	1754.16 ± 0.11	1754.284 ± 0.063	1823.52 ± 0.12	1704.63 ± 0.35	1823.55 ± 0.25
$t_{\max,1}$	1749.16 ± 0.11	1749.282 ± 0.067	1818.48 ± 0.12	1709.62 ± 0.34	1818.52 ± 0.26
$P/P_{Mercury}$	41.529 ± 0.034	83.082 ± 0.036 ^{2×}	41.802 ± 0.032	41.424 ± 0.070	41.77 ± 0.11
P/P_{Venus}	16.255 ± 0.013	32.520 ± 0.014 ^{2×}	16.362 ± 0.012	16.214 ± 0.028	16.349 ± 0.042
$P/P_{Jupiter}$	0.84304 ± 0.00068	1.68658 ± 0.00074 ^{2×}	0.84858 ± 0.00065	0.8409 ± 0.0014	0.8479 ± 0.0022
Signal $S_{10,y,6} \cong 44 \times P_{Mercury}$					
Rank	(5)	(5)		(3)	
P	10.569 ± 0.020	10.5407 ± 0.0060		10.659 ± 0.031	
$t_{\min,1}$	1753.03 ± 0.27	1754.40 ± 0.13		1709.27 ± 0.44	
$t_{\max,1}$	1758.31 ± 0.26	1758.307 ± 0.091		1703.94 ± 0.46	
$P/P_{Mercury}$	43.891 ± 0.083	43.774 ± 0.025		44.26 ± 0.13	
P/P_{Venus}	17.180 ± 0.032	17.1338 ± 0.0098		17.326 ± 0.050	
$P/P_{Jupiter}$	0.89100 ± 0.0017	0.88861 ± 0.00050		0.8986 ± 0.0026	
Signal $S_{11y} \cong 11 \times P_{Earth}$					
Rank	(1)	(1)	(1)	(1)	(1)
P	11.0033 ± 0.0064	10.9878 ± 0.0051	10.8585 ± 0.0048	10.981 ± 0.020	10.863 ± 0.022
$t_{\min,1}$	1755.897 ± 0.076	1756.678 ± 0.077	1823.580 ± 0.053	1700.86 ± 0.24	1823.56 ± 0.20
$t_{\max,1}$	1750.395 ± 0.078	1750.262 ± 0.087	1818.150 ± 0.055	1706.35 ± 0.23	1828.99 ± 0.19
$P/P_{Mercury}$	45.695 ± 0.026	45.630 ± 0.021	45.093 ± 0.020	45.602 ± 0.083	45.112 ± 0.091
P/P_{Venus}	17.886 ± 0.010	17.8605 ± 0.0083	17.6504 ± 0.0078	17.849 ± 0.032	17.658 ± 0.036
$P/P_{Jupiter}$	0.92761 ± 0.00054	0.92630 ± 0.00043	0.91540 ± 0.00040	0.9257 ± 0.0017	0.9158 ± 0.0018
Signal $S_{11,y,86} \cong 49 \times P_{Mercury} \cong 1 \times P_{Jupiter}$					
(3)	(4)	(4)	(5)		(4)
P	11.806 ± 0.012	11.770 ± 0.011	11.863 ± 0.021	11.820 ± 0.027	11.856 ± 0.068
$t_{\min,1}$	1760.33 ± 0.13	1749.51 ± 0.15	1818.92 ± 0.20	1701.01 ± 0.41	1818.95 ± 0.69
$t_{\max,1}$	1754.42 ± 0.14	1754.40 ± 0.21	1824.85 ± 0.19	1706.92 ± 0.41	1824.88 ± 0.66
$P/P_{Mercury}$	49.028 ± 0.050	48.879 ± 0.046	49.265 ± 0.087	49.09 ± 0.11	49.24 ± 0.28
P/P_{Venus}	19.190 ± 0.020	19.132 ± 0.018	19.283 ± 0.034	19.213 ± 0.044	19.27 ± 0.11
$P/P_{Jupiter}$	0.9953 ± 0.0010	0.99224 ± 0.00093	1.0001 ± 0.0018	0.9964 ± 0.0023	0.9995 ± 0.0057
Signal $S_{53y} \cong 4.5 P_{Jupiter}$					
Rank	(6)			(6)	
P	52.66 ± 0.27			53.83 ± 0.76	
$t_{\min,1}$	1759.63 ± 0.70			1704.5 ± 2.7	
$t_{\max,1}$	1785.94 ± 0.60			1731.4 ± 2.3	
$P/P_{Mercury}$	218.7 ± 1.1			223.5 ± 3.2	
P/P_{Venus}	85.60 ± 0.44			87.5 ± 1.2	
$P/P_{Jupiter}$	4.439 ± 0.023			4.538 ± 0.064	
Signal $S_{66y} \cong 5.5 \times P_{Jupiter}$ or $6.0 \times P_{Jupiter}$					
Rank	(7)		(8)		
P	143.39 ± 0.99 ^{2×}		66.7 ± 1.4		
$t_{\min,1}$	1887.84 ± 0.80		1753.0 ± 3.8		
$t_{\max,1}$	1784.2 ± 1.1		1719.6 ± 4.4		
$P/P_{Mercury}$	595.5 ± 4.1 ^{2×}		277.0 ± 5.8		
P/P_{Venus}	233.1 ± 1.6 ^{2×}		108.4 ± 2.3		
$P/P_{Jupiter}$	12.088 ± 0.083 ^{2×}		5.62 ± 0.12		
Signal $S_{110y} \cong$ Synodic periods of Equation 47 (Table 11)					
(4)	(3)	(3)	(4)		(3)
P	99.92 ± 0.57	104.23 ± 0.68	116.7 ± 1.3	101.4 ± 2.4	115.6 ± 3.6
$t_{\min,1}$	1811.99 ± 0.84	1811.37 ± 0.68	1911.02 ± 0.74	1710.5 ± 3.4	1910.4 ± 2.1
$t_{\max,1}$	1762.0 ± 1.1	1844.00 ± 0.48	1852.7 ± 1.1	1761.2 ± 2.5	1852.6 ± 2.6
$P/P_{Mercury}$	415.0 ± 2.4	432.8 ± 2.8	484.6 ± 5.4	421 ± 10	480 ± 15
P/P_{Venus}	162.42 ± 0.93	169.4 ± 1.1	189.7 ± 2.1	164.8 ± 3.9	187.9 ± 5.8
$P/P_{Jupiter}$	8.424 ± 0.048	8.787 ± 0.057	9.84 ± 0.11	8.55 ± 0.20	9.74 ± 0.30

Notes. Column 1 specifies seven parameters for each sample. For example, seventh strongest “(7)” signal S_{8y} for Rmonthly ($K_2 = 1$) has period $P \pm \sigma_P = 8.1087 \pm 0.0076$ in Earth years. Primary minima and maxima of this signal are at years $t_{\min,1} = 1751.29 \pm 0.14$ and $t_{\max,1} = 1755.34 \pm 0.14$. Rounds $P \pm \sigma_P$ values are $(P \pm \sigma_P)/P_{Mercury} = 33.674 \pm 0.032$, $(P \pm \sigma_P)/P_{Venus} = 13.180 \pm 0.012$ and $(P \pm \sigma_P)/P_{Jupiter} = 0.68359 \pm 0.00064$.

Table 10. Detected planetary signal candidates. (1) Sample ($K_2 = 1 \equiv$ pure sine model, $K_2 = 2 \equiv$ double wave model), (2) Time span. (3) Period. (4) Rounds (Equations 35 and 36). (5) Rounds deviation (Equation 37). (6) Relative rounds deviation (Equation 38). (7) Mean anomaly migration $\Delta M/360^\circ$ (Equation 43). (8) Planet revolutions during ΔT . (9) Relative mean anomaly migration $\Delta M/360^\circ$ (Equation 44). (10) Displaying figure and symbol colour.

(1) Sample (K_2)	(2) ΔT (y)	(3) $P \pm \sigma_P$ (y)	(4) $\mathcal{P} \pm \sigma_{\mathcal{P}}$ (-)	(5) $\Delta \mathcal{P}$ (-)	(6) $\Delta \mathcal{P}_{\text{rel}}$ (-)	(7) $\frac{\Delta M}{360^\circ}$ (-)	(8) $\frac{\Delta T}{P_{\text{Planet}}}$ (-)	(9) $\frac{\Delta M_{\text{rel}}}{360^\circ}$ (-)	(10) Figure
Signal $S_{8y}: \cong 13 \times P_{\text{Venus}}$									
Rmonthly($K_2 = 1$)	273.8	8.1087 ± 0.0076	13.180 ± 0.012	0.180	15.0	6.1	445	0.014	13a: red
Rmonthly($K_2 = 2$)	273.8	8.169 ± 0.014	13.279 ± 0.023	0.279	12.1	9.4	445	0.021	13a: blue
Cmonthly($K_2 = 1$)	204.8	8.009 ± 0.017	13.018 ± 0.028	0.018	0.90	0.46	333	0.0014	13a: green
Cyearly($K_2 = 1$)	203.0	8.005 ± 0.058	13.012 ± 0.094	0.012	0.13	0.30	330	0.00092	13a: cyan
Signal $S_{8y}: \cong 8 \times P_{\text{Earth}}$									
Rmonthly($K_2 = 1$)	273.8	8.1087 ± 0.0076	8.1087 ± 0.0076	0.1087	14.3	3.7	273.8	0.013	13b: red
Rmonthly($K_2 = 2$)	273.8	8.169 ± 0.014	8.169 ± 0.014	0.169	12.1	5.7	273.8	0.021	13b: blue
Cmonthly($K_2 = 1$)	204.8	8.009 ± 0.017	8.009 ± 0.017	0.009	0.53	0.23	204.8	0.0011	13b: green
b Cyearly($K_2 = 1$)	203.0	8.005 ± 0.058	8.005 ± 0.058	0.005	0.086	0.13	203.0	0.00062	13b: cyan
Signal $S_{8,y4}: \cong 35 \times P_{\text{Mercury}}$									
Ryearly($K_1 = 1$)	321.0	8.466 ± 0.016	35.158 ± 0.066	0.158	2.4	6.0	1333	0.0045	None
Signal $S_{10y}: 41.5 \times P_{\text{Mercury}}$									
Rmonthly($K_2 = 1$)	273.8	10.0001 ± 0.0081	41.529 ± 0.034	0.029	0.85	0.79	1137	0.00070	13c: red
Cmonthly($K_2 = 1$)	204.8	10.0659 ± 0.0077	41.802 ± 0.032	0.302	9.4	6.2	851	0.0072	13c: green
Ryearly($K_2 = 1$)	321.0	9.975 ± 0.017	41.424 ± 0.070	-0.076	1.1	-2.4	1333	0.0018	13c: yellow
Cyearly($K_2 = 1$)	203.0	10.058 ± 0.026	41.77 ± 0.11	0.27	2.4	5.4	843	0.0065	13c: cyan
Signal $S_{10y}: \cong 10.0 \times P_{\text{Earth}}$									
Rmonthly($K_2 = 1$)	273.8	10.0001 ± 0.0081	10.0001 ± 0.0081	0.0001	0.012	0.0027	273.8	0.000010	13d: red
Cmonthly($K_2 = 1$)	204.8	10.0659 ± 0.0077	10.0659 ± 0.0077	0.0659	8.6	1.3	204.8	0.0065	13d: green
Ryearly($K_2 = 1$)	321.0	9.975 ± 0.017	9.975 ± 0.017	-0.025	1.5	-0.80	321	0.0025	13d: yellow
Cyearly($K_2 = 1$)	203.0	10.058 ± 0.026	10.058 ± 0.026	0.058	2.3	1.2	203	0.0058	13d: cyan
Signal $S_{10,y6}: \cong 44 \times P_{\text{Mercury}}$									
Rmonthly($K_2 = 1$)	273.8	10.569 ± 0.020	43.891 ± 0.083	-0.109	1.3	-2.8	1137	0.0025	14a: red
Rmonthly($K_2 = 2$)	273.8	10.5407 ± 0.0060	43.774 ± 0.025	-0.226	9.0	-5.9	1137	0.0052	14a: blue
Ryearly($K_2 = 1$)	321.0	10.659 ± 0.031	44.26 ± 0.13	0.26	2.0	7.8	1333	0.0059	14a: yellow
Signal $S_{11y}: \cong 11.0 \times P_{\text{Earth}}$									
Rmonthly($K_2 = 1$)	273.8	11.0033 ± 0.0064	11.0033 ± 0.0064	0.0033	0.52	0.082	273.8	0.00030	14b: red
Rmonthly($K_2 = 2$)	273.8	10.9878 ± 0.0051	10.9878 ± 0.0051	-0.0122	2.4	-0.30	273.8	0.0011	14b: blue
Cmonthly($K_2 = 1$)	204.8	10.8585 ± 0.0048	10.8585 ± 0.0048	-0.1415	29	-2.7	204.8	0.013	14b: green
Ryearly($K_2 = 1$)	321.0	10.981 ± 0.020	10.981 ± 0.020	-0.019	0.95	0.56	321.0	0.0017	14b: yellow
Cyearly($K_2 = 1$)	203.0	10.863 ± 0.022	10.863 ± 0.022	-0.137	6.2	-2.6	203.0	0.013	14b: cyan
Signal $S_{11,y86}: \cong 49.0 \times P_{\text{Mercury}}$									
Rmonthly($K_2 = 1$)	273.8	11.806 ± 0.012	49.028 ± 0.050	0.028	0.56	0.65	1137	0.00057	14c: red
Rmonthly($K_2 = 2$)	273.8	11.770 ± 0.011	48.879 ± 0.046	-0.121	2.6	-2.8	1137	0.0025	14c: blue
Cmonthly($K_2 = 1$)	204.8	11.863 ± 0.021	49.265 ± 0.087	0.265	3.0	4.6	850	0.0054	14c: green
Ryearly($K_2 = 1$)	321.0	11.820 ± 0.027	49.09 ± 0.11	0.09	0.82	2.4	1333	0.0018	14c: yellow
Cyearly($K_2 = 1$)	203.0	11.856 ± 0.068	49.24 ± 0.28	0.24	0.86	4.1	843	0.0049	14c: cyan
Signal $S_{11,y86}: \cong 1.0 \times P_{\text{Jupiter}}$									
Rmonthly($K_2 = 1$)	273.8	11.806 ± 0.012	0.9953 ± 0.0010	-0.0047	4.7	-0.11	23	0.0047	14d: red
Rmonthly($K_2 = 2$)	273.8	11.770 ± 0.011	0.99224 ± 0.00093	-0.0078	8.3	-0.18	23	0.0078	14d: blue
Cmonthly($K_2 = 1$)	204.8	11.863 ± 0.021	1.0001 ± 0.0018	0.00010	0.056	0.0017	17	0.00010	14d: green
Ryearly($K_2 = 1$)	321.0	11.820 ± 0.027	0.9964 ± 0.0023	-0.0036	1.6	-0.098	27	0.0036	14d: yellow
Cyearly($K_2 = 1$)	203.0	11.856 ± 0.068	0.9995 ± 0.0057	-0.00050	0.088	-0.0086	17	0.00050	14d: cyan
Signal $S_{53y}: \cong 4.5 \times P_{\text{Jupiter}}$									
Rmonthly($K_2 = 1$)	273.8	52.66 ± 0.27	4.439 ± 0.023	-0.061	2.6	-0.32	23	0.014	None
Ryearly($K_2 = 1$)	321.0	53.83 ± 0.76	4.538 ± 0.064	0.038	0.59	0.23	27	0.0084	None
Signal $S_{66y}: \cong 5.5 \times P_{\text{Jupiter}}$									
Ryearly($K_2 = 1$)	321.0	66.7 ± 1.4	5.62 ± 0.12	0.12	1.0	0.57	27	0.021	None

These nine signals are now rearranged into the order of increasing periods S_{8y} , $S_{8.y4}$, S_{10y} , $S_{10.y6}$, S_{11y} , $S_{11.y86}$, S_{53y} , S_{66y} and S_{110y} in our next Tables 9 and 10. We study only the signals detected in all data samples, because we get the same results for the predictive data samples (i.e., the subsets of all data samples). We select only those all data samples, where DCM detects more than two signals. The period (P), the primary minimum epoch ($t_{\min,1}$) and the primary maximum epoch ($t_{\max,1}$) of all S_{8y} , $S_{8.y4}$, S_{10y} , $S_{10.y6}$, S_{11y} , $S_{11.y86}$, S_{53y} , S_{66y} and S_{110y} signals are given in Table 9. The units of these three parameters are Earth years.

We are accustomed to measuring time and periodicity in Earth years. The Earth year signal periods detected in all data samples are transformed into Mercury, Venus and Jupiter year signal periods in Tables 9 and 10. It is easier to identify integer multiple periods from these values. We use the known planet period P_{Planet} in Earth years to compute four dimensionless parameters

$$\mathcal{P} = P/P_{\text{Planet}} \quad (35)$$

$$\sigma_{\mathcal{P}} = \sigma_P/P_{\text{Planet}} \quad (36)$$

$$\Delta\mathcal{P} = \mathcal{P} - \mathcal{P}_0 \quad (37)$$

$$\Delta\mathcal{P}_{\text{rel}} = \frac{|\Delta\mathcal{P}|}{\sigma_{\mathcal{P}}}, \quad (38)$$

where \mathcal{P}_0 is the integer value closest to \mathcal{P} . The two first parameters $\sigma_{\mathcal{P}}$ and \mathcal{P} are hereafter called “rounds error” and “rounds” (number of planet revolutions around the Sun). The next two parameters $\Delta\mathcal{P}$ and $\Delta\mathcal{P}_{\text{rel}}$ are called “rounds deviation” and “relative rounds deviation”. Note that we introduce a new letter “ \mathcal{P} ” to highlight the difference from the period letter “ P ”.

For any detected period $P \pm \sigma_P$, the rounds error is $\sigma_{\mathcal{P}} \propto \sigma_P/P_{\text{Planet}}$. This rounds error $\sigma_{\mathcal{P}}$ is larger for the inner planets Mercury and Venus having $P_{\text{Planet}} < P_{\text{Earth}} = 1$, and smaller for Jupiter having $P_{\text{Planet}} > P_{\text{Earth}} = 1$. For example, the period $P = 8.1087 \pm 0.0076$ gives the following $\sigma_{\mathcal{P}} = 0.032$ (Mercury), $\sigma_{\mathcal{P}} = 0.012$ (Venus), $\sigma_{\mathcal{P}} = 0.0076$ (Earth) and $\sigma_{\mathcal{P}} = 0.000064$ (Jupiter) rounds error values (Table 9: `Rmonthly`, $K_2 = 1$ model, signal S_{8y}). This means that the period of Jupiter is easiest to identify from the \mathcal{P} rounds values. On the other hand, the identifications of Mercury and Venus from the \mathcal{P} rounds values are the most difficult ones, and especially in this order. Furthermore, the correct \mathcal{P}_0 rounds value becomes uncertain, if the round error $\sigma_{\mathcal{P}}$ exceeds $1/2$, i.e. half a revolution around the Sun. This complication effect is strongest for the longest detected periods P , which have the largest $\sigma_{\mathcal{P}}$ errors in Tables 9 and 10.

The larger rounds error $\sigma_{\mathcal{P}}$ values of Mercury and Venus cause another effect that makes the identification of their signals even more difficult. If the rounds deviation $\Delta\mathcal{P}$ values are drawn from a Gaussian distribution having a mean \mathcal{P}_0 and a standard deviation $\sigma_{\mathcal{P}}$, the probability

$$P(|\Delta\mathcal{P}| \geq |\Delta\mathcal{P}'|) \quad (39)$$

for $|\Delta\mathcal{P}|$ exceeding any fixed large rounds deviation $|\Delta\mathcal{P}'|$ value increases for larger rounds error $\sigma_{\mathcal{P}}$ values. In other words, large $|\Delta\mathcal{P}|$ values are more probable for Mercury and Venus than for the Earth and Jupiter. This increases the probability of stronger mean anomaly migration ΔM for Mercury and Venus (see Equation 43).

The primary minima and the primary maxima of the signals in Table 9 occur at multiples

$$T_{\min,k} = t_{\min,1} + kP \quad (40)$$

$$T_{\max,k} = t_{\max,1} + kP, \quad (41)$$

where $k = 1, 2, \dots$ are integers. The units of P , $t_{\min,1}$ and $t_{\max,1}$ are Earth years. The relation $P = (\mathcal{P}_0 + \Delta\mathcal{P})P_{\text{Planet}}$ gives

$$\begin{aligned} T_{\min,k} &= t_{\min,1} + kP = t_{\min,1} + k(\mathcal{P}_0 + \Delta\mathcal{P})P_{\text{Planet}} = t_{\min,1} + k\mathcal{P}_0P_{\text{Planet}} + k\Delta\mathcal{P}P_{\text{Planet}} \\ T_{\max,k} &= t_{\max,1} + kP = t_{\max,1} + k(\mathcal{P}_0 + \Delta\mathcal{P})P_{\text{Planet}} = t_{\max,1} + k\mathcal{P}_0P_{\text{Planet}} + k\Delta\mathcal{P}P_{\text{Planet}} \end{aligned}$$

The last term

$$\Delta t = k\Delta\mathcal{P}P_{\text{Planet}} \quad (42)$$

is the time difference between the multiples $t_{\min,1} + kP$ and $t_{\min,1} + k\mathcal{P}_0P_{\text{Planet}}$, and between the multiples $t_{\max,1} + kP$ and $t_{\max,1} + k\mathcal{P}_0P_{\text{Planet}}$.

The data time span ΔT contains $\Delta T/P$ multiples of P . Using $k = \Delta T/P$ in Equation 42 gives

$$\Delta t = \frac{\Delta\mathcal{P}\Delta T}{P}P_{\text{Planet}}$$

time difference during ΔT . We convert time difference Δt into planet “mean anomaly migration”

$$\Delta M = \frac{\Delta t}{P_{\text{Planet}}} \times 360^\circ = \frac{\Delta\mathcal{P}\Delta T}{P} \times 360^\circ, \quad (43)$$

where the units of ΔM are degrees. For all ΔT and P combinations, this relation shows that larger mean anomaly ΔM migration occurs for larger $\Delta\mathcal{P}$ values, which are most probable for Mercury and Venus (Equation 39). The “relative mean anomaly migration” during each P_{Planet} revolution is

$$\Delta M_{\text{rel}} = |\Delta M| / \left(\frac{\Delta T}{P_{\text{Planet}}} \right) \times 360^\circ = |\Delta\mathcal{P}| \frac{P_{\text{Planet}}}{P} \times 360^\circ. \quad (44)$$

For any particular signal, the period P detected in each sample determines the linear mean anomaly migration ΔM during the ΔT time span of the data (Equation 43). The slope of this linear $M(t)$ mean anomaly migration is $(\Delta\mathcal{P}/P) \times 360^\circ$ (Equation 43). Let us assume that these mean anomaly migration lines

$$\frac{\Delta\mathcal{P}}{P}(t - t_C) \times 360^\circ = M(t) - M_C \quad (45)$$

of different samples intersect close to a “convergence point” (t_C, M_C) . This means that the mean anomaly value of each line is $M(t) \approx M_C$ at epoch $t = t_C$. The slope of all these $M(t)$ lines approaches zero, if $\Delta\mathcal{P} \rightarrow 0 \equiv \mathcal{P} \rightarrow \mathcal{P}_0 \equiv P \rightarrow P_{\text{planet}}$. In this case, all lines fulfil

$$M(t) \approx M_C \quad (46)$$

for all t values. If the mean anomaly $M(t)$ lines for the same signal are detected in different samples, and these lines show a convergence point (t_C, M_C) , then the periods P , the minimum epochs $t_{\min,1}$ and the maximum epochs $t_{\max,1}$ of all these signals can be connected to each other. The presence of this convergence point confirms that the individual signals detected in different samples can represent the same real signal having the same period, and the same phase. The statistical fluctuation of $|\Delta\mathcal{P}|$ rounds deviations (Equation 39) complicate the detection of this “convergence point connection”. We have already shown that the probability for larger $|\Delta\mathcal{P}|$ values increases when $\sigma_{\mathcal{P}}$ increases for smaller P_{Planet} periods. These $|\Delta\mathcal{P}|$ fluctuations are largest for Mercury and Venus. Therefore, the mean anomaly migration ΔM lines of these inner

planets are “messier”, and their convergence point locations are more difficult to detect. Hence, the detection of Jupiter and the Earth from the *same* sunspot data is easier than the detection of Venus and Mercury.

The relations of Equations 43 - 46 are formulated for the mean anomaly M , because this parameter has a linear connection to time. We compute the true anomaly ν_{\min} and ν_{\max} values from the mean anomaly values M for the minimum epochs $t_{\min,1}$ and the maximum epochs $t_{\max,1}$ (Equations 40 and 41) given in Table 9. The mean anomaly M and the true anomaly ν value differences are small for Venus, the Earth and Jupiter, which have nearly circular orbits. The large Mercury’s orbit eccentricity $e = 0.20$ can cause clear ν deviations from the linear M trend (e.g. Figure 14c).

We search for signatures of Mercury, Venus, the Earth and Jupiter from the S_{8y} , $S_{8,y4}$, S_{10y} , $S_{10,y6}$, S_{11y} , $S_{11,y86}$, S_{53y} , S_{66y} and S_{110y} signals. The results for this “wide search” of 36 alternatives are given in Table 9. We summarise the most promising planetary signal candidate detections in Table 10. The three double sinusoid signals “ $2\times$ ” are given in Table 9. We exclude these double sinusoids from Table 10, because the minor asymmetries of these double sinusoid $2 \times P$ period curves can mislead the identification of convergence points (Equation 45).

In our next figures, we plot the ν_{\min} and ν_{\max} values for numerous sample, signal and planet combinations. In every figure, we use the same symbol colour for the signals detected in the same sample. All samples end in the same year 2022, but they begin at different years between 1700 and 1815. This complicates the detection of convergence points, if they are located outside some sample(s). We solve this problem by computing the ν_{\min} and ν_{\max} values of all samples for the whole time interval between the years 1700 and 2022. The symbols for the ν_{\min} and ν_{\max} values *inside* each sample are highlighted with a black circle around the coloured symbol. This black circle is missing from the symbols representing ν_{\min} and ν_{\max} values *outside* each sample. We can use these outside values to check, if the signals detected in each sample can predict the presence of a convergence point before the beginning of this sample.

The detected signals are the $h_i(t)$ functions (Equation 7) in the sum $h(t)$ of all signals (Equation 6). For the symmetric pure sine model $h_i(t)$ functions, the separation between the primary minimum epoch $t_{\min,1}$ and the primary maximum epoch $t_{\max,1}$ is exactly $P/2$. If the period of the detected signal P is an *even* multiple of the planet’s period P_{Planet} , the mean anomaly M values are equal at all minima $T_{\min,k}$ and maxima $T_{\max,k}$ (Equations 40 and 41). Except for the possible deviations caused by the planetary orbit eccentricity, the ν_{\min} and ν_{\max} values will also be equal. This “overlapping effect” occurs in Figures 13b, 13d and 14a. If the detected period P is an *uneven* P_{Planet} multiple, the differences between the mean anomaly M values of all minima $T_{\min,k}$ and maxima $T_{\max,k}$ are equal to 180 degrees. The planetary orbit eccentricity can, again, cause deviations from this 180 degrees difference between the true anomalies ν_{\min} and ν_{\max} . This 180 degrees “separation effect” occurs in Figures 13a, 14b, 14c and 14d. The asymmetries of double wave models can also cause deviations from the overlapping effect and 180 degrees separation effect, like those seen in the blue circles of Figures 13b, 14a, 14b and 14d.

7.2. Signal S_{8y}

The shortest period S_{8y} signal is close to $13 \times P_{\text{Venus}}$ and $8 \times P_{\text{Earth}}$ (Tables 9 and 10). The known period ratio is $8 \times P_{\text{Earth}}/P_{\text{Venus}} = 13.0039$. Due to statistical $\Delta\mathcal{P}$ fluctuations (Equations 39 and 43), the true anomaly migration curves of Venus in Figure 13a should appear less regular than those of Earth in Figure 13b. This is indeed the case.

7.2.1. Signal $S_{8y} \cong 13 \times P_{\text{Venus}}$

The two rounds $\mathcal{P} = 13.018 \pm 0.028$ and 13.012 ± 0.094 values for the Cmonthly and Cyearly samples differ $\Delta\mathcal{P}_{\text{rel}} = 0.90$ and 0.13 from $13 \times P_{\text{Venus}}$ (Table 10: Signal S_{8y}). The mean anomaly

migration is $\Delta M/360^\circ = 0.46$ and 0.30 revolutions during 205 and 203 years, respectively. The green and cyan circles highlighted with black circles show this weak positive upwards ν_{\min} and ν_{\max} true anomaly migration of Venus inside these **Cmonthly** and **Cyearly** samples (Figure 13a).

The other two rounds values for sample **Rmonthly** (pure sine and double wave models) are $\mathcal{P} = 13.180 \pm 0.012$ and 13.279 ± 0.023 . They differ $\Delta\mathcal{P}_{\text{rel}} = 15.0$ and 12.1 from $13 \times P_{\text{Venus}}$ (Table 10: Signal S_{8y}). For these two \mathcal{P} rounds values, the strong positive upwards mean anomaly migration $\Delta M/360^\circ$ is 6.1 and 9.4 revolutions during 274 years $\equiv 445$ Venus revolutions. These values are equal to the relative mean anomaly migration $\Delta M_{\text{rel}}/360^\circ = 0.014$ and 0.021 during one revolution of Venus. We show the respective true anomaly ν_{\min} and ν_{\max} migration in Figure 13a (red and blue circles).

The uneven $13 \times P_{\text{Venus}}$ multiple causes the 180 degree separation effect of ν_{\min} and ν_{\max} . The migration lines of large circles denoting the ν_{\max} values show a convergence point (Equation 45), which is highlighted with a large dotted blue circle at $t_C = 1820$ years and $\nu_C = 315$ degrees. The migration lines of smaller circles denoting the ν_{\min} values converge at $t_C = 1820$ years and $\nu_C = 135$ degrees in the centre of the red large dotted circle. These two convergence points are at the beginning of **Cmonthly** and **Cyearly** samples, where the black circles begin to highlight the green and cyan circles. The detection of the two convergence points confirms that all four S_{8y} signals in Table 10 can be connected, regardless of the large true anomaly ν migration of the two signals detected in **Rmonthly** (pure sine and double wave models). The apparently messy migration of red and blue circles in Figure 13a can arise, as expected, from the statistical $\Delta\mathcal{P}$ fluctuations caused by the short orbital period of Venus (Equation 39).

7.2.2. Signal $S_{8y} \cong 8 \times P_{\text{Earth}}$

The two $P \pm \sigma_P = 8.009 \pm 0.017$ and 8.005 ± 0.058 Earth year periods detected in the **Cmonthly** and **Cyearly** samples are equal to $8 \times P_{\text{Earth}}$ comfortably within $\pm 1\sigma_{\mathcal{P}}$ (Table 10: Signal S_{8y}). The mean anomaly migration $\Delta M/360^\circ$ is only 0.23 and 0.13 revolutions in over two centuries (Figure 13b: green and cyan highlighted circles).

For the other two periods (**Rmonthly**: pure sine and double wave models), the rounds values $\mathcal{P} = 8.1087 \pm 0.0076$ and 8.169 ± 0.014 differ $\Delta\mathcal{P}_{\text{rel}} = 14.3$ and 12.1 from $8 \times P_{\text{Earth}}$ (Table 10: Signal S_{8y}). The respective ΔM_{rel} relative mean anomaly migration values are 0.013 and 0.021 during one revolution of Earth. Hence, these true anomaly ν_{\min} and ν_{\max} values of Earth migrate about 3.7 and 5.7 revolutions during 274 years (Figure 13b: red and blue highlighted circles).

For the three symmetric pure sine models, the true anomaly ν_{\min} and ν_{\max} lines show the overlapping effect, because $8 \times P_{\text{Earth}}$ in an even number multiple (Figure 13b: red, green and cyan symbols). Due to the asymmetric signal S_{8y} shape of the double wave model for sample **Rmonthly**, the lines of small and large blue circles do not overlap.

The true anomaly ν_{\min} and ν_{\max} migration curves of Earth converge in the centre of the blue and red dotted circles at $t_C = 1815$ years and $\nu = 25$ degrees (Figure 13b). Due to the aforementioned double wave signal asymmetry, the line of large blue circles deviates from the converging line of small blue circles. Although the convergence point is *outside* samples **Cmonthly** and **Cyearly**, it is nicely covered by the “predictive” green and cyan symbols not highlighted with black circles. We can identify this convergence point regardless of the large true anomaly migration of the pure sine model and the double wave model for sample **Rmonthly**. This means that all four S_{8y} signals’ period (P), primary minimum ($t_{\min,1}$) and primary maximum ($t_{\max,1}$) values for different samples in Table 9 can be connected to the same signal.

We detect the convergence points for the signal candidates of both Venus and the Earth. This indicates that the repetitive relative motions of these two planets may cause this S_{8y} signal.

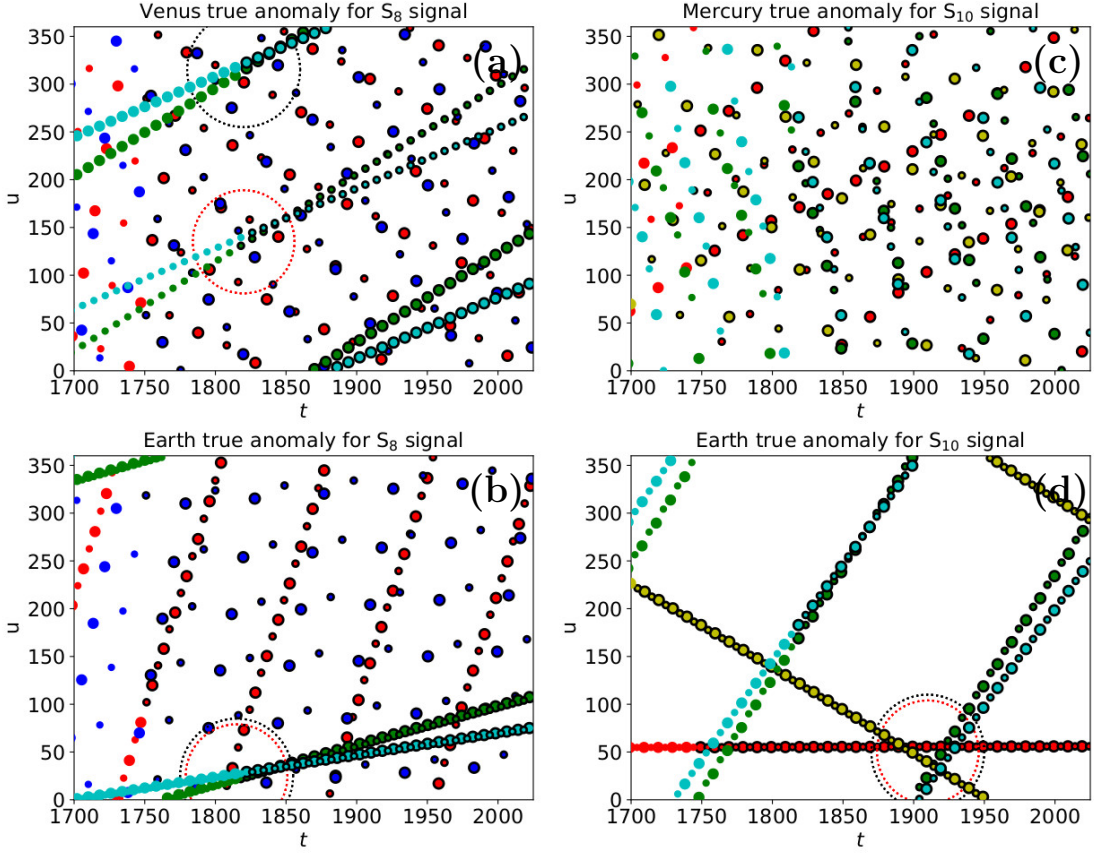


Figure 13. True anomalies ν_{\min} (small circles) and ν_{\max} (large circles) for time point multiples $T_{\min,k}$ and $T_{\max,k}$ (Equations 40 and 41). We compute these multiples from periods (P), primary minimum epochs ($t_{\min,1}$) and primary maximum epochs ($t_{\max,1}$) given in Table 9. Symbol colours for different samples are red (Rmonthly : pure sines), blue (Rmonthly : double waves), green (Cmonthly : pure sines), yellow (Ryearly : pure sines), and cyan (Cyearly : pure sines). Symbols for ν_{\min} and ν_{\max} values inside each sample are highlighted with a black circle. (a) Venus' true anomalies for signal S_{8y} . (b) Earth's true anomalies for signal S_{8y} . (c) Mercury's true anomalies for signal S_{10y} . (d) Earth's true anomalies for signal S_{10y} . Units of X-axis and Y-axis are years and degrees, respectively.

7.3. Signal $S_{8,y4} \cong 35 \times P_{\text{Mercury}}$

This sixth-strongest signal is detected only in sample Ryearly (Table 10: Signal $S_{8,y4}$). The rounds value $\mathcal{P} = 35.158 \pm 0.066$ deviates $\Delta\mathcal{P}_{\text{rel}} = 2.4$ from $35 \times P_{\text{Mercury}}$. We want to draw attention to this $S_{8,y4}$ signal, because the $\mathcal{P} = 69.57 \pm 0.11$ rounds value of another signal, the double sinusoid signal for sample Rmonthly ($K_2 = 2$), is quite close to $2 \times 35 \times P_{\text{Mercury}}$ (Table 9: Signal $S_{8,y4}$). We show no figure for this $S_{8,y4}$ signal candidate of Mercury, because one migration line can not have a convergence point.

7.4. Signal S_{10y}

The second-strongest signal S_{10y} period is approximately $41.5 \times P_{\text{Mercury}}$ and $10 \times P_{\text{Earth}}$. The known ratio is $10 \times P_{\text{Earth}}/P_{\text{Mercury}} = 45.528$. Considering the statistical $|\Delta\mathcal{P}|$ fluctuations (Equations 39 and 43), the expected migration curves of Mercury should be much messier than

those of the Earth. These expectations are “amply rewarded” when Figures 13c and 13d are compared.

7.4.1. Signal $S_{10y} \cong 41.5 \times P_{\text{Mercury}}$

For clarity, as well as to avoid possible misunderstandings, we define \mathcal{P}_0 in Equation 37 as the integer closest to \mathcal{P} . The combined tidal forces of two planets are strongest when they are aligned to the same line with respect to the Sun. This can happen when these planets are at the same side, or at opposite sides, of the Sun. Therefore, the connection $\mathcal{P}_0 \cong 41.5 \times P_{\text{Mercury}}$ draws our attention.

The true anomaly ν_{\min} and ν_{\max} migration curves for Mercury appear truly messy (Figure 13c). These true anomaly migration curves are not fully linear due to the large eccentricity of Mercury’s orbit. However, the reason for the messy impression is not eccentricity or strong migration, because even the largest relative mean anomaly migration is only $\Delta M_{\text{rel}} = 6.2$ revolutions in a total of 851 revolutions during over two centuries (Table 10: Sample **Cmonthly**). The $41.5 \times P_{\text{Mercury}}$ value divides all ν_{\min} and ν_{\max} true anomaly curves into two parts. First part contains uneven multiples of $41.5 \times P_{\text{Mercury}}$ revolutions, and the second part contains even multiples of $83 = 2 \times 41.5 \times P_{\text{Mercury}}$ revolutions. The true anomaly difference between these two parts is about half a revolution. This division effect causes the messy impression in Figure 13c. It would make no sense to search for a convergence point (Equation 45) from this mixture of true anomaly lines.

For one sample **Cmonthly**, this planetary signal candidate can be questioned, because the rounds $\mathcal{P} = 41.802 \pm 0.032$ value having $\Delta\mathcal{P}_{\text{rel}} = 9.4$ differs strongly from $41.5 \times P_{\text{Mercury}}$ (Table 10: Signal S_{10y}). However, the relative rounds deviation values for the other three samples, $0.85 \leq \Delta\mathcal{P}_{\text{rel}} \leq 2.4$, support the $41.5 \times P_{\text{Mercury}}$ relation. The signal detection $\mathcal{P} = 41.529 \pm 0.034$ for sample **Rmonthly** is extremely accurate, only $\Delta M_{\text{rel}} = 0.00070$ during one revolution of Mercury. The mean anomaly migration of the respective highlighted red circles is only 0.79 revolutions during 1137 revolutions (Figure 13c).

7.4.2. Signal $S_{10y} \cong 10 \times P_{\text{Earth}}$

The relative rounds deviation $\Delta\mathcal{P}_{\text{rel}} = 0.012, 1.5$ and 2.3 values of three samples support the $10 \times P_{\text{Earth}}$ relation for S_{10y} signal (Table 10: **Rmonthly**, **Ryearly**, **Cyearly**). For the fourth sample **Cmonthly**, the rounds $\mathcal{P} = 10.0659 \pm 0.0077$ value has a large relative rounds deviation $\Delta\mathcal{P}_{\text{rel}} = 8.6$. However, the mean anomaly migration $|\Delta M/360^\circ|$ values for all four samples are smaller than 1.3 revolutions during two, or even three, centuries.

The true anomaly ν_{\min} and ν_{\max} migration curves of Earth are exceptionally clear (Figure 13d). The lines of small and large circles of every sample show the overlapping effect caused by the even number $10 \times P_{\text{Earth}}$ multiple. This overlapping effect is even more pronounced than in Figure 13b, because the results for all four samples are based on pure sine models. The true anomaly ν_{\min} and ν_{\max} migration convergence point of all four signals is at $t_C = 1910$ years and $\nu \approx M_C = 50$ degrees (Figure 13d: centre of blue and red dotted circles). This convergence point is *inside* all four samples. All these four S_{10y} signals in different samples can undoubtedly originate from one and the same signal.

7.5. Signal $S_{10,y6} \cong 44 \times P_{\text{Mercury}}$

The signal $S_{10,y6}$ period is close to $44 \times P_{\text{Mercury}} = 10.595$ years. The identification of the convergence point of this signal is quite complicated. It is not easy to perceive the correct true

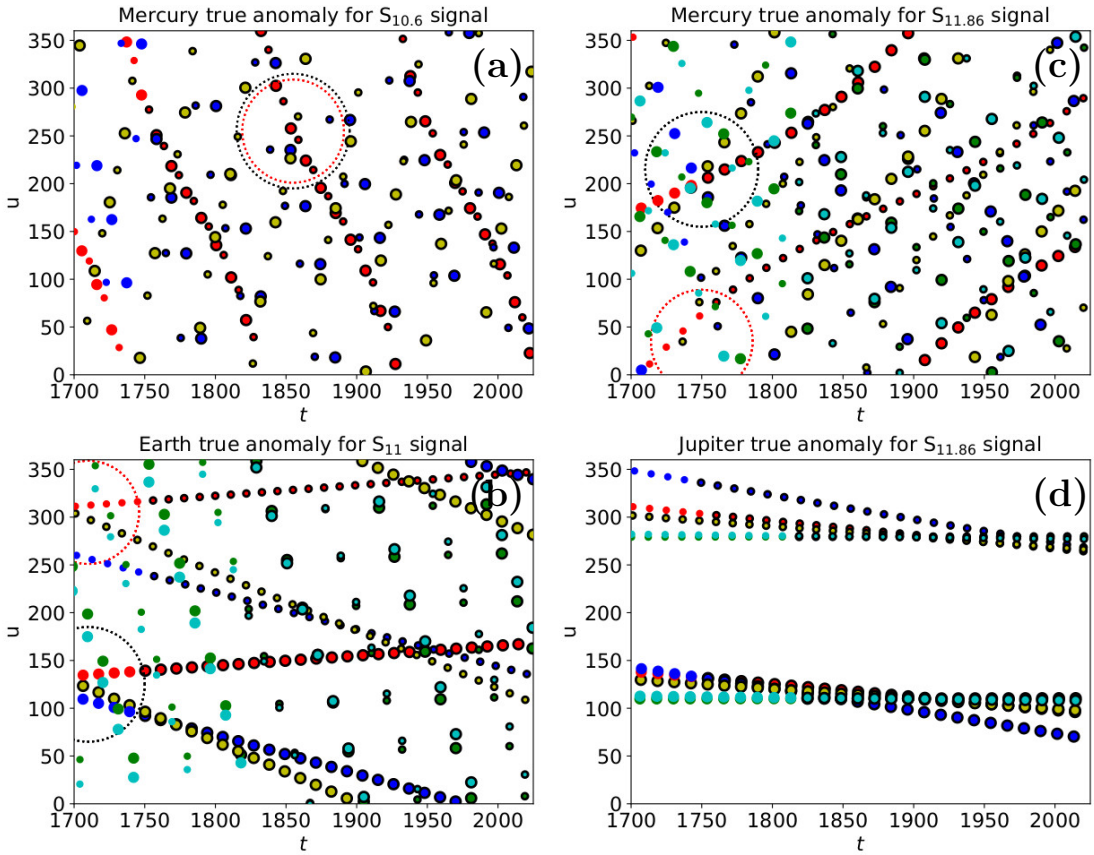


Figure 14. (a) Mercury's true anomalies for signal $S_{10.6}$. (b) Earth's true anomalies for signal S_{11} . (c) Mercury's true anomalies for signal $S_{11.86}$. (d) Jupiter's true anomalies for signal $S_{11.86}$. Otherwise as in Figure 13.

anomaly migration directions of the signals detected in three different samples (Figure 14a). The mean anomaly migration values $\Delta M/360^\circ = -2.8, -5.9$ and 7.8 reveal that the red and the blue circles migrate downwards, and the yellow circles migrate upwards (Table 10, Signal $S_{10.6}$). The large and small circles of each sample show the overlapping effect, because this signal is an even number multiple $44 \times P_{\text{Mercury}}$. The red and yellow circles of the symmetric pure sine model for samples Rmonthly and Ryearly follow this regularity. However, the blue small circles for the asymmetric double wave model of sample Rmonthly break this regularity. Using all the above-mentioned information, we identify the convergence points of both ν_{\min} and ν_{\max} true anomalies at $t_C = 1855$ years and $\nu \approx M_C = 255$ degrees (Figure 14a: centre of blue and red dotted lines). Due to the strong migration, the same pattern is repeated at the approximate year and degree coordinates (1760,220) and (1940,280).

The rounds values $\mathcal{P} = 43.891 \pm 0.083$ and 44.26 ± 0.13 differ only $\Delta \mathcal{P}_{\text{rel}} = 1.3$ and 2.0 from $44 \times P_{\text{Mercury}}$ (Table 10: Signal $S_{10.6}$). The $\mathcal{P} = 43.774 \pm 0.0824$ value for sample Rmonthly double wave model has a large $\Delta \mathcal{P}_{\text{rel}} = 9.0$ relative rounds deviation. However, all three relative mean anomaly migration ΔM_{rel} values $0.0025, 0.0052$ and 0.0059 are nearly the same.

7.6. Signal $S_{11y} \cong 11 \times P_{\text{Earth}}$

This strongest S_{11y} signal is close to $11 \times P_{\text{Earth}}$. The non-weighted DCM analysis gives the rounds values $\mathcal{P} = 11.0033 \pm 0.0064$, 10.9878 ± 0.0051 and 10.981 ± 0.021 (Table 10: **Rmonthly**, **Ryearly**). The respective relative rounds deviation $\Delta\mathcal{P}_{\text{rel}} = 0.52$, 0.24 and 0.95 values support the $11 \times P_{\text{Earth}}$ relation. The rounds values $\mathcal{P} = 10.8585 \pm 0.0048$ and 10.863 ± 0.022 obtained from the weighted DCM analysis, however, show large $\Delta\mathcal{P}_{\text{rel}} = 29$ and 6.2 relative rounds deviations (Table 10: **Cmonthly**, **Cyearly**).

The uneven $11 \times P_{\text{Earth}}$ multiple causes the 180 degrees separation effect of the ν_{\min} and ν_{\max} true anomalies. Regardless of the above-mentioned large $\Delta\mathcal{P}_{\text{rel}}$ values for samples **Cmonthly** and **Cyearly**, we obtain very convincing estimates for the convergence points of the true anomaly ν_{\min} and ν_{\max} migration curves (Figure 14b). The maxima converge at $t_C = 1710$ years and $\nu \approx M_C = 125$ degrees. Only the highlighted yellow circles of **Ryearly** reach this convergence point, because it is *outside* samples **Rmonthly**, **Cmonthly** and **Cyearly**. Yet, the large “predictive” red, blue, green and cyan circles migrate through the large dotted blue circle surrounding this convergence point (Figure 14b). The small circles show that the minima ν_{\min} converge at $t_C = 1710$ and $\nu \approx M_C = 305$ degrees. The small blue circles denoting the asymmetric **Rmonthly** double wave model, represents the only migration curve that deviates from this convergence point. Both convergence points in the year 1710 are located about 50 years before the beginning of **Rmonthly** and **Cmonthly** samples (the highlighted red and blue circles) and about 100 years before the beginning of **Cmonthly** and **Cyearly** samples (the highlighted green and cyan circles). The successful convergence of the “predictive” red, blue, green and cyan circles (not highlighted with black circles) indicates that all five detected S_{11y} signals can represent one and the same real signal.

7.7. Signal $S_{11,y86}$

The $S_{11,y86}$ signal period is close to $49.0 \times P_{\text{Mercury}}$ and $1.0 \times P_{\text{Jupiter}}$. The known period ratio is $P_{\text{Jupiter}}/P_{\text{Mercury}} = 49.2608$. This pair of $S_{11,y86}$ signal multiples displays the most dramatic statistical $|\Delta\mathcal{P}|$ fluctuation effect (Equations 39 and 43). The messy Mercury’s migration curves (Figure 14c) have exceptionally regular Jupiter’s migration curve counterparts (Figure 14d).

7.7.1. Signal $S_{11,y86} \cong 49.0 \times P_{\text{Mercury}}$

None of the five \mathcal{P} rounds values differs more than $3\Delta\mathcal{P}_{\text{rel}}$ from $49.0 \times P_{\text{Mercury}}$ (Table 10: Signal $S_{11,y86}$). No other planetary signal candidate shows this degree of regularity. All relative mean anomaly migration values fulfil $\Delta M_{\text{rel}} \leq 0.0054$. For this particular ΔM_{rel} parameter, this is also the best result among all planetary signal candidates. Even the largest mean anomaly migration $\Delta M/360^\circ$ is only 4.6 revolutions during 850 revolutions of Mercury. The smallest mean anomaly migration for sample **Rmonthly** ($K_2 = 1$) is only $\Delta M/360^\circ = 0.65$ during 1137 revolutions. The twisted large and small red circle curves of this sample nicely illustrate Mercury’s orbit eccentricity effect (Figure 14c).

The uneven $49 \times P_{\text{Mercury}}$ multiple causes the 180 degrees separation effect of ν_{\min} and ν_{\max} values (Figure 14c). The red, green, yellow and cyan circles of four samples show positive upwards migration. The blue circles denoting the double wave model results for sample **Rmonthly** show the only negative downwards migration. The curves of the large highlighted red and yellow circles denoting the ν_{\max} values *inside* samples **Rmonthly** ($K_2 = 1$) and **Ryearly** intersect at the convergence point $t_C = 1750$ and $\nu \approx M_C = 215$ degrees. The respective large “predictive” blue, green and cyan circle curves, which are *outside* samples **Rmonthly** ($K_2 = 2$), **Cmonthly** and

Cyearly, also intersect at the centre of the large blue dotted circle surrounding this convergence point. The respective ν_{\min} convergence point is at $t_C = 1750$ and $\nu \approx M_C = 35$ degrees. The two detected convergence points indicate that all five $S_{11,y86}$ signals detected in different samples can represent one and the same signal.

7.7.2. Signal $S_{11,y86} \cong 1.0 \times P_{\text{Jupiter}}$

Three rounds $\mathcal{P} = 1.0001 \pm 0.0018$, 0.9964 ± 0.0023 and 0.9995 ± 0.0057 values support the $1 \times P_{\text{Jupiter}}$ relation (Table 10: Signal $S_{11,y86}$). Two rounds values for Rmonthly, $\mathcal{P} = 0.9953 \pm 0.0010$ and 0.99224 ± 0.00093 , differ $\Delta\mathcal{P}_{\text{rel}} = 4.7$ and 8.3 from this relation. However, all mean anomaly migration values fulfil $|\Delta M| \leq 0.18$ revolutions.

The uneven $1 \times P_{\text{Jupiter}}$ multiple causes the 180 degree separation effect between Jupiter's true anomaly ν_{\min} and ν_{\max} values (Figure 14b). All true anomaly migration curves are so regular that there is no need to search for convergence points. The small blue circles, which denote the ν_{\min} values of the asymmetric double wave model for sample Rmonthly, show the largest deviation from the general migration trends. The regular convergence of Jupiter's true anomalies definitely indicates that one and the same signal is detected in all five different samples. The strongest amplification of the $S_{11,y86}$ sunspot signal occurs close to true anomaly $\nu = \nu_{\max} = 120^\circ$. The damping of this signal occurs about 6 years ($11.86/2$) later, close to true anomaly $\nu = \nu_{\min} = 300^\circ$.

The detection of the convergence points for the signal candidates of Mercury and Jupiter indicates that the relative motions of these two planets can cause this $S_{11,y86}$ signal.

The maxima of all five $S_{11,y86}$ signals in Table 10 occur between Jupiter's perihelion and aphelion, which are denoted with dotted and continuous vertical lines in Figure 15. All $S_{11,y86}$ signal minima are between Jupiter's aphelion and perihelion. The phases of all five $S_{11,y86}$ signals are stable, and stay in phase with Jupiter's orbital motion. The signal amplitudes in the monthly and the yearly samples are nearly the same. This $S_{11,y86}$ signal is clearly connected to the orbital motion of Jupiter. The distance between the Sun and Jupiter modulates the number of sunspots.

All these results confirm an irrefutable deterministic connection between the sunspot cycle and Jupiter's orbital motion. If these results do not represent the *direct* detection of Jupiter from the sunspot data, then, what have we detected? It would be quite a coincidence if we had managed to formulate a flawed statistical method that would accidentally detect Jupiter's period from the sunspot data. We can ask, quite rightly, has anyone else ever made this kind of a direct detection of Jupiter from the sunspot data?

7.8. Signal $S_{53y} \cong 4.5 P_{\text{Jupiter}}$

The two rounds $\mathcal{P} = 4.439 \pm 0.023$ and 4.538 ± 0.064 differ only $\Delta\mathcal{P}_{\text{rel}} = 2.6$ and 0.59 from $4.5 \times P_{\text{Jupiter}}$ (Table 10: S_{53y}). We merely mention this regularity, but we do not search for converge points from the migration of only two curves.

7.9. Signal $S_{66y} \cong 5.5 \times P_{\text{Jupiter}}$ or $\cong 6.0 \times P_{\text{Jupiter}}$

This weakest one of all detected signals has a rounds value $\mathcal{P} = 5.62 \pm 0.12$ (Table 10: Signal S_{66y}). We mention this S_{66y} signal because the double sinusoid signal period $P = 143.30 \pm 0.99$ (Table 9: Signal S_{66y}) has a rounds value $\mathcal{P} = 12.088 \pm 0.083$, which is close to $2 \times 6 \times P_{\text{Jupiter}}$.

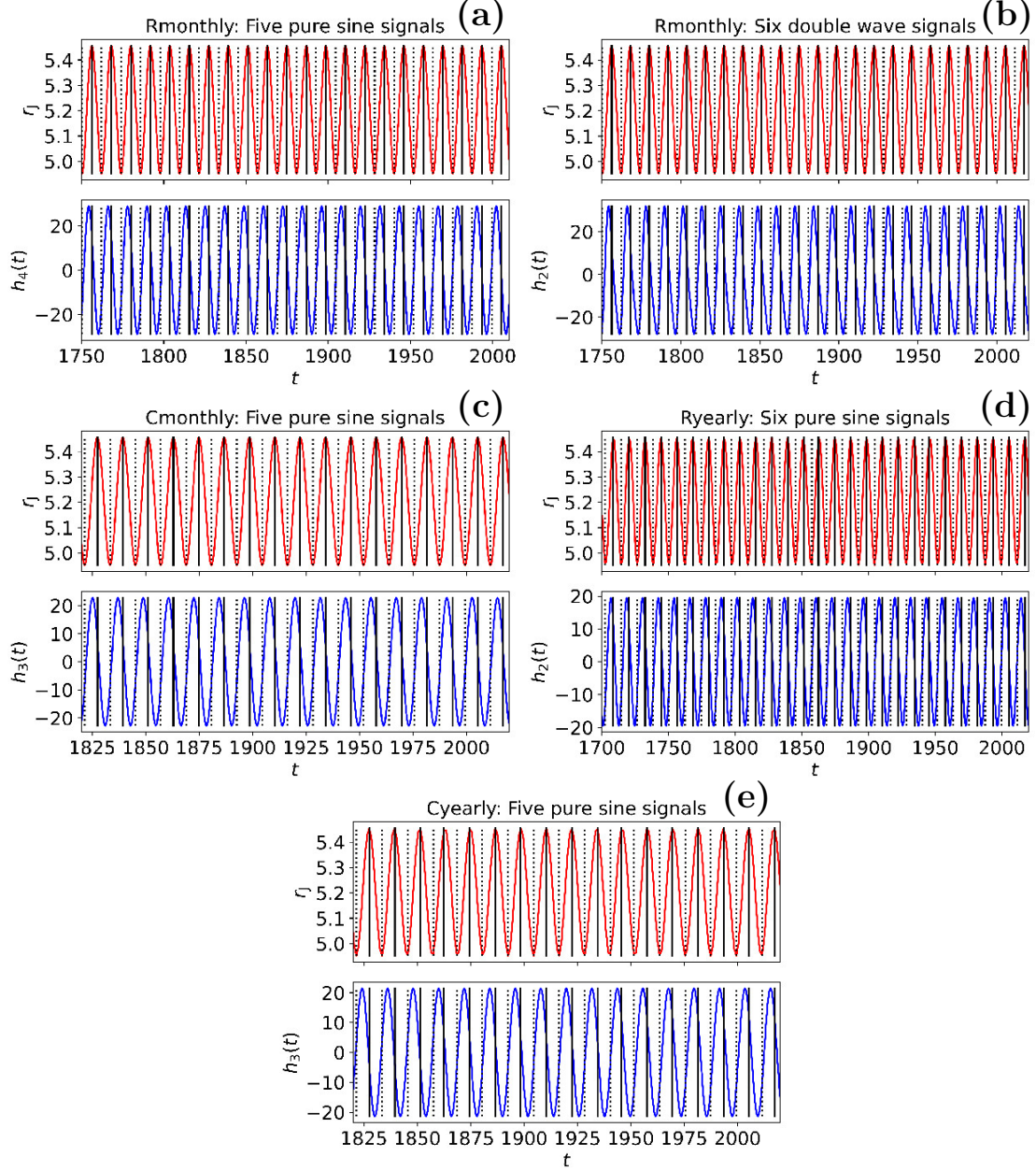


Figure 15. Signal S_{11.y86} connection to Jupiter's distance r_J from the Sun. (a) Upper panel: Red curve shows distance between the Sun and Jupiter. Aphelion and perihelion epochs are denoted with vertical black continuous and dotted lines, respectively. Units are x-axis $[t]$ = years and y-axis $[r_J]$ = AU. Lower panel: Blue curve shows simultaneous $h_4(t)$ pure sine 11.807 year signal in Rmonthly (Table 18). Aphelion and perihelion notations are as in upper panel. Units are x-axis $[t]$ = years and y-axis $[h_4(t)]$ = dimensionless. (b) $h_2(t)$ double wave 11.770 year signal in Rmonthly (Table 20). Otherwise as in “a”. (c) $h_3(t)$ pure sine 11.863 year signal in Cmonthly (Table 22). Otherwise as in “a”. (d) $h_2(t)$ pure sine 11.820 year signal in Ryearly (Table 26). Otherwise as in “a”. (e) $h_3(t)$ pure sine 11.856 year signal in Cyearly (Table 28). Otherwise as in “a”.

Table 11. Synodic period connections. (1) P_1 period. (2-5) P_2 period. Next lines: P_{\pm} periods for P_1 and P_2 combinations (Equation 47). Signals S_{10y} and S_{11y} connect to signal S_{110y} . Signals $S_{11,y86}$ and S_{110y} connect to signal $S_{10,y6}$. Signal $S_{10,y6}$ has no direct connection to signals S_{10y} or S_{11y} .

(1)	(2)	(3)	(4)	(5)
	$P_2 = S_{10,y6}$	$P_2 = S_{11y}$	$P_2 = S_{11,y86}$	$P_2 = S_{110y}$
$P_1 = S_{10y}$	$P_- = 177$ $P_+ = 5.15$	$P_- = 110$ $P_+ = 5.24$	$P_- = 63.8$ $P_+ = 5.42$	$P_- = 11.0$ $P_+ = 9.17$
$P_1 = S_{10,y6}$		$P_- = 292$ $P_+ = 5.40$	$P_- = 99.8$ $P_+ = 5.60$	$P_- = 11.7$ $P_+ = 9.67$
$P_1 = S_{11y}$			$P_- = 152$ $P_+ = 5.71$	$P_- = 12.2$ $P_+ = 10.0$
$P_1 = S_{11,y86}$				$P_- = 13.3$ $P_+ = 10.7$

7.10. Signal S_{110y}

In the order of decreasing amplitude, the five strongest signals detected from the sunspot data are the S_{11y} , S_{10y} , $S_{11,y86}$, S_{110y} and $S_{10,y6}$ signals (Table 6). The fourth strongest, and the longest period, the S_{110y} signal can not be connected to any particular planet. There are, however, clear connections between the five strongest signals. These ± 1 round synodic period difference connections

$$P_{\pm} = [P_1^{-1} \pm P_2^{-1}]^{-1} \quad (47)$$

are given in Table 11. These five strongest signals can, and inevitably do, interact through these one round differences. This means that the interference of these five signals is repeated indefinitely, as long as the orbital periods of the involved planet candidates remain constant. This is one additional proof of that these five strongest S_{11y} , S_{10y} , $S_{11,y86}$, S_{110y} and $S_{10,y6}$ signals can cause a common phenomenon: the sunspot cycle.

For example, the $n = 3287$ observations in sample R_{monthly} have $m = 81.6$ and $s = 67.7$. Only twenty observations y_i have values larger than $m + 3s = 285$. The best model for this sample, the sum of five pure sine signals, has $M_0 = 81.3 \pm 0.8$ (Figure 4a). The sum of the peak to peak amplitudes for these five strongest S_{11y} , S_{10y} , $S_{11,y86}$, S_{110y} and $S_{10,y6}$ signals is $A_1 + A_2 + A_3 + A_4 + A_5 = 331$ (Table 6: column 2). These five signals alone are strong enough to reproduce the whole range of observed y_i changes. No additional signals are needed.

We conclude that the signal identifications presented in this Section 7 confirm that the planet identification criterion C4 is certainly fulfilled.

8. Discrete Fourier Transform (DFT) cross-check

Zhu and Jia (2018) applied the Discrete Fourier Transform (DFT) to the daily sunspot number data from WDC SILSO (Royal Observatory of Belgium, Brussels). They used the DFT version formulated by Horne and Baliunas (1986). DFT searches for the best pure sine model for the data. Here, we cross-check if a similar DFT analysis of our monthly sunspot number sample R_{monthly} gives the same results as our pure sine model DCM analysis (Table 18).

Table 12. Independent frequency limitation (Equation 50). Ratios $f/f_0 = \Delta T/P$ in order of decreasing sample time interval ΔT . Arrows above numerical values indicate cases where $\Delta f < f_0$.

Sample	ΔT (y)	S_{10y} $\Delta T/P$ (-)	$S_{10,y6}$ $\Delta T/P$ (-)	S_{11y} $\Delta T/P$ (-)	$S_{11,y86}$ $\Delta T/P$ (-)
Ryearly	321.0	32.10	30.28	29.18	27.07
Ryearly2000	299.0	29.90	28.21	27.18	25.21
Rmonthly	273.8	27.38	25.83	24.89	23.09
Rmonthly2000	250.9	25.09	23.67	22.81	21.16
Cmonthly	204.8	20.48	19.32	18.62	17.27
Cyearly	203.0	20.30	19.15	18.45	17.12
Cmonthly2000	181.9	18.19	17.16	16.54	15.34
Cyearly2000	181.0	18.10	17.07	16.45	15.25

8.1. DFT detection of two pure sine signals

Before our DFT cross-check of DCM analysis, we perform some simple simulations. In these simulations, we compare the performance of DFT and DCM. Let us assume that the data contains the sum signal $s(t) = s_1(t) + s_2(t)$ of two pure sine signals

$$s_1(t) = a_1 \sin(2\pi f_1 t) \quad (48)$$

$$s_2(t) = a_2 \sin(2\pi f_2 t), \quad (49)$$

where the frequencies fulfil $f_1 \approx f_2$. DFT can detect both of the $s_1(t)$ and $s_2(t)$ signals, if

$$\Delta f = |f_2 - f_1| \gtrsim f_0, \quad (50)$$

where $f_0 = 1/\Delta T$ is the distance between independent frequencies (Loumos and Deeming, 1978). We give the $f/f_0 = \Delta T/P$ ratios for the S_{11y} , S_{10y} , $S_{10,y6}$ and $S_{11,y86}$ signals in Table 12. The S_{10y} and $S_{10,y6}$ signal frequencies fulfil the criterion of Equation 50 only in the two longest Ryearly and Ryearly2000 samples. This criterion is not fulfilled in our DFT cross-check Rmonthly sample (Table 12). Furthermore, many pairs of S_{11y} , S_{10y} , $S_{10,y6}$ and $S_{11,y86}$ signals detected in this sample Rmonthly have frequency differences Δf close to $1 \times f_0$.

The interference pattern of the sum $s(t)$ of the two signals $s_1(t)$ and $s_2(t)$ is repeated during the beat period $P_{\text{beat}} = |P_1^{-1} - P_2^{-1}|^{-1} = |f_1 - f_2|^{-1}$. The solutions for the frequency, the amplitude and the phase of this sum signal $s(t)$ are quite complex (Feth, 1974; Aguilar et al., 2012; Rutkowski, 2014; Schwär, Müller, and Schlecht, 2023). For the purposes of our DFT cross-check, it suffices to discuss the frequency $f(t)$ and the phase ϕ changes of the sum signal $s(t)$.

The frequency $f(t)$ of the $s(t)$ sum signal is constant

$$f(t) = (f_1 + f_2)/2, \text{ if } a_1 = a_2. \quad (51)$$

This frequency $f(t)$ varies between the lower and upper limits given below

$$f_2 - \frac{a_1(f_1 - f_2)}{a_2 + a_1} \leq f(t) \leq f_2 + \frac{a_1(f_1 - f_2)}{a_2 + a_1}, \text{ if } a_2 > a_1. \quad (52)$$

In this case, the $f(t)$ frequency changes are dominated by the stronger f_2 signal.

The sum signal $s(t)$ amplitude a_s is constantly changing. An abrupt instantaneous phase shift

$$\Delta\phi = [\text{arc sin}(a_1/a_2)]/\pi \quad (53)$$

occurs at the epoch of a_s minimum. This shift is the largest, $\Delta\phi = 0.5$, for equal amplitudes $a_1 = a_2$.

The limitation of Equation 50 can *prevent* the DFT detection of both f_1 and f_2 values. The effects of Equations 51, 52 and 53 can *mislead* the DFT detection of the correct f_1 and f_2 values.

The units of time intervals and periods in all our simulations are years. The amplitude unit is dimensionless. These units are therefore no longer mentioned in the simulations below. We simulate y_i^* data, where the monthly sunspot number time points t_i^* are computed for four alternative time intervals of $\Delta T = 70, 90, 110$ and 274 . These time intervals begin from the year 1749 at the beginning of sample **Rmonthly**. The longest $\Delta T = 274$ simulation has the same time span and the same time points as **Rmonthly**. The $s_1(t_i^*)$ and $s_2(t_i^*)$ signal periods are $P_1 = 1/f_1 = 10$, $P_2 = 1/f_2 = 11$. They are equal to the periods of the two strongest S_{10^y} and S_{11^y} signals detected in sample **Rmonthly**. This gives the beat period $P_{\text{beat}} = 110$. We simulate data for two alternative amplitude combinations $a_1 = a_2 = 50 \Rightarrow f(t) = \text{constant}$ (Equation 51) and $a_1 = 25 < a_2 = 50 \Rightarrow f(t) = \text{variable}$ (Equation 52). Hence, the total number of simulated samples is $4 \times 2 = 8$. The tested period interval between 5 and 200 years is the same as in our earlier DCM analysis of **Rmonthly** sample.

For the **Rmonthly** sample, the DCM five pure sine signal $\mathcal{M}=5$ model gives the residuals ϵ_i , which have a standard deviation $s_\epsilon = 42$. We assume that after the detection of these five pure sine signals, these remaining ϵ_i residuals represent the noise in the original data. Therefore, the errors σ_i^* for the simulated data are drawn from a Gaussian distribution having a mean $m = 0$ and a standard deviation $s = s_\epsilon = 42$. The simulated data are

$$y_i^* = m^* + s_1(t_i^*) + s_2(t_i^*) + \sigma_i^*, \quad (54)$$

where $m^* = 81.6$ is the mean of all y_i values in **Rmonthly**. The selected m^* value has no impact on our results, because it is subtracted from the simulated y_i^* data before the computation of DFT periodogram. The DCM two sine wave model $\mathcal{M}_{2,1,0,R}$ solves this $M_0 = m^*$ value.

We analyse the $2 \times 4 = 8$ simulated data samples using the same DFT approach as Zhu and Jia (2018). They used the pre-whitening technique, where DFT detects one signal at the time (Scargle, 1982; Reegen, 2007). We apply DFT to the original simulated data. This gives us the first P_1 period. The least squares fit is then made to the original simulated data, where the pure sine model has the P_1 period. This “first DFT model” gives the first sample of residuals. DFT is applied to this first sample of residuals, which gives the second P_2 period. The next least squares fit is made to the first sample of residuals using a pure sine model having a period P_2 . The model for this sample is called “the second DFT model”. This gives the second sample of residuals.

The DFT pre-whitening technique has its limitations. The DFT *can only* be used to cross-check the DCM pure sine model analysis results for non-weighted data. DFT *can not* be used to cross-check the DCM double wave model analysis results, nor the DCM weighted data analysis results.

In the next Sections 8.2 and 8.3, we perform the DCM and DFT analyses of the $2 \times 4 = 8$ simulated data samples, and compare the results. The results for each individual simulated sample are presented in one vertical column of Figures 16 and 17, where the dashed vertical lines intersecting the periodograms denote the *simulated frequencies* $1/P_1 = 1/10$ and $1/P_2 = 1/11$. The diamonds at the DFT periodogram maxima and the DCM periodogram minima denote the *detected frequencies*. Hence, the vertical dashed lines intersect the diamonds only if the method detects the correct frequencies.

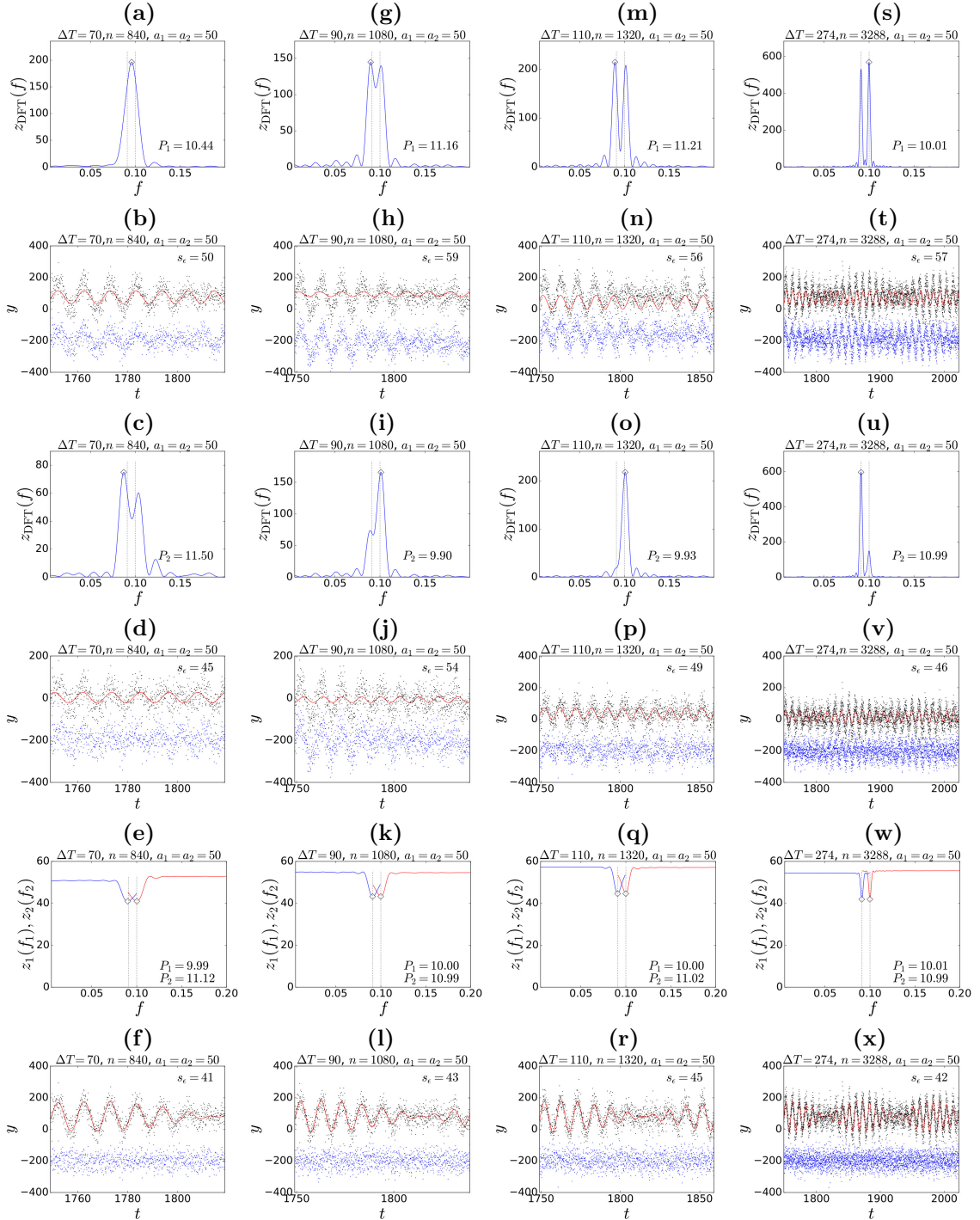


Figure 16. Equal amplitude $a_1 = a_2 = 50$ simulations for signal periods $P_1 = 10$ and $P_2 = 11$ (Equations 48 and 49). (a) DFT periodogram $z_{\text{DFT}}(f)$. Period $P_1 = 10.44$ is detected from y_i^* data simulated with $n = 840$, $\Delta T = 70$, $P_1 = 10$, $a_1 = 50$, $P_2 = 11$ and $a_2 = 50$. Units are $[f] = 1/y$ and $[z_{\text{DFT}}] = \text{dimensionless}$. Vertical dashed black lines denote locations of simulated frequencies $f_1 = 1/P_1$ and $f_2 = 1/P_2$. Diamond denotes location of detected frequency. (b) Model for simulated data. Black dots denote simulated y_i^* data. Red curve denotes pure sine model having period $P_1 = 10.44$. Black dots denote ϵ_i residuals offset to level -200. Standard deviation of residuals is $s_\epsilon = 50$. Units are $[t] = \text{year}$ and $[y] = [\epsilon] = \text{dimensionless}$. (c-d) DFT results for first sample of residuals. Otherwise as in a-b. (e) DCM periodograms $z_1(f_1)$ and $z_2(f_2)$. Periods $P_1 = 9.99$ and $P_2 = 11.12$ are detected from y_i^* data simulated with $n = 840$, $\Delta T = 70$, $P_1 = 10$, $a_1 = 50$, $P_2 = 11$ and $a_2 = 50$. Diamonds denote locations of detected frequencies. Units are $[f] = 1/y$ and $[z_1] = [z_2] = \text{dimensionless}$. (f) Model for simulated data. Black dots denote simulated y_i^* data. Red curve shows two pure sine signal DCM model. Blue dots denote ϵ_i residuals offset to level -200. Standard deviation of residuals is $s_\epsilon = 41$. Units are $[t] = \text{year}$ and $[y] = [\epsilon] = \text{dimensionless}$. (g-l) Data simulated for longer time interval $\Delta T = 90$. Otherwise as in a-f. (m-r) Data simulated for longer time interval $\Delta T = 110$. Otherwise as in a-f. (s-x) Data simulated for longer time interval $\Delta T = 274$. Otherwise as in a-f.

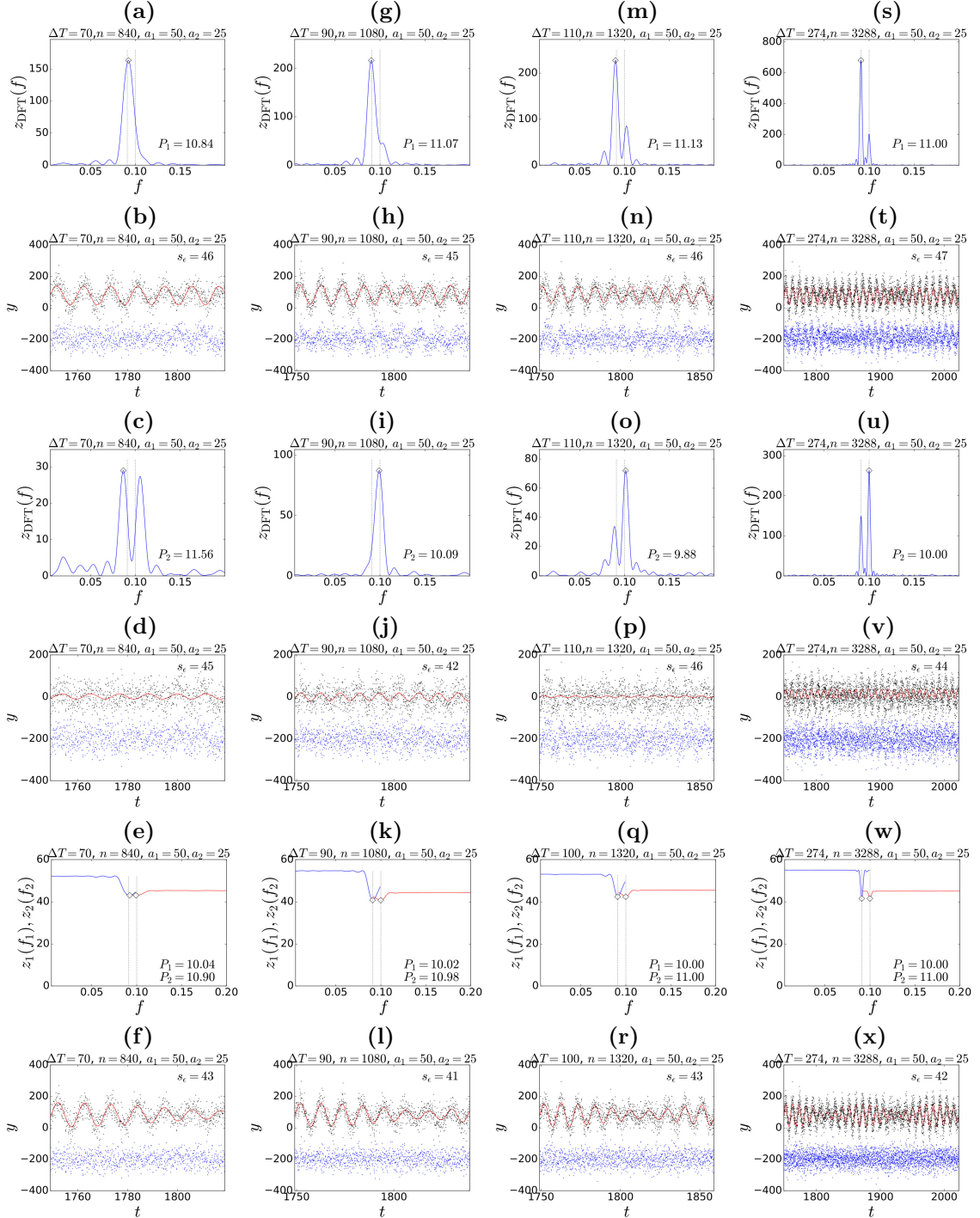


Figure 17. Unequal amplitude $a_1 = 25$ and $a_2 = 50$ simulations for signal periods $P_1 = 10$ and $P_2 = 11$ (Equations 48 and 49). Otherwise as in Figure 16.

8.2. Results for two equal amplitude signals

We present the results for equal amplitudes $a_1 = a_2 = 50$ in Figure 16.

The results for the shortest simulated time interval, $\Delta T = 70$, are shown in Figures 16a-16f. The DFT periodogram $z_{\text{DFT}}(f)$ shows only one peak at $P_1 = 10.44$ (Figure 16a). The limitation of Equation 50 prevents the detection of two peaks. The effect $[(f_1 + f_2)/2]^{-1} = 10.48$ (Equation 51) explains the detected wrong period $P_1 = 10.44$ value. The first DFT model residuals have a standard deviation $s_\epsilon = 50$, and show regular periodic variation (Figure 16b). The DFT periodogram for these residuals shows the highest peak at $P_2 = 11.50$ (Figure 16c). The second DFT model residuals have a standard deviation of $s_\epsilon = 45$ and show some regular periodic variation (Figure 16d). DCM detects the $P_1 = 9.99$ and $P_2 = 11.12$ periods, which are close to, but not exactly equal to the simulated 10 and 11 values (Figure 16e). The DCM model residuals show no periodic variation and follow a straight line (Figure 16f). This residual distribution resembles a random distribution. The DCM model residuals $s_\epsilon = 41$ standard deviation is much smaller than the DFT model residuals $s_\epsilon = 45$ standard deviation. In this $\Delta T = 70$ simulation, DFT fails and DCM succeeds.

Both DFT periodograms are double-peaked in the longer $\Delta T = 90$ simulation (Figures 16g and 16i). DFT detects the $P_1 = 11.16$ and $P_2 = 9.90$ periods, which are closer to the simulated values. The residuals of both DFT models show periodic variability (Figures 16h and 16j). The mean residual $s_\epsilon = 59$ and 54 values are larger than in the earlier shorter $\Delta T = 70$ simulation, because there is a $\Delta\phi = 0.5$ phase shift (Equation 53) in the simulated y_i^* data at the year 1804. DCM detects the correct $P_1 = 10.00$ and $P_2 = 10.99$ periods (Figure 16k). The distribution of DCM model residuals resembles that of a random distribution, and there is no periodic variability (Figure 16l). The $s_\epsilon = 43$ value of DCM model is much smaller than the $s_\epsilon = 54$ value of DFT model, because the DCM can handle the $\Delta\phi = 0.5$ phase shift (Equation 53). Again, DCM performs better than DFT.

In the next $\Delta T = 110$ simulation, the criterion of Equation 50 is fulfilled, and therefore the first DFT periodogram is clearly double-peaked (Figure 16m). DFT detects the $P_1 = 11.21$ and $P_2 = 9.93$ periods, which differ from the simulated periods. Both DFT model $s_\epsilon = 56$ and 49 mean residual values are large (Figures 16n and 16p). These DFT residuals show periodic variability. DCM detects the correct $P_1 = 10.00$ and $P_2 = 11.02$ periods (Figure 16q). The distribution of DCM model residuals appears random, and its standard deviation is $s_\epsilon = 45$ (Figure 16r). The abrupt phase shift in the simulated y_i^* data (Equation 53) at the year 1804 misleads DFT, but it does not mislead DCM.

Two abrupt phase shifts, in the years 1804 and 1914, occur in the last $\Delta T = 274$ simulation (Equation 53). Finally, DFT succeeds in finding the correct $P_1 = 10.01$ and $P_2 = 10.99$ periods (Figures 16s and 16u). However, the residuals of both DFT models still show periodic variability (Figures 16t and 16v). DCM detects the correct $P_1 = 10.01$ and $P_2 = 10.99$ periods (Figures 16w). The DCM model residuals show no periodic variability, and their distribution resembles a random distribution (Figures 16x). The standard deviation $s_\epsilon = 46$ of the DFT model clearly exceeds the $s_\epsilon = 42$ value of DCM model. In short, DCM performs better than DFT.

8.3. Results for two unequal amplitude signals

We present the results for unequal amplitudes $a_1 = 25$ and $a_2 = 50$ in Figure 17.

All details are not discussed, as in the case of Figure 16. We concentrate only on the general results in Figure 17, because they are the same for all $\Delta T = 70, 90, 110$ and 274 simulations.

If the relation of Equation 50 is not fulfilled, DFT can not detect the correct period values, but DCM can. If this relation is fulfilled, DFT can also succeed.

The relation of Equation 52 predicts that the frequency $f_2 = 1/P_2 = 1/11$ of the stronger signal dominates in the frequency $f(t)$ of the $s(t)$. Therefore, DFT always detects this $P_2 = 11$ period signal first. DCM detects both signals simultaneously, neither one of them being “the first”.

DFT can not model the amplitude changes or the abrupt phase shifts (Equation 53). For this reason, the DFT model residuals always show periodic variability, while the DCM model residuals do not. DCM residuals have a random distribution concentrated on a straight line, which is a signature of a good model. DFT model s_ϵ values are always larger than DCM model s_ϵ values. This means that some information is always lost at every DFT pre-whitening stage, where one pure sine signal is detected at the time. Both methods reach s_ϵ levels that are close to the standard deviation $s = 42$ of the random errors σ_i^* , which are added as noise to the simulated data (Equation 54). This means that both methods can also detect the second, weaker $P_1 = 10$ signal, which has the peak to peak amplitude $A_1 = 2a_1 = 50$ that has the same order of magnitude as $s = 42$. However, only DCM can reach this $\sigma_\epsilon \approx s = 42$ level for all $2 \times 4 = 8$ simulations.

8.4. Discrete Fourier Transform (DFT) analysis of `Rmonthly`

We simulate data arising from the interference between two sine waves having frequencies $f_1 \approx f_2$ (Equation 54). Our DFT and DCM analyses of these simulated data reveal the performance differences between these two methods. We encounter the same five DFT drawbacks for equal and unequal amplitude sine waves (Sections 8.2 and 8.3).

1. Detection of close frequencies: DFT suffers from the limitation of Equation 50, but DCM does not.
2. Wrong frequency detection: DFT suffers from the misleading effects of Equations 51 and 52, but DCM does not.
3. Abrupt phase shifts: DFT can not model the abrupt phase shifts of Equation 53, but DCM can.
4. Biased residuals: DFT pre-whitening model residuals do not have a random distribution, but DCM model residuals do. The mean residual s_ϵ values of DFT models are always larger than those of DCM models, which means that some information is lost at every DFT pre-whitening stage.
5. Detection accuracy: The difference between the detected and the simulated period values is larger for DFT than for DCM. This difference decreases as the samples become longer. For real data, this means that DCM detects the correct period values more probably than DFT.

When DFT analysis fails, DCM analysis can succeed. We can safely state that DCM performs better than DFT. The two strongest S_{11y} and S_{10y} signals in the real data sample `Rmonthly` are exactly the same as in our simulations. When we use DFT pre-whitening to search for more than two signals in this real data sample `Rmonthly`, it is logical to assume that the above DFT drawbacks become more pronounced.

The DFT pre-whitening results for the sample `Rmonthly` are shown in Figure 18. The first five S_{11y} , S_{10y} , $S_{11,y86}$, S_{110y} and $S_{10,y6}$ signals detected using DFT pre-whitening (Figure 18 a-j) are the same as those detected using the five pure sine signal DCM model (Table 18: $M=5$). The only minor difference is that DCM detects signal $S_{10,y6}$ before signal S_{110y} . Both methods give nearly the same amplitudes for these five strongest signals. The sixth-strongest detected signals are different: the S_{53y} signal for DCM (Table 18: $M=7$) and the $S_{8,y4}$ signal for DFT (Figure 18 k-l). The seventh-strongest detected signals are also different, the S_{8y} signal for DCM and the S_{53y} signal for DFT. DCM detects only seven signals from sample `Rmonthly`, because the unstable $M=8$ model is rejected (Table 18: “UM”). DCM analysis of predictive data sample

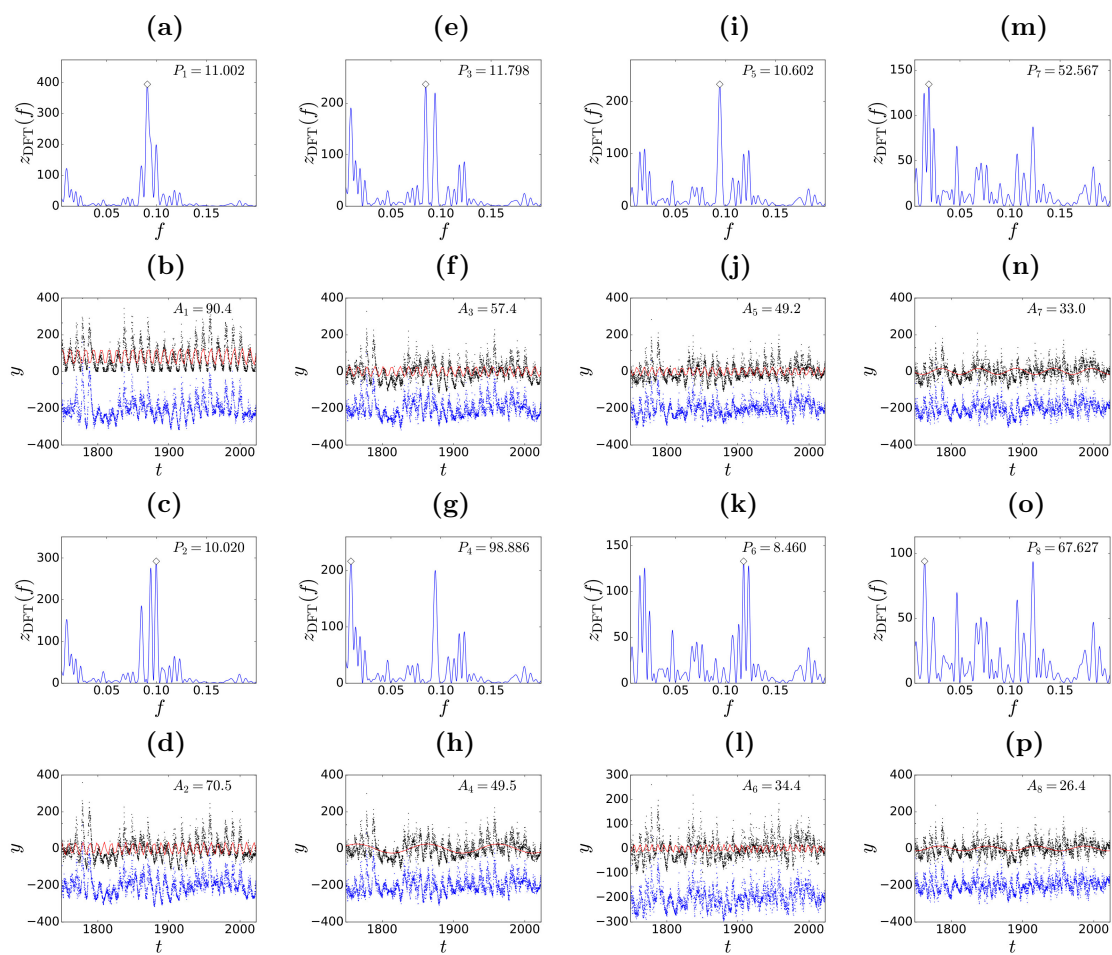


Figure 18. DFT pre-whitening analysis results for **Rmonthly** sample. (a) DFT periodogram for original data. Diamond denotes peak of periodogram at frequency of best period $P_1 = 11.002$ years. Units are $[f] = 1/y$ and $[z_{\text{DFT}}] = \text{dimensionless}$. (b) Pure sine model for original data. Black dots denote original y_i data. Red curve denotes sine model with period $P_1 = 11.002$. Its peak to peak amplitude is $A_1 = 90.4$. Blue dots denote residuals ϵ_i offset to level -200. Units are $[t] = \text{years}$ and $[y] = [\epsilon] = [A] = \text{dimensionless}$. (c-d) Second signal detected from first sample of residuals. (e-f) Third signal detected from second sample of residuals. (g-h) Fourth signal detected from next sample of residuals. (i-j) Fifth signal. (k-l) Sixth signal. (m-n) Seventh signal. (o-p) Eighth signal. Notations for all panel pairs from “c-d” to “o-p” are same as in panel pair “a-b”.

Rmonthly2000, which is a subsample of all data sample **Rmonthly**, indicates that the correct number of real signals is six (Section 6: Figure 7). We conclude that DCM and DFT detect the same five strongest signals from sample **Rmonthly**. We have already shown that these five strongest signals are clearly connected to each other (Table 11).

It is essential to understand, why the DFT pre-whitening analysis of **Rmonthly** sample does succeed, regardless of all DFT drawbacks discussed above? The limitation of Equation 50 is encountered, because the difference between the $S_{10,y6}$ and $S_{11,y}$ signal frequencies is smaller than f_0 (Table 12). All four $S_{10,y}$, $S_{10,y6}$, $S_{11,y}$ and $S_{11,y86}$ signal frequencies are closely packed within an interval of $(27.38 - 23.09)f_0 = 4.29f_0$ independent frequencies. The interference of these four signals enhances the misleading effects of Equations 51 and 52. The amplitudes of $S_{10,y}$, $S_{10,y6}$ and $S_{11,y86}$ signals are nearly equal. This causes many abrupt large $\Delta\phi \approx 0.5$ phase shifts during

$\Delta T = 274$ (Equation 53). Nevertheless, the DFT pre-whitening analysis succeeds, because signal S_{11y} amplitude $A_1 = 90.4$ is crucially larger than signal S_{10y} , $S_{10.y6}$ and $S_{11.y86}$ amplitudes. As predicted by Equation 52, this S_{11y} signal is detected first. After the pre-whitening subtraction of this strongest signal, the remaining S_{10y} , $S_{10.y6}$ and $S_{11.y86}$ signals no longer suffer from the f_0 limitation of Equation 50. The two highest amplitude $A_2 = 70.5$ and $A_3 = 57.4$ signals S_{10y} and $S_{11.y86}$ are now “comfortably separated” by $(27.38 - 23.09)f_0 = 4.29f_0$ independent frequencies. As predicted by the relation of Equation 52, these two signals are detected next (Figure 18c-f). The frequency difference between the remaining $S_{10.y6}$ and S_{110y} signals is so large that DFT can easily detect them. Our DFT pre-whitening analysis of sample **Rmonthly** succeeds, because one strong S_{11y} signal dominates, and the remaining signals are detected in a suitable order. This successful DFT analysis also confirms that the data does not contain any misleading long-term trends.

Our Table 13 gives the significance estimates for the DCM and DFT period detections from the **Rmonthly** sample. The DCM gives no direct significance estimate for the first detected 11.032 year period, which has certainly been detected for more than million times from the sunspot data. The DCM detections for the next six periods are extremely significant because the Fisher-test always rejects the H_0 hypothesis at critical levels $Q_F < 10^{-16}$ (Equation 28). The DCM model for the eighth 8.456 year period is unstable (Table 18, $M=8$).

For the DFT analysis, our Table 13 gives the values for the term

$$E_{\text{DFT}} = e^{-(n/2)(1+\xi^{-1})^{-1}}, \quad (55)$$

which is used to compute the false alarm probability Q_{DFT} (Horne and Baliunas, 1986, their Equation 22). All E_{DFT} values are so close to zero that all false alarm probabilities Q_{DFT} are practically equal to zero, which means that all DFT period detections are extremely significant.

Unless the solar cycle, the first detected 11 year signal, is an artefact, the DCM detections of all other signals are extremely significant ($Q_F < 10^{-16}$). In short, all DCM and DFT period detections in Table 13 are absolutely certain, if the data contain only white noise. One could argue that our significance estimates can be unreliable because we do not consider the possibility that the data contains red noise (Vaughan, 2005). We test the H_0 hypothesis in our DCM analysis with the Fisher-method (Equation 28). If the data contained red noise, it would influence both the simple model and the complex model of the Fisher-test. Hence, our the DCM analysis results are correct with or without the red noise. We admit that the red noise could contaminate our DFT analysis significance estimates, but then again we detect the same periods with the DCM and the DFT. For some reason, the extreme significance estimates for the DFT period detections from the sunspot data have not caught the attention that they would have deserved in the earlier studies (e.g., Zhu and Jia, 2018).

Finally, we repeat the daily sunspot data DFT pre-whitening analysis in Zhu and Jia (2018). They did not detect the S_{110y} signal because they searched for periods between 2 and 18 years. For our tested period interval between 5 and 200 years, DFT detects the five strongest 10.87, 10.14, 110.6, 12.00, and 7.99 year signals. These five periods are close to the five best periods that DCM detects in the weighted data (Table 6: Columns 7 and 13). The probable cause for the minor numerical value differences is that DFT tends to detect less accurate real period values than DCM (Sections 8.2 and 8.3). Our DFT detection of the 110.6 signal from these daily sunspot data removes the two weak 8.92 and 5.44 year signals detected by Zhu and Jia (2018). We do not apply DCM to the daily sunspot data for a simple reason. For a cluster of parallel computation processors, it takes about two days to compute the four signal DCM model for one

Table 13. Significance estimates for DCM and DFT period detections from **Rmonthly** sample. (1) Detection order. (2) DCM period P . (3) DCM critical level Q_F (Equation 28). (4) DFT period P . (5) DFT term E_{DFT} (Equation 55). (6) DFT false alarm probability Q_{DFT} . Note that DCM model for period 8.456 is unstable (“UM”).

DCM			DFT		
(1)	P	Q_F	(4)	E_{DFT}	Q_{DFT}
(-)	(y)	(-)	(y)	(-)	(-)
1	11.0324	—	11.002	1.8×10^{-162}	0
2	10.0001	$< 10^{-16}$	10.020	5.5×10^{-128}	0
3	11.807	$< 10^{-16}$	11.798	1.7×10^{-103}	0
4	99.92	$< 10^{-16}$	98.886	1.7×10^{-90}	0
5	10.569	$< 10^{-16}$	10.602	4.0×10^{-102}	0
6	52.66	$< 10^{-16}$	8.460	2.2×10^{-58}	0
7	8.1087	$< 10^{-16}$	52.567	8.9×10^{-59}	0
8	8.456UM	$< 10^{-16}$	67.627	4.0×10^{-41}	0

monthly sunspot data sample. For one daily sunspot data sample, this four signal DCM model computation would take months, and computations of many samples would take years.

We conclude that the DFT cross-check presented in this Section 8 confirms that our earlier DCM analysis results are correct.

9. Discussion

We discuss eight important questions that arose during this study and answer those questions.

It is an easy routine task for DCM to detect the five strongest S_{11y} , S_{10y} , $S_{11.y86}$, S_{110y} and $S_{10.y6}$ signals in the small non-weighted yearly sunspot number sample **Ryearly**. The same four strongest signals are also detected in the weighted yearly sunspot number sample **Cyearly**, but the fifth strongest signal changes from the $S_{10.y6}$ signal to the S_{8y} signal (Table 6). These results already raise some interesting questions.

1. Why are the S_{11y} and S_{10y} signal periods close integer multiples of Earth’s orbital period?
2. Why is the $S_{11.y86}$ signal period so close to Jupiter’s orbital period?
3. Why does Equation 47 connect all five S_{11y} , S_{10y} , $S_{11.y86}$, S_{110y} and $S_{10.y6}$ signal periods?

We shall forget the planets for a moment. Let us concentrate only on the statistics and the direct detection of signals (Section 5). Could it be that the one-year window in the above two yearly sunspot number samples somehow causes biased DCM detections of integer period values? The answer is “no”, because DCM detects the same signals in the twelve times larger, and temporally denser, monthly sunspot data samples **Rmonthly** and **Cmonthly**.

Could it be that these signals are present only in the larger yearly and monthly samples, but not in their shorter subsamples? Again, the answer is “no”. The non-weighted and the weighted DCM analysis reveals the same signals in the monthly and yearly subsamples (Table 6).

Answer to questions 1-3: Regardless of the cause of these signals, DCM detects all periods directly from the sunspot data. The detected period values confirm that the sampling and

consistency criterion C1 is fulfilled (Section 5). We will discuss the possible the planetary period connection later (see Question 5).

The next obvious question is

4. If these signals are real, can they be used to predicting the sunspot numbers?

The answer is “yes”, because DCM detects the strongest signals that dominate the long-term sunspot number changes. There are two alternatives to test this predictability (Section 6).

The first predictability test alternative is to divide the larger samples of all data into smaller samples of predictive data and predicted data. The predictive data are the observations before the year 2000, and the predicted data are the observations after the year 2000. Each new signal detected in the predictive data gives a predicted test statistic value z_{pred} (Equation 30) for the predicted data. These z_{pred} values should keep on decreasing as long as DCM detects new real periods in the predictive data.

Our most convincing z_{pred} parameter prediction is shown in Figures 10ab. The z_{pred} values decrease until six real pure sine signals are detected (Figure 10a). After that, these z_{pred} values begin to increase, which indicates that the detected seventh and eighth signals are no longer real. This six signal 22 years prediction from 2000 to 2022 is excellent (Figure 10b). The residuals for the predicted values follow a straight line, and are comfortably within red dotted curves denoting the $\pm 3\sigma$ errors of the predicting model. The accuracy of our prediction is far better than the four year s_{ISES} limit (Equation 33) denoted with the dash-dotted cyan lines. Our other two 22 years predictions based on the z_{pred} parameter also beat the four years s_{ISES} limit, because only a few residuals are outside this limit (Figures 7b and 8b).

The second alternative predictability test utilises the known time intervals of the past prolonged sunspot activity minima (Table 1). This allows us to compute the monthly or yearly time points t_i''' during each activity minimum interval. Now the DCM model for any analysed sample can be used to compute the predicted model values g_i''' at the time points t_i''' (Equation 31), which give the predicted mean level m_{pred} (Equation 32) during each activity minimum interval. The prediction becomes better, if this m_{pred} parameter decreases because we detect new real signals from the analysed sample. If this m_{pred} parameter starts to increase, we are no longer detecting real signals. In a good prediction, this m_{pred} value should fall below the mean m of all data.

Our best m_{pred} mean level predictions for Dalton and Maunder minima are convincing (Figures 9ab and 11ab). The predicting DCM model for the weighted data is a sum of five pure sines. In both cases, the black and the red squares denoting the m_{pred} values for Dalton and Maunder minima decrease, as expected, when new signals are detected (Figures 9a and 11a). Except for the Wolf minimum (green squares), the predicted mean m_{pred} values during all other activity minima dip below the mean m of all data denoted with a horizontal dotted black line. The best result of all is displayed by the green curve denoting the predicted long-term thirty-years sliding mean (Figures 9b and 11b). The minima of this curve coincide with the time intervals of the Dalton and Maunder minima. We are not aware of if anyone else has ever presented a similar successful backwards prediction of Dalton and Maunder minima. We emphasise that our prediction error estimates during the past two centuries (Figure 9b: red and green dotted lines) are more accurate than the ISES four year s_{ISES} limit of Equation 33 (Figure 9b: dash-dotted cyan lines).

The m_{pred} mean level prediction fails for the Maunder minimum, the closest activity minimum before the beginning of the analysed data sample (Figure 8d). The predicting DCM model for the non-weighted data is a sum of six double waves. This result is supported by the curve connecting the red squares denoting the Maunder minimum m_{pred} values. This curve decreases for four, five

and six signals, and increases for seven and eight signals (Figure 8d). We rate this prediction as “a partial success”, because only three m_{pred} values are slightly below the dotted black line, which denotes the mean level m of all data.

Two m_{pred} mean level predictions fail (Figures 7d and 10d). The predicting DCM models for these non-weighted data are sums of five and six pure sines, respectively. The Maunder minimum is the closest activity minimum before the beginning of these two samples. In both cases, all red squares denoting the Maunder minimum predicted mean m_{pred} values stay above the mean level m of all data, which is denoted with a dotted black line. DCM can use the error information only in the analysis of weighted data. The absence of this error information, and the lower accuracy of the older data, could explain, why our predictions for the past activity minima are better for the weighted data (Figures 9ab and 11ab), and worse for the non-weighted data (Figures 7d, 8d and 10d).

Answer to question 4: The predictability criteria C2 and C3 are fulfilled (Section 6).

Unlike the four first questions, the next question is no longer only statistical.

5. Can the detected signals be connected to the planets?

We first apply DCM to search for periods between $P_{\text{min}} = 5$ and $P_{\text{max}} = 200$ years (Sections 4-6). Mercury’s, Venus’, the Earth’s and Mars’ periods are outside our tested period range. Therefore, we perform another DCM search between $P_{\text{min}} = 0.1$ and $P_{\text{max}} = 5$ years (Section 7.1). We detect none of the four inner planet periods (Figure 12). We then consider the possibility that some detected signals may be integer multiple periods iP_{Planet} , where i is an integer and P_{Planet} is a planet’s period. If the planetary gravitational tidal forcing causes the detected signals (e.g. Stefani, Giesecke, and Weier, 2019; Cionco, Kudryavtsev, and Soon, 2023), these integer multiple periods may be caused by Mercury, Venus, the Earth and Jupiter (Table 8: Equation 34).

The statistics required for detecting iP_{Planet} integer multiple periods force us to define many new parameters (Equations 35-38, 43 and 44). We use these parameters to identify the best integer multiple period candidates. We can infer that the detection of integer multiple periods is easier for longer planetary periods (Equations 39 and 43), i.e., integer multiple period detection is most difficult for Mercury, and it is easiest for Jupiter. This inference can be amply confirmed by comparing Figures 13a-d and 14a-d. We first compute Mercury’s, Venus’, and Jupiter’s rounds \mathcal{P} values (Equation 35) for the detected signals (Table 9), and then identify the most promising integer multiple period candidates (Table 10). These candidates are

$$\begin{aligned} S_{8y} &\cong 13 \times P_{\text{Venus}} \cong 8 \times P_{\text{Earth}} \text{ (Figures 13ab)} \\ S_{10y} &\cong 41.5 \times P_{\text{Mercury}} \cong 10 \times P_{\text{Earth}} \text{ (Figures 13cd)} \\ S_{10,y_6} &\cong 44 \times P_{\text{Mercury}} \text{ (Figure 14a)} \\ S_{11y} &\cong 11 \times P_{\text{Earth}} \text{ (Figure 14b)} \\ S_{11,y_86} &\cong 49 \times P_{\text{Mercury}} \cong 1 \times P_{\text{Jupiter}} \text{ (Figures 14cd)} \end{aligned}$$

The S_{10y} , S_{11y} , S_{11,y_86} and S_{10,y_6} signals are connected to the S_{110y} signal (Table 11).

The rounds \mathcal{P} (Equation 35) values for different signals deviate from the identified integer multiple value \mathcal{P}_0 (Equation 37). Some, but not all, of these rounds deviations $\Delta\mathcal{P}$ (Equation 37) can be attributed to the integer multiple period statistics (Equations 39 and 43). We solve how the migration of primary minima $t_{\text{min},1}$ and primary maxima $t_{\text{max},1}$ of different signals depends on $\Delta\mathcal{P}$ (Equations 40-44). Different signals have different mean anomaly migration lines (Equation 45). If these migration lines intersect at a convergence point M_C (Equation 46), all different signals can represent the same signal connected to the integer value \mathcal{P}_0 (Equation 37). More than two migration lines may converge by accident, but not all migration lines of

all samples! This linear convergence is very convincing for the S_{10y} signal (Figure 13d), the S_{11y} signal (Figure 14b) and the $S_{11.y86}$ signal (Figure 14d). As expected, the convergence point identification is more difficult for Venus' and Mercury's signal candidates (Equations 39 and 43).

Criterion C4 requires that some of the detected signals can be connected to the orbital periods of planets. The most convincing planetary period candidate is the $S_{11.y86}$ signal, which can be connected to Jupiter's orbital period (Figures 14d), as well as to Jupiter's orbital motion (Figure 15). The second-best integer multiple period candidates are the S_{10y} and S_{11y} signals, which may be connected to the Earth (Figures 13d and 14b). It is quite a coincidence that we first detect $11 \times P_{\text{Earth}}$ and $10 \times P_{\text{Earth}}$, and then exactly $1 \times P_{\text{Jupiter}}$. The detected signs of Venus' and Mercury's integer multiple periods are less convincing due to the known statistical effects (Equations 39 and 43).

Answer to question 5: The planet identification criterion C4 is fulfilled (Section 7).

The next interesting question is purely statistical.

6. Is it possible to cross-check our DCM analysis results?

We use the Discrete Fourier Transform (Horne and Baliunas, 1986, DFT) to cross-check our Discrete Chi-square Method (DCM) analysis results (Section 8). Before this cross-check, we compare the performance of DFT and DCM. We simulate noisy data, which contains only the S_{10y} and S_{11y} signals (Section 8.1). The analysis of these simulated data reveals at least five DFT drawbacks (Sections 8.2 and 8.3). DFT may not detect two close frequencies (Equation 50). DFT may detect wrong periods (Equations 51 and 52). DFT can not model abrupt phase shifts (Equation 53). DFT pre-whitening may give biased residuals. DFT may detect periods deviating from the simulated real period values. DCM suffers from none of the above five DFT drawbacks (Figures 16 and 17).

Regardless of all DFT drawbacks, our DFT pre-whitening analysis of sample R_{monthly} succeeds and confirms our earlier DCM analysis results (Figure 18). For both methods, the five strongest signals are the same, except for minor numerical differences. For example, DFT detects the $S_{11.y86}$ signal period $11.y798$, while DCM detects the $11.y846$ period, which is closer to the orbital period $P_{\text{Jupiter}} = 11.y857$. This result could be expected, because our simulations already show that DFT tends to detect less precise real period values than DCM (Figures 16 and 17: vertical dashed lines at real period values). Our DFT pre-whitening analysis of real data sample R_{monthly} succeeds, because the strong S_{11y} signal is detected first, and then the remaining signals can be detected in a suitable order.

If we had analysed the sunspot data using only the DFT pre-whitening technique, all above-mentioned DFT method drawbacks could have been used to dispute our results. We can now disregard such argumentation, because DFT pre-whitening analysis detects the same signals as our DCM pure sine model analysis. Both DCM and DFT analyses use the same model: sum of pure sines. DFT pre-whitening detects one period at the time, while DCM detects many periods simultaneously. We obtain the same results with these two different time series analysis methods!

Answer to question 6: The DFT cross-check confirms our DCM analysis results.

The next relevant question is

7. Do we detect real signals?

We detect “old” and “new” signals in the sunspot data. The “old” accepted real signal detections are those made by Schwabe (1844, 10 years $\equiv S_{10y}$ signal) and Wolf (1852, 11.1 years $\equiv S_{11y}$ signal). We confirm that their detections were correct. The third “new” signal most probably represents Jupiter's period ($P_{\text{Jupiter}} = 11.857$ years $\equiv S_{11.y86}$ signal). This detection

of Jupiter's period is hard to deny, when our 10 and 11-year cycles re-detections from the very same data have been accepted for nearly two centuries. Furthermore, why would DCM detect just this kind of an “unreal” $S_{11,y86}$ signal in all analysed samples? The next “new” detections are the S_{110^y} and $S_{10,y6}$ signals. The interference pattern of the above-mentioned five signals is repeated indefinitely, because these five signals are interconnected (Table 11: Equation 47). If our detections of these old and new signals were dismissed as unreal, it would mean that both DCM and DFT analyses give the same wrong results. For example, we admit that visual inspection and statistical inference are two completely different approaches, but there must be a reason why the $y_{i,j}$ and $h_i(t)$ changes as a function of phase look like strong real signals in Figure 5 (left panels), where the red, blue and green curves denote the S_{10^y} , S_{11^y} and $S_{11,y86}$ signals, respectively.

These data allow outstanding predictions, like those in Figure 9b (green curve 200 years backwards), Figure 10b (red curve 22 years forwards) and Figure 11b (green curve 200 years backwards). Such predictions would be impossible, if the detected signals were unreal. This indicates that the sunspot cycle is deterministic, not stochastic. The interference of many signals causes an apparent stochasticity effect, which modifies the length and shape of individual solar cycle curves. We have detected only the strongest signals, which already give good predictions for the thirty years sliding mean (Figures 7-11: green curves). These thirty years sliding mean predictions are always more accurate than the individual cycle predictions (Figures 7-11: red curves). Therefore, the green curve errors (dotted green lines) are always smaller than the red curve errors (dotted red lines). More accurate predictions for individual solar cycles can require the detection of lower-amplitude signals. Such detections may succeed when the data time span increases, but only if the amplitude of noise is significantly lower than the wandering ISES limit $s_{\text{ISES}} = \pm 50$ during four years (Figure 2: Equation 33). Our predictions do not wander even in decades (Figure 10b) or centuries (Figure 9b and 11b). The successful Maunder and Dalton minima predictions (Figures 9b and 11b: green curves) do indicate that our solar activity mean level predictions for the next centuries can be correct.

Answer to question 7: We re-detect the old accepted real 10 and 11 year signals (Schwabe, 1844; Wolf, 1852). One of the detected new signals is most probably the $S_{11,y86}$ signal of Jupiter. The detected signals can be used to predict the past and the future sunspot data. All these results indicate that we detect real signals.

The crucial astrophysical question is

8. What physical mechanism causes these signals?

In time series analysis, the detected periods are usually considered real if they have an accepted physical cause, like in the DCM analysis by Jetsu (2021). Here, such a widely accepted cause for the detected strictly periodic signals is missing.

Parker (1955) formulated the dynamo model, where the interaction of differential rotation and convective motion drives the solar magnetic field. The first models for a dynamo generated sunspot cycle were presented by Babcock (1961) and Leighton (1969). All dynamo model physical mechanisms causing the solar cycle are not yet fully understood (Charbonneau, 2010). As stated in our H_{Dynamo} hypothesis, it is widely accepted that the solar cycle is stochastic and unpredictable beyond one solar cycle (Petrovay, 2020). For example, the ISES panel predictions cover only the ongoing cycle (Figure 2). If these predictions were made for several cycles in a row, the prediction errors would certainly exceed the four year ISES limit (Equation 33).

It is unnecessary to argue what physical mechanism inside the solar system can cause the detected strictly periodic signals, which allow deterministic predictions. What else could this cause be, except the planets? This would mean that the solar cycle is not generated only by the physical mechanisms inside the Sun. We consider two alternative external causes: the planetary gravitational forces and the planetary magnetic forces.

Table 14. Three strongest signals in all data samples. (1) Sample: $K_2 = 1$ or 2 model. (2) Signal S_{11y} : Period P_{11y} and amplitude A_{11y} . (3-4) Same for S_{10y} and $S_{11.y86}$ signals. (5) R_{Signal} (Equation 56). (6) R_{Signal} (Equation 57). Lowest line gives period, amplitude, and R_{Signal} weighted means. Note that S_{10y} signal in Rmonthly : $K_2 = 2$ is a double sinusoid $^{2\times}$.

(1)	(2)	(3)	(4)	(5)	(6)
Sample: K_2	S_{11y} $P_{11} (\text{y})$ $A_{11} (-)$	S_{10y} $P_{10} (\text{y})$ $A_{10} (-)$	$S_{11.y86}$ $P_{11.86} (\text{y})$ $A_{11.86} (-)$	$R_{\text{Signal}} (-)$	$R_{\text{Signal}} (-)$
$\text{Rmonthly: } K_2 = 1$	11.0033 ± 0.0064 101.5 ± 2.5	10.0001 ± 0.0081 65.5 ± 2.1	11.807 ± 0.012 56.4 ± 2.4	0.338 ± 0.016	0.861 ± 0.046
$\text{Rmonthly: } K_2 = 2$	10.9878 ± 0.0051 104.6 ± 2.3	$10.0031 \pm 0.0044^{2\times}$ 75.2 ± 2.7	11.770 ± 0.011 62.7 ± 2.6	0.349 ± 0.016	0.834 ± 0.046
$\text{Cmonthly: } K_2 = 1$	10.8585 ± 0.0048 117.5 ± 2.9	10.0658 ± 0.0077 59.3 ± 2.8	11.863 ± 0.021 43.3 ± 2.0	0.245 ± 0.013	0.730 ± 0.048
$\text{Ryearly: } K_2 = 1$	10.981 ± 0.020 98.3 ± 7.8	9.975 ± 0.017 62.8 ± 6.1	11.820 ± 0.027 40.5 ± 3.3	0.251 ± 0.026	0.645 ± 0.081
$\text{Cyearly: } K_2 = 1$	10.863 ± 0.022 119.3 ± 7.5	10.058 ± 0.026 61.0 ± 9.6	11.856 ± 0.068 43.8 ± 7.9	0.243 ± 0.047	0.718 ± 0.17
Weighted mean	10.938 ± 0.066 107.0 ± 6.8	10.014 ± 0.026 66.3 ± 5.8	11.799 ± 0.031 50.5 ± 8.6	0.294 ± 0.048	0.739 ± 0.072

Recently, several attempts have been made to model an internal solar dynamo influenced by external gravitational tidal forces of planets. Stefani, Giesecke, and Weier (2019) presented a solar dynamo, where the planetary tidal forcing causes periodic 11.07 and 22.14-year magnetic field oscillations. Scafetta and Bianchini (2022) reviewed the possible physical mechanisms that could explain how the weak planetary tidal forces can alter the solar structure and cause the sunspot cycle. Charbonneau (2022) showed that if the external planetary signal is not constantly amplified, the internal solar dynamo mechanism fluctuations can mask this external signal. More recently, Cionco, Kudryavtsev, and Soon (2023) argued that the combined tidal forcing of Venus, the Earth and Jupiter can not cause the 11-years solar cycle.

We give the weighted mean periods and amplitudes of the three strongest signals in Table 14.

The weighted mean $P_{11y} = 10.938 \pm 0.066$ years period of the strongest S_{11y} signal differs 0.94σ from $11 \times P_{\text{Earth}}$. The 0.26σ difference from $10 \times P_{\text{EJ}} = 10.921$ years is even smaller, where $P_{\text{EJ}} = 1.0921$ years is the synodic period of the Earth and Jupiter. The Earth may cause this strongest S_{11y} signal alone, or together with Jupiter.

The weighted mean $P_{10y} = 10.014 \pm 0.026$ years period of the second strongest S_{10y} signal differs 0.54σ from $10 \times P_{\text{Earth}}$. This signal is probably connected only to the Earth, because the closest $9 \times P_{\text{EJ}} = 9.829$ years synodic period multiple is 7.1σ away.

The third strongest $S_{11.y86}$ signal has $P_{11.y86} = 11.799 \pm 0.031$ years weighted mean period, which differs 1.9σ from the $P_{\text{Jupiter}} = 11.857$ years period. Since the closest $11 \times P_{\text{EJ}} = 12.013$ years synodic period multiple is 5.0σ away, this $S_{11.y86}$ signal is probably connected only to Jupiter.

If the $S_{11.y86}$ signal is connected only to Jupiter, and the S_{11y} and S_{10y} signals are connected only to the Earth, the weighted mean of Jupiter's and the Earth's signal amplitude ratio is

$$R_{\text{Signal}} = A_{11.y86} / (A_{11y} + A_{10y}) = 0.294 \pm 0.048. \quad (56)$$

If the S_{11y} signal is connected to both the Earth and Jupiter, the weighted mean signal amplitude ratio is

$$R_{\text{Signal}} = A_{11,y86}/A_{10y} = 0.739 \pm 0.07. \quad (57)$$

In this relation, we assume that Jupiter's and the Earth's amplitude ratio is equal to R_{Signal} also in the S_{11y} signal. For both alternative Equations 56 and 57, the Earth's gravitational tidal forces should dominate over those of Jupiter, which is not true (Table 8). This would exclude the alternative that the external planetary tidal forces cause the sunspot cycle.

The electromagnetic force is 10^{40} times stronger than the gravitational force (Gillies, 1997). For a proton at the distance of Earth, the force due to the solar magnetic field is 60 000 stronger than the solar gravitational force (Alfvén, 1942). Jupiter and the Earth have the strongest planetary magnetic fields in the solar system (Schubert and Soderlund, 2011, their Table 2). Mercury has only a weak magnetic field, and Venus has none. Hansson (2022) and Muñoz, Wagemakers, and Sanjuán (2023) have formulated models, where the solar dynamo and the planetary magnetic fields interact, and cause the solar cycle. A similar interaction of magnetic fields has also been modelled for "hot Jupiter" exoplanets, but the results are uncertain, because the stellar magnetic field geometry is unknown (Ip, Kopp, and Hu, 2004; Cranmer and Saar, 2007). As for the solar magnetic field geometry, Parker (1958) first showed that at certain distances this field falls inverse squared r^{-2} due to the solar wind, and then he finally noted that the observations support the existence of a more complicated field structure. Our strongest candidates for planetary signals, the S_{11y} , S_{10y} and $S_{11,y86}$ signals, could indeed be connected to the Earth and Jupiter, having the strongest magnetic fields. Only one signal, the S_{8y} signal, could be connected to Venus, which has no magnetic field. These results would support the idea of magnetic field interaction, but do not prove it, because we have shown that Mercury's and Venus' signal detection is statistically more difficult than the Earth's and Jupiter's signal detection (Equations 39 and 43).

The interaction between stellar and exoplanet magnetic fields has been estimated by Cranmer and Saar (2007, Equation 2). We assume that their estimate can also be applied to the solar system because the solar magnetic field interacts with the planetary magnetic fields during FTEs (Dungey, 1961; Nakariakov et al., 2016; Paul, Vaidya, and Strugarek, 2022; Sun et al., 2022). Our notations for a solar system planet are a = semi-major axis of orbit, v = orbital velocity, R = radius, and B_{Planet} = magnetic field strength given in Schubert and Soderlund (2011). The connection between the parameters in Cranmer and Saar (2007, Equation 2) and our parameters are $B_{\star} \equiv B_{\text{Sun}}(a)$ = solar magnetic field strength at distance a , $B_P \equiv B_{\text{Planet}}$, $r_{\text{mag}} \propto R$ and $V_{\text{rel}} \equiv v$. Our dimensionless parameters are $a' = a/a_{\text{Earth}}$, $v' = v/v_{\text{Earth}}$, $R' = R/R_{\text{Earth}}$, $B'_{\text{Sun}} = B_{\text{Sun}}(a)/B_{\text{Sun}}(a_{\text{Earth}})$ and $B' = B_{\text{Planet}}/B_{\text{Earth}}$. We assume that $B'_{\text{Sun}} \propto a'^{n_{\text{Sun}}}$, where the unknown value can be $n_{\text{Sun}} = -1, -2$, or -3 . Cranmer and Saar (2007) assumed that the magnetic interaction is proportional to the exoplanet disk area $\propto R'^{n_{\text{Planet}}}$, where $n_{\text{Planet}} = 2$. We test other $R'^{n_{\text{Planet}}}$ alternatives, where the unknown n_{Planet} value can also be 0 (point source), 1 (planet's diameter), or 3 (planet's volume). Kepler's third law gives us $v' \propto a'^{-1/2}$ for circular orbits. Under all the above assumptions, the estimate in Cranmer and Saar (2007, Equation 2) gives the relative magnetic interaction parameter

$$R_{\text{Magnetic}} \propto a'^{(n_{\text{Sun}} - 1/2)} R'^{n_{\text{Planet}}} B'. \quad (58)$$

We compute the R_{Magnetic} values for all $n_{\text{Sun}} = -1, -2, -3$ and $n_{\text{Planet}} = 0, 1, 2, 3$ combinations (Table 15). Note that all twelve n_{Sun} and n_{Planet} combinations give $R_{\text{Magnetic}} = 1$ for the Earth. No one knows the correct n_{Sun} and n_{Planet} values, but we can test which combinations could

Table 15. Relative magnetic interaction parameters of planets. (1) Combination number (Com). (2-3) n_{Sun} and n_{Planet} (Equation 58). (4) R_{Magnetic} values for $a' = 0.387$, $R' = 0.351$ and $B' = 0.00789$ of Mercury (Equation 58). (5-11) R_{Magnetic} values for other planets.

Com	n_{Sun}	n_{Planet}	(1)	(2)	(3)	(4)	(5)	(6)	(7)	(8)	(9)	(10)	(11)
			Mercury	Venus	Earth	Mars	Jupiter	Saturn	Neptune	Uranus			
			$a' = 0.387$	$a' = 0.723$	$a' = 1$	$a' = 1.524$	$a' = 5.202$	$a' = 9.562$	$a' = 19.304$	$a' = 30.278$			
			$R' = 0.351$	$R' = 0.099$	$R' = 1$	$R' = 0.533$	$R' = 11.2$	$R' = 9.45$	$R' = 4.01$	$R' = 3.88$			
			$B' = 0.00789$	$B' = 0$	$B' = 1$	$B' = 0.00263$	$B' = 14.5$	$B' = 0.737$	$B' = 0.842$	$B' = 0.710$			
	(-)	(-)	(-)	(-)	(-)	(-)	(-)	(-)	(-)	(-)			
1	-1	0	0.033	0	1	0.0014	1.2	0.025	0.0099	0.0043			
2	-2	0	0.085	0	1	0.00092	0.23	0.0026	0.00051	0.00014			
3	-3	0	0.22	0	1	0.0006	0.045	0.00027	0.000027	0.0000047			
4	-1	1	0.012	0	1	0.00074	14.0	0.24	0.04	0.017			
5	-2	1	0.03	0	1	0.00049	2.6	0.025	0.0021	0.00055			
6	-3	1	0.077	0	1	0.00032	0.51	0.0026	0.00011	0.000018			
7	-1	2	0.004	0	1	0.0004	150.0	2.2	0.16	0.064			
8	-2	2	0.01	0	1	0.00026	29.0	0.23	0.0083	0.0021			
9	-3	2	0.027	0	1	0.00017	5.7	0.024	0.00043	0.000070			
10	-1	3	0.0014	0	1	0.00021	1700.0	21.0	0.64	0.25			
11	-2	3	0.0037	0	1	0.00014	330.0	2.2	0.033	0.0082			
12	-3	3	0.0095	0	1	0.000091	63.0	0.23	0.0017	0.00027			

support our R_{Signal} values (Equations 56 and 57). For example, Parker (1958) arrived at the value $n_{\text{Sun}} = -2$ for the Sun, while Cranmer and Saar (2007) used $n_{\text{Planet}} = 2$ for an exoplanet.

Jupiter dominates in nine n_{Sun} and n_{Planet} combinations (Table 15). Our results indicate that the Earth should dominate (Equations 56 and 57). The Earth, having $F_{\text{magnetic}} = 1$, does dominate in the three remaining possible combinations.

The Earth dominates in the Com=2 combination, where the $n_{\text{Sun}} = -2$ and $n_{\text{Planet}} = 0$ values give $R_{\text{Magnetic}} = 0.23$ for Jupiter, which differs only 1.3σ from $R_{\text{Signal}} = 0.294 \pm 0.048$ (Equation 56). In this case, the S_{11y} and S_{10y} signals are caused only by the Earth, and the $S_{11,y86}$ signal is caused only by Jupiter. This $n_{\text{Sun}} = -2$ and $n_{\text{Planet}} = 0$ combination would support the solar magnetic field relation r^{-2} in Parker (1958), and it also indicates that the planets can be treated as point sources.

The Earth dominates in the Com=3 combination $n_{\text{Sun}} = -3$ and $n_{\text{Planet}} = 0$, which gives $R_{\text{Magnetic}} = 0.045$ for Jupiter. This result contradicts both $R_{\text{Signal}} = 0.294$ (Equation 56) and $R_{\text{Signal}} = 0.793$ (Equation 57) because Jupiter's influence is underestimated.

In the Com=6 combination, the Earth dominates because the $n_{\text{Sun}} = -3$ and $n_{\text{Planet}} = 1$ values give $R_{\text{Magnetic}} = 0.51$ for Jupiter. This value differs 4.5σ from $R_{\text{Signal}} = 0.294 \pm 0.048$ (Equation 56) and 3.2σ from $R_{\text{Signal}} = 0.739 \pm 0.072$ (Equation 57). However, the numerical $R_{\text{Magnetic}} = 0.51$ value is 0.013 closer to $R_{\text{Signal}} = 0.294$ than $R_{\text{Signal}} = 0.739$. The $n_{\text{Sun}} = -3$ value would support the r^{-3} relation between two dipole magnetic fields (Ku et al., 2016, their Equation 1). The value $n_{\text{Planet}} = 1$ means that the interaction in Equation 58 is proportional to the planet's diameter R' .

The geomagnetic field dominates the sunspot cycle in the two remaining Com=2 and 6 combinations. This would explain the strongest S_{11y} and S_{10y} signals. Jupiter's contribution would be weaker, and cause the third strongest $S_{11,y86}$ signal. The interference of these three signals would cause the other $S_{10,y6}$ and S_{110y} signals (Table 11). Mercury would have a weak contribution. The contributions of Venus, Mars, Saturn, Neptune and Uranus would be insignificant.

The FTE are the only known physical mechanisms, where the planetary magnetic fields can interact *directly* with the solar magnetic field. At the Earth, these FTE reconnections occur at the dayside and the FTE magnetic flux ropes roll from low latitudes towards the winter pole (Raeder, 2006; Fear, Palmroth, and Milan, 2012; Nakariakov et al., 2016; Zhang et al., 2022).

Hence, the FTE magnetic flux ropes are switching between the N and S poles of the terrestrial magnetic field. Due to the Earth's orbital motion, this rolling repeats a strict regular magnetic FTE pole switch period

$$P_{\text{FTE}} = P_{\text{Earth}} = 1^y. \quad (59)$$

High-energy particles are constantly flowing through the FTE magnetic flux ropes from the Sun to the planets. This must have some effect. We performed an extensive ADS database⁵ literature search for studies, where the FTEs are connected to the sunspots. We could find only two such studies, which propose that the FTEs may be connected to the formation of sunspots (Pease and Glenn, 2016) and to the sunspot cycles (Glenn, 2019). We test this hypothesis

H_{FTS} : “FTEs cause sunspots.”

This hypothesis could explain, for example, the following observations of the sunspots.

1. If H_{FTS} we true, there would be the following relatively simple explanation for the Hale's law, the sunspots cycles and the differential rotation. We denote the polarity of the global solar dipole magnetic field with P_{Sun} . This polarity is opposite on the northern and southern hemispheres. Our notation is $P_{\text{Sun}} = A$, where A is N or S.
 - 1a. As the FTE begins, the polarity at FTE magnetic flux rope footpoint on solar surface is the same as $P_{\text{Sun}} = A$ and this causes the leading A polarity sunspot. The magnetic flux through the rope weakens $P_{\text{Sun}} = A$.
 - 1b. During the FTE, the polarity is $P_{\text{Planet}} = B$ at the planetary end of the FTE magnetic flux rope, where B is opposite to A .
 - 1c. As the FTE ends, the planetary FTE magnetic flux rope reconnects to the Sun and causes the trailing B polarity sunspot. The trailing sunspot trails because the trailing Parker spiral trails. This trailing B polarity sunspot weakens $P_{\text{Sun}} = A$.
 - 1d. At both solar hemispheres, the constantly forming new trailing B polarity sunspots weaken the solar $P_{\text{Sun}} = A$ dipole field, until it flips, and a new sunspot cycle begins. The dipole magnetic fields of planets do not flip.
 - 1e. If the A and B polarity FTE magnetic flux rope footpoints are deeper below the solar surface, there is a time delay between the FTEs and the emergence of sunspot pairs. This would neatly explain why the connection between the FTEs and the sunspots has not been discovered earlier.
 - 1f. The planet moves against the rotating Parker spiral. If the dragging of FTE magnetic flux ropes transfer some kinetic energy from the planetary motion to the solar convective zone, this effect is strongest at the solar equator. This effect may even be weak, but nothing has prevented it from accumulating during the lifetime of the Sun. This could explain the differential rotation.
2. If the relation in Equation 58 is correct, the terrestrial dipole magnetic field would have the strongest influence on the formation of sunspots (Table 15: Com=2 and 6). In this case, the ten and the eleven year multiples of the FTE pole switch periods $P_{\text{FTS}} = P_{\text{Earth}}$ may cause the strongest S_{11^y} and S_{10^y} sunspot cycles. For example, Hansson (2022) and Muñoz, Wagemakers, and Sanjuán (2023) have presented models, where this kind of repetitive strictly periodic magnetic perturbations cause the sunspot cycle. If the relation $P_{\text{FTS}} = P_{\text{Jupiter}}$ (Equation 59) also holds for the dipole magnetic field of Jupiter, it may cause the third strongest S_{11^y86} cycle.

⁵NASA ADS-database.

Table 16. Observed flux rope diameter upper limits. (1-3) Mercury: Diameter (D), Number of FTEs (n_{FTE}), Reference. (4-6) Same for the Earth. (7-9) Same for Jupiter. Notation “-” means that n_{FTE} is unknown.

Mercury			Earth			Jupiter		
(1) D (R_{Mercury})	(2) n_{FTE} (-)	(3) Reference	(4) D (R_{Earth})	(5) n_{FTE} (-)	(6) Reference	(7) D (R_{Jupiter})	(8) n_{FTE} (-)	(9) Reference
1.04	5	2	2	152	1	3*	4	4
0.61	-	3	0.47	1	5	0.19	2	8
1.48	16	6	1.25	55	7	0.24	1	9

References: (1) Rijnbeek et al. (1984), (2) Slavin et al. (2010), (3) Slavin et al. (2012), (4) Vogt et al. (2014), (5) Hasegawa et al. (2015), (6) DiBraccio et al. (2015), (7) Akhavan-Tafti et al. (2018), (8) Sarkango et al. (2021), (9) Sarkango et al. (2022).

*Mean diameter of 43 plasmoids: Only 4 of these plasmoids were classified as flux ropes.

The FTE magnetic flux ropes of the Earth and Jupiter may constantly perturb the Sun, until its dipole magnetic field repetitively flips after about 11 years. At the sunspot cycle minimum, the solar magnetic field also becomes a dipole (Parker, 1955).

3. Russell (1995) analysed the Pioneer 10 and 11, Voyager 1 and 2 and Ulysses satellite observations of Jupiter’s FTEs. The durations and the temporal separations of FTEs were similar for the Earth and Jupiter. However, the amplitudes of terrestrial FTEs were about four times larger than the amplitudes of Jupiter’s FTEs when scaled by the planetary magnetic field inside the magnetopause. We use the same scaling for the dimensionless magnetic field parameter B' in Equation 58. If the relative FTEs amplitude ratio between Jupiter and Earth is denoted $R_{\text{FTE}} = 1/4$, our results fulfil

$$R_{\text{Signal}} = 0.294 \pm 0.048 \text{ (Equation 56)} \approx R_{\text{Magnetic}} = 0.23 \text{ (Table 11: Com=2)} \approx R_{\text{FTE}} = 0.25(60)$$

4. The FTE magnetic flux rope diameters of the Earth, Jupiter and Mercury are comparable to the diameters of these three planets (Table 16). Our results indicate that the Earth may have the strongest influence on the sunspot cycle (Table 15: Com=2 and 6). The average diameter of sunspots is about same as the diameter of the Earth (Macdonald, 2012; Luminița, Laurențiu, and Constantina, 2023). The sunspot diameter’s range is between 16 km and to 160 000 km (Birch and Bromage, 2022). The largest sunspots have diameters equal to the sum of the diameters of the Earth, Jupiter and Mercury, 160 600 km. If the simultaneous FTEs of these three planets cause the largest sunspots, the 160 000 km upper limit would make sense. The weakest FTEs of Mercury could explain the 16 km lower limit of sunspot diameters. About $8.1 \pm 0.5\%$ of all sunspots do not obey Hale’s law (Li, 2018). Since this fraction is of the same order as $R_{\text{Magnetic}} = 0.085$ for Mercury (Table 15: Com=2), these weaker “anti-Hale” sunspots may be caused by Mercury’s FTEs. Mercury is so close to the Sun that the shape of the Parker spiral does not necessarily determine the order of the leading and trailing sunspots. All this fits to the strongest influence of the Earth, Jupiter and Mercury, and especially in this particular order (Table 15: Com=2 and 6). These connections between the sunspot diameters and the diameters of the Earth, Jupiter and Mercury may not be a coincidence.

5. The $P_R = 155 - 160$ days Rieger cycle in the solar flares was discovered by Rieger et al. (1984). This cycle has been later discovered in many other solar activity indices, including the

sunspots, and the full periodicity range is between 155 and 190 days (Gurgenashvili et al., 2017). These periods are about half of the 365 days FTE pole switch period (Equation 59). Numerous P_R period subharmonics have also been detected (Dimitropoulou, Moussas, and Strintzi, 2008). The FTEs are most frequent during periods of southward interplanetary magnetic field (IMF) when the magnetic shear between the IMF and the geomagnetic field is strongest (Phan et al., 1994; Scurry, Russell, and Gosling, 1994). Since the shear changes are strictly periodic, the 27.4 days IMF rotation period (Xiang, Ning, and Li, 2020) could cause the Rieger P_R period subharmonics, and the 26.7 days period in the major solar flares (Bai, 1987; Jetsu et al., 1997). All sunspots caused by Jupiter's and Mercury's FTEs would not be connected to the Rieger periods.

There must be an astrophysical mechanism that causes the detected predictive strictly periodic and extremely significant signals in the sunspot data, unless both DCM and DFT give the same misleading results. Whatever this astrophysical mechanism may be, why would both of these statistical methods detect the same unreal signals that can predict real data? We present direct observational evidence that the signals in the sunspot data may be connected to the planetary motions and the FTEs. It is possible that the planetary motions can influence the solar cycle, but it is impossible that the solar magnetic field can influence the planetary motions. As far as we know, ours would be the first *direct* detection of the Earth and Jupiter from the sunspot data. The possible detections of Venus and Mercury are uncertain due to statistical reasons (Equations 39 and 43), and maybe also due to physical reasons (Equation 58). If our relative magnetic interaction Equation 58 is correct, the Earth, due to its iron core (Jephcoat and Olson, 1987), is an exceptional planet in the solar system. Direct observations of Earth-like exoplanets are difficult (Jenkins et al., 2015). If Earth-like planets can cause stellar activity cycles, innumerable indirect detections of such exoplanets have already been made (e.g. Baliunas and Vaughan, 1985). This would mean that the planets can cause the starspots, which in turn can prevent the detection of these planets (Korhonen et al., 2015). There may indeed also be a connection between stellar activity and exoplanets (e.g. Cuntz, Saar, and Musielak, 2000).

Astrophysical theories are used to construct models of astronomical phenomena. Observations are used to test these models. Statistical methods are not confined to any particular phenomenon. The same statistical method can be applied to different phenomena. No phenomenon can fool statistics. Phenomena are not stochastic only because they appear unpredictable. Phenomena may appear stochastic because we can not yet predict them. Our sunspot number predictions are accurate and the significance estimates for the signals are extreme. This does not support the mainstream dynamo-influence-theory H_{Dynamo} hypothesis of a stochastic sunspot cycle. From the time series analysis point of view, this is a clear-cut case. Our results support the deterministic planetary-influence-theory H_{Planet} hypothesis.

Answer to question 8: The orbital motion of the Earth and Jupiter may cause the S_{11y} , S_{10y} and $S_{11.y86}$ signals. The FTEs of these two planets may be the main cause for the sunspot cycle.

10. Conclusions

If the FTE of the Earth, Jupiter and Mercury cause the sunspots, it could explain the sunspots cycles, the Hale's law, the differential rotation and many other phenomena observed in the Sun, as well as in other chromospherically active stars. If we are correct, not a lot will remain of the dynamo theory.

The predictability of solar activity will allow us to prepare better for the climate change on the Earth and the catastrophic geomagnetic storms, like the Carrington event in the year 1859.

Acknowledgements We thank the Finnish Computing Competence Infrastructure (FCCI) for supporting this project with computational resources. We thank Juha Helin, Jani Jaakkola, Sami Maisala and Pasi Vettentranta who helped us utilise parallel computation resources in the High Performance Computing (HPC) platform. Veijo Niinikoski is acknowledged for pointing out that the Earth's and Jupiter's magnetic fields are much stronger than those of Venus and Mercury. We also thank Stefan Ahmala for drawing our attention to the possible electromagnetic interactions between the magnetic fields of solar system bodies. We thank professor Alexis Finoguenov for his insightful comments, as well as for recommending the use of grammar packages. This work has made use of NASA's Astrophysics Data System (ADS) services.

Appendix

Table 17. `Rmonthly2000` analysis for pure sines ($K_2 = 1$). (1) Model number (2) Model $\mathcal{M}_{K_1, K_2, K_3, R}$, number of free parameters η , and sum of squared residuals R . (3-6) Periods P , amplitudes A and primary minima $t_{\min,1}$ for one, two, three and four signal models. (7-9) Fisher-test comparison between models $\mathcal{M}=1, 2, 3$ and 4 . An upward arrow \uparrow indicates that complex model is better than simple model. A leftward arrow \leftarrow would be used, if simple model were the better one. (10) Electronic control file. Four first signals are detected from original data (file `Rmonthly2000.dat`). Next four model $\mathcal{M}=5-8$ signals are detected from residuals of model $\mathcal{M}=4$ (electronic file `RmonthlyK410R14Residuals.dat`). Models $\mathcal{M}=7$ and 8 are unstable (UM) because they suffer from amplitude dispersion (AD). There are no unstable models having intersecting frequencies (IF) or leaking periods (LP) in any of these eight $\mathcal{M}=1-8$ models. Models $\mathcal{M}=4$ and $\mathcal{M}=6$ give final results summarised in Table 6.

\mathcal{M}	$\mathcal{M}_{K_1, K_2, K_3, R}$	Period analysis						Fisher-test			Control file
		Data: Original non-weighted data ($n = 3012, \Delta T = 250.9$: <code>Rmonthly2000.dat</code>)						$\mathcal{M}=2$	$\mathcal{M}=3$	$\mathcal{M}=4$	
		P_1 (y)	P_2 (y)	P_3 (y)	P_4 (y)	F_R (-)	F_R (-)	F_R (-)	Q_F (-)	Q_F (-)	
(1)	η (-)	A_1 (-)	A_2 (-)	A_3 (-)	A_4 (-)						(10)
	R (-)	$t_{\min,1}$ (y)	$t_{\min,1}$ (y)	$t_{\min,1}$ (y)	$t_{\min,1}$ (y)						
(1)	(2)	(3)	(4)	(5)	(6)						
$\mathcal{M}=1$	$\mathcal{M}_{1,1,0,R}$ 4 1.09×10^7	11.0336 ± 0.0074 92.2 ± 2.8 1755.30 ± 0.12	- -	- -	- -		\uparrow 255	\uparrow 254	\uparrow 231		<code>Rmonthly2000K110R14.dat</code>
							$< 10^{-16}$	$< 10^{-16}$	$< 10^{-16}$		
$\mathcal{M}=2$	$\mathcal{M}_{2,1,0,R}$ 7 8.69×10^6	9.9998 ± 0.0060 76.7 ± 2.5 1754.18 ± 0.11	11.0200 ± 0.0074 91.6 ± 3.2 1755.65 ± 0.11	- -	- -		- -	\uparrow 179	\uparrow 174		<code>Rmonthly2000K210R14.dat</code>
								$< 10^{-16}$	$< 10^{-16}$		
$\mathcal{M}=3$	$\mathcal{M}_{3,1,0,R}$ 10 7.37×10^6	9.9848 ± 0.0076 77.0 ± 2.4 1754.36 ± 0.12	11.0293 ± 0.0065 99.6 ± 2.9 1755.704 ± 0.089	11.845 ± 0.012 60.8 ± 1.8 1760.24 ± 0.16	- -		- -	- -	\uparrow 144		<code>Rmonthly2000K310R14.dat</code>
$\mathcal{M}=4$	$\mathcal{M}_{4,1,0,R}$ 13 6.44×10^6	9.9842 ± 0.0075 77.4 ± 2.2 1754.363 ± 0.096	11.0324 ± 0.0048 98.8 ± 2.6 1755.661 ± 0.075	11.846 ± 0.012 60.0 ± 2.2 1760.22 ± 0.16	96.2 ± 1.0 50.1 ± 2.8 1815.3 ± 1.0	- -	- -	- -	-		<code>Rmonthly2000K410R14.dat</code>
Data: Non-weighted residuals of model $\mathcal{M}=4$ ($n = 3012, \Delta T = 250.9$: <code>Rmonthly2000K410R14Residuals.dat</code>)											
								$\mathcal{M}=6$	$\mathcal{M}=7$	$\mathcal{M}=8$	
$\mathcal{M}=5$	$\mathcal{M}_{1,1,-1,R}$ 3 5.67×10^6	10.547 ± 0.012 45.3 ± 1.8 1753.04 ± 0.16	- -	- -	- -		\uparrow 97	\uparrow 92	\uparrow 96		<code>Rmonthly2000K11-1R58.dat</code>
							$< 10^{-16}$	$< 10^{-16}$	$< 10^{-16}$		
$\mathcal{M}=6$	$\mathcal{M}_{2,1,-1,R}$ 6 5.17×10^6	8.1054 ± 0.0084 36.5 ± 1.7 1751.33 ± 0.13	10.541 ± 0.014 45.0 ± 1.8 1753.13 ± 0.20	- -	- -		- -	\uparrow 79	\uparrow 87		<code>Rmonthly2000K21-1R58.dat</code>
								$< 10^{-16}$	$< 10^{-16}$		
$\mathcal{M}=7$	$\mathcal{M}_{3,1,-1,R}$ 9 4.79×10^6	8.174 ± 0.033 40 ± 57 AD 1750.23 ± 0.58	8.381 ± 0.029 40 ± 57 AD 1750.67 ± 0.53	105.409 ± 0.010 45.6 ± 1.4 1753.13 ± 0.13	- -		- -	- -	\uparrow 89		<code>Rmonthly2000K31-1R58.dat</code>
$\mathcal{M}=8$	$\mathcal{M}_{4,1,-1,R}$ 12 4.40×10^6	8.175 ± 0.026 39 ± 25 AD 1750.22 ± 0.52	8.384 ± 0.032 39 ± 24 AD 1750.64 ± 0.39	10.543 ± 0.010 45.7 ± 2.1 1753.11 ± 0.13	52.08 ± 0.36 31.6 ± 2.1 1760.2 ± 1.0	- -	- -	- -	-		<code>Rmonthly2000K41-1R58.dat</code>

Table 18. Rmonthly analysis for pure sines ($K_2 = 1$). Otherwise as in Table 17.

\mathcal{M}	$\mathcal{M}_{K_1, K_2, K_3, R}$	Data: Non-weighted original data ($n = 3287, \Delta T = 273.8$: Rmonthly.dat)						Fisher-test			Control file		
		Period analysis						$\mathcal{M}=2$	$\mathcal{M}=3$	$\mathcal{M}=4$			
		P_1 (y)	P_2 (y)	P_3 (y)	P_4 (y)	A_1 (-)	A_2 (-)	A_3 (-)	A_4 (-)	F_R (-)	F_R (-)	F_R (-)	
(1)	η (-)	R (-)	$t_{\min,1}$ (y)	$t_{\min,1}$ (y)	$t_{\min,1}$ (y)	$t_{\min,1}$ (y)	$t_{\min,1}$ (y)	$t_{\min,1}$ (y)	$t_{\min,1}$ (y)	(7)	(8)	(9)	(10)
$\mathcal{M}=1$	$\mathcal{M}_{1,1,0,R}$	11.0046 ± 0.0076	-	-	-	-	-	-	-	\uparrow	\uparrow	\uparrow	RmonthlyK110R14.dat
	4	93.8 ± 2.3	-	-	-	-	-	-	-	217	243	237	
	1.14×10^7	1755.59 ± 0.11	-	-	-	-	-	-	-	$< 10^{-16}$	$< 10^{-16}$	$< 10^{-16}$	
$\mathcal{M}=2$	$\mathcal{M}_{2,1,0,R}$	10.618 ± 0.010	11.01254 ± 0.0067	-	-	-	-	-	-	\uparrow	\uparrow	\uparrow	RmonthlyK210R14.dat
	7	69.2 ± 2.9	94.0 ± 2.4	-	-	-	-	-	-	224	206		
	9.51×10^6	1752.09 ± 0.14	1755.363 ± 0.084	-	-	-	-	-	-	$< 10^{-16}$	$< 10^{-16}$		
$\mathcal{M}=3$	$\mathcal{M}_{3,1,0,R}$	10.0009 ± 0.0051	10.9954 ± 0.0075	11.780 ± 0.012	-	-	-	-	-	-	\uparrow		RmonthlyK310R14.dat
	10	74.6 ± 3.2	102.0 ± 2.6	61.6 ± 2.8	-	-	-	-	-	-	156		
	7.89×10^6	1754.302 ± 0.095	1756.046 ± 0.086	1760.67 ± 0.16	-	-	-	-	-	-	$< 10^{-16}$		
$\mathcal{M}=4$	$\mathcal{M}_{4,1,0,R}$	10.0001 ± 0.0081	10.569 ± 0.020	11.0033 ± 0.0064	11.807 ± 0.012	-	-	-	-	-	-	-	RmonthlyK410R14.dat
	13	65.5 ± 2.1	51.0 ± 1.8	101.5 ± 2.5	56.4 ± 2.4	-	-	-	-	-	-	-	
	6.90×10^6	1754.16 ± 0.11	1753.03 ± 0.27	1755.897 ± 0.076	1760.33 ± 0.13	-	-	-	-	-	-	-	
Data: Non-weighted residuals of model $\mathcal{M}=4$ ($n = 3287, \Delta T = 273.8$: RmonthlyK410R14Residuals.dat)													
								$\mathcal{M}=6$	$\mathcal{M}=7$	$\mathcal{M}=8$			
$\mathcal{M}=5$	$\mathcal{M}_{1,1,-1,R}$	98.6 ± 1.1	-	-	-	-	-	\uparrow	\uparrow	\uparrow			
	3	49.5 ± 2.3	-	-	-	-	-	93	103	106	RmonthlyK11-1R58.dat		
	5.84×10^6	1814.2 ± 1.5	-	-	-	-	-	$< 10^{-16}$	$< 10^{-16}$	$< 10^{-16}$			
$\mathcal{M}=6$	$\mathcal{M}_{2,1,-1,R}$	52.67 ± 0.29	99.68 ± 0.89	-	-	-	-	-	\uparrow	\uparrow		RmonthlyK21-1R58.dat	
	6	34.0 ± 2.2	51.5 ± 2.0	-	-	-	-	-	104	104			
	5.38×10^6	1759.52 ± 0.87	1812.24 ± 0.75	-	-	-	-	-	$< 10^{-16}$	$< 10^{-16}$			
$\mathcal{M}=7$	$\mathcal{M}_{3,1,-1,R}$	8.1087 ± 0.0076	52.66 ± 0.27	99.92 ± 0.57	-	-	-	-	-	\uparrow		RmonthlyK31-1R58.dat	
	9	33.6 ± 1.6	33.9 ± 2.0	51.8 ± 2.3	-	-	-	-	-	94			
	4.91×10^6	1751.29 ± 0.14	1759.6 ± 0.70	1811.99 ± 0.84	-	-	-	-	-	$< 10^{-16}$			
$\mathcal{M}=8$	$\mathcal{M}_{4,1,-1,R}$	8.456 ± 0.0086	59.6 ± 1.2 IF	60.8 ± 1.2 IF	103.10 ± 0.67	-	-	-	-	-	-	RmonthlyK41-1R58.dat	
UM	12	32.4 ± 2.6	274 ± 01 AD	274 ± 02 AD	54.4 ± 1.9	-	-	-	-	-	-		
	4.52×10^6	1749.51 ± 0.14	1801.1 ± 2.5	1768.4 ± 3.1	1807.29 ± 0.94	-	-	-	-	-	-		

Table 19. Rmonthly2000 analysis for double waves ($K_2 = 2$). Otherwise as in Table 17.

\mathcal{M}	$\mathcal{M}_{K_1, K_2, K_3, R}$	Period analysis						Fisher-test			Control file	
		Data: Non-weighted original data ($n = 3012, \Delta T = 250.9$: Rmonthly2000.dat)						$\mathcal{M}=2$	$\mathcal{M}=3$	$\mathcal{M}=4$		
		P_1 (y)	P_2 (y)	P_3 (y)	P_4 (y)	A_1 (-)	A_2 (-)	A_3 (-)	A_4 (-)	F_R (-)	Q_F (-)	F_R (-)
(1)	(2)	(3)	(4)	(5)	(6)	(7)	(8)	(9)	(10)			
$\mathcal{M}=1$	$\mathcal{M}_{1,2,0,R}$	11.0242 ± 0.0084	-	-	-	-	-	-	\uparrow	\uparrow	\uparrow	
	6	94.7 ± 3.6	-	-	-	-	-	-	154	149	164	Rmonthly2000K120R14.dat
	1.08×10^7	1755.98 ± 0.12	-	-	-	-	-	-	$< 10^{-16}$	$< 10^{-16}$	$< 10^{-16}$	
$\mathcal{M}=2$	$\mathcal{M}_{2,2,0,R}$	11.0118 ± 0.0071	20.000 ± 0.016	-	-	-	-	-	\uparrow	\uparrow		
	11	95.0 ± 2.8	81.2 ± 2.4	-	-	-	-	-	115	135		Rmonthly2000K220R14.dat
	8.59×10^6	1756.33 ± 0.15	1764.12 ± 0.11	-	-	-	-	-	$< 10^{-16}$	$< 10^{-16}$		
$\mathcal{M}=3$	$\mathcal{M}_{3,2,0,R}$	9.9862 ± 0.0068	11.0222 ± 0.0062	23.692 ± 0.021	-	-	-	-	-	-	\uparrow	
	16	78.7 ± 1.8	103.3 ± 2.9	69.1 ± 2.4	-	-	-	-	-	-	130	Rmonthly2000K320R14.dat
	7.21×10^6	1754.72 ± 0.18	1756.33 ± 0.12	1760.11 ± 0.13	-	-	-	-	-	-	$< 10^{-16}$	
$\mathcal{M}=4$	$\mathcal{M}_{4,2,0,R}$	9.9882 ± 0.0061	11.0234 ± 0.0068	23.686 ± 0.018	104.16 ± 0.59	-	-	-	-	-	-	
	21	78.6 ± 2.6	102.9 ± 2.7	69.4 ± 2.7	70.4 ± 3.6	-	-	-	-	-	-	Rmonthly2000K420R14.dat
	5.92×10^6	1754.70 ± 0.11	1756.295 ± 0.099	1760.13 ± 0.14	1811.43 ± 0.54	-	-	-	-	-	-	
Data: Non-weighted residuals of $\mathcal{M}=4$ ($n = 3012, \Delta T = 250.9$: Rmonthly2000K420R14Residuals.dat)												
								$\mathcal{M}=6$	$\mathcal{M}=7$	$\mathcal{M}=8$		
$\mathcal{M}=5$	$\mathcal{M}_{1,2,-1,R}$	10.5400 ± 0.0095	-	-	-	-	-	\uparrow	\uparrow	\uparrow		
	5	51.1 ± 2.6	-	-	-	-	-	68	69	74		
	5.04×10^6	1754.34 ± 0.19	-	-	-	-	-	$< 10^{-16}$	$< 10^{-16}$	$< 10^{-16}$	Rmonthly2000K12-1R58.dat	
$\mathcal{M}=6$	$\mathcal{M}_{2,2,-1,R}$	10.5386 ± 0.0076	16.215 ± 0.014	-	-	-	-	-	\uparrow	\uparrow		
	10	51.5 ± 2.6	41.6 ± 3.0	-	-	-	-	-	63	70		
	4.53×10^6	1754.41 ± 0.19	1751.20 ± 0.16	-	-	-	-	-	$< 10^{-16}$	$< 10^{-16}$	Rmonthly2000K22-1R58.dat	
$\mathcal{M}=7$	$\mathcal{M}_{3,2,-1,R}$	8.177 ± 0.010	10.5400 ± 0.0071	16.764 ± 0.033	-	-	-	-	-	\uparrow		
	15	39.6 ± 4.0	51.7 ± 2.2	46.0 ± 4.4	-	-	-	-	-	70		
	4.10×10^6	1750.46 ± 0.60	1754.35 ± 0.10	1759.23 ± 0.26	-	-	-	-	-	$< 10^{-16}$	Rmonthly2000K32-1R58.dat	
$\mathcal{M}=8$	$\mathcal{M}_{4,2,-1,R}$	8.173 ± 0.011	10.5372 ± 0.0075	16.781 ± 0.034	136.43 ± 0.99	-	-	-	-	-		
	20	37.6 ± 4.8	51.2 ± 1.8	44.9 ± 4.0	42.3 ± 2.2	-	-	-	-	-		
	3.67×10^6	1750.76 ± 0.64	1754.38 ± 0.12	1759.13 ± 0.25	1884.10 ± 0.91	-	-	-	-	-	Rmonthly2000K42-1R58.dat	

Table 20. Rmonthly analysis for double waves ($K_2 = 2$). Otherwise as in Table 17.

Data: Original non-weighted data ($n = 3287, \Delta T = 273.8$: Rmonthly.dat)									
\mathcal{M}	$\mathcal{M}_{K_1, K_2, K_3, R}$	Period analysis				Fisher-test			Control file
		P_1 (y)	P_2 (y)	P_3 (y)	P_4 (y)	$\mathcal{M}=2$	$\mathcal{M}=3$	$\mathcal{M}=4$	
		A_1 (-)	A_2 (-)	A_3 (-)	A_4 (-)	F_R (-)	F_R (-)	F_R (-)	
(1)	R (-)	$t_{\min,1}$ (y)	$t_{\min,1}$ (y)	$t_{\min,1}$ (y)	$t_{\min,1}$ (y)	Q_F (-)	Q_F (-)	Q_F (-)	(10)
		(2)	(3)	(4)	(5)	(6)	(7)	(8)	
		6	97.5 ± 2.8	-	-	157	155	177	
$\mathcal{M}=1$	$\mathcal{M}_{1,2,0,R}$	10.9922 ± 0.0064	-	-	-	$< 10^{-16}$	$< 10^{-16}$	$< 10^{-16}$	RmonthlyK120R14.dat
	6	97.5 ± 2.8	-	-	-				
	1.14×10^7	1756.41 ± 0.18	-	-	-				
$\mathcal{M}=2$	$\mathcal{M}_{2,2,0,R}$	10.9964 ± 0.0090	21.252 ± 0.023	-	-	-	\uparrow	\uparrow	RmonthlyK220R14.dat
	11	97.4 ± 3.3	82.8 ± 2.8	-	-	-	123	151	
	9.20×10^6	1756.13 ± 0.18	1752.36 ± 0.14	-	-	-	$< 10^{-16}$	$< 10^{-16}$	
$\mathcal{M}=3$	$\mathcal{M}_{3,2,0,R}$	10.9864 ± 0.0052	11.772 ± 0.010	19.998 ± 0.012	-	-	-	\uparrow	RmonthlyK320R14.dat
	16	106.4 ± 2.7	64.2 ± 2.3	76.1 ± 3.1	-	-	-	150	
	7.74×10^6	1756.72 ± 0.11	1749.48 ± 0.18	1754.36 ± 0.11	-	-	-	$< 10^{-16}$	
$\mathcal{M}=4$	$\mathcal{M}_{4,2,0,R}$	10.9878 ± 0.0051	11.770 ± 0.011	20.0062 ± 0.0088	104.23 ± 0.68	-	-	-	RmonthlyK420R14.dat
	21	104.6 ± 2.3	62.7 ± 2.6	75.2 ± 2.7	68.1 ± 2.7	-	-	-	
	6.29×10^6	1756.678 ± 0.077	1749.51 ± 0.15	1754.284 ± 0.063	1811.37 ± 0.68	-	-	-	
Data: Non-weighted residuals of model $\mathcal{M}=4$ ($n = 3287, \Delta T = 273.8$: RmonthlyK420R14Residuals.dat)									
						$\mathcal{M}=6$	$\mathcal{M}=7$	$\mathcal{M}=8$	
$\mathcal{M}=5$	$\mathcal{M}_{1,2,-1,R}$	10.5486 ± 0.0078	-	-	-	\uparrow	\uparrow	\uparrow	RmonthlyK12-1R58.dat
	5	53.6 ± 2.6	-	-	-	70	66	65	
	5.26×10^6	1754.38 ± 0.13	-	-	-	$< 10^{-16}$	$< 10^{-16}$	$< 10^{-16}$	
$\mathcal{M}=6$	$\mathcal{M}_{2,2,-1,R}$	10.5421 ± 0.0072	16.220 ± 0.011	-	-	-	\uparrow	\uparrow	RmonthlyK22-1R58.dat
	10	54.3 ± 2.1	41.0 ± 1.8	-	-	-	55	56	
	4.75×10^6	1754.44 ± 0.14	1751.167 ± 0.099	-	-	-	$< 10^{-16}$	$< 10^{-16}$	
$\mathcal{M}=7$	$\mathcal{M}_{3,2,-1,R}$	10.5376 ± 0.0063	16.217 ± 0.013	142.9 ± 1.4	-	-	-	\uparrow	RmonthlyK32-1R58.dat
	15	54.2 ± 1.8	40.9 ± 2.3	37.5 ± 2.4	-	-	-	53	
	4.38×10^6	1754.50 ± 0.13	1751.17 ± 0.14	1887.63 ± 0.73	-	-	-	$< 10^{-16}$	
$\mathcal{M}=8$	$\mathcal{M}_{4,2,-1,R}$	8.169 ± 0.014	10.5407 ± 0.0060	16.753 ± 0.027	143.39 ± 0.99	-	-	-	RmonthlyK42-1R58.dat
	20	35.5 ± 3.3	55.6 ± 2.3	41.2 ± 3.1	37.3 ± 2.7	-	-	-	
	4.05×10^6	1750.90 ± 0.51	1754.40 ± 0.13	1759.19 ± 0.23	1887.84 ± 0.80	-	-	-	

Table 21. Cmonthly2000 analysis for pure sines ($K_2 = 1$). Otherwise as in Table 17.

\mathcal{M}	$\mathcal{M}_{K_1, K_2, K_3, \chi^2}$	Period analysis						Fisher-test			Control file		
		Data: Weighted original data before 2000 ($n = 2182, \Delta T = 181.9$: Cmonthly2000.dat)						$\mathcal{M}=2$	$\mathcal{M}=3$	$\mathcal{M}=4$			
		P_1 (y)	P_2 (y)	P_3 (y)	P_4 (y)	A_1 (-)	A_2 (-)	A_3 (-)	A_4 (-)	F_R (-)	F_R (-)	F_R (-)	
(1)	(2)	$t_{\min,1}$ (y)	$t_{\min,1}$ (y)	$t_{\min,1}$ (y)	$t_{\min,1}$ (y)	(3)	(4)	(5)	(6)	(7)	(8)	(9)	(10)
$\mathcal{M}=1$	$\mathcal{M}_{1,1,0,\chi^2}$	10.8338 ± 0.0094	-	-	-	-	-	-	-	\uparrow	\uparrow	\uparrow	Cmonthly2000K110R14.dat
	4	121.9 ± 3.6	-	-	-	-	-	-	-	203	230	196	
	3.34×10^6	1823.740 ± 0.082	-	-	-	-	-	-	-	$< 10^{-16}$	$< 10^{-16}$	$< 10^{-16}$	
$\mathcal{M}=2$	$\mathcal{M}_{2,1,0,\chi^2}$	10.196 ± 0.027	10.805 ± 0.013	-	-	-	-	-	-	\uparrow	\uparrow		
	7	61.9 ± 3.9	118.2 ± 3.7	-	-	-	-	-	-	202	151		Cmonthly2000K210R14.dat
	2.61×10^6	1822.12 ± 0.23	1823.941 ± 0.091	-	-	-	-	-	-	$< 10^{-16}$	$< 10^{-16}$		
$\mathcal{M}=3$	$\mathcal{M}_{3,1,0,\chi^2}$	10.265 ± 0.026	10.766 ± 0.017	267 ± 34 LP	-	-	-	-	-	-	\uparrow		
UM	10	71.0 ± 3.2	118.2 ± 3.8	54.6 ± 4.9	-	-	-	-	-	-	78		Cmonthly2000K310R14.dat
	2.04×10^6	1821.51 ± 0.17	1824.19 ± 0.13	1868.3 ± 4.5	-	-	-	-	-	-	$< 10^{-16}$		
$\mathcal{M}=4$	$\mathcal{M}_{4,1,0,\chi^2}$	10.236 ± 0.020	10.770 ± 0.010	99.6 ± 6.2	8400 ± 3800 LP	-	-	-	-	-	-		
UM	13	69.0 ± 2.8	119.2 ± 4.0	34.8 ± 4.0	19000 ± 8800 AD	-	-	-	-	-	-		Cmonthly2000K410R14.dat
	1.84×10^6	1821.83 ± 0.17	1824.192 ± 0.079	1903.2 ± 1.8	1843 ± 24	-	-	-	-	-	-		

Table 22. Cmonthly analysis for pure sines ($K_2 = 1$). Otherwise as in Table 17.

\mathcal{M}	$\mathcal{M}_{K_1, K_2, K_3, \chi^2}$	Period analysis								Control file	
		Data: Weighted original data ($n = 2458, \Delta T = 204.8$: Cmonthly.dat)									
		P_1 (y)	P_2 (y)	P_3 (y)	P_4 (y)	$\mathcal{M}=2$	$\mathcal{M}=3$	$\mathcal{M}=4$	$\mathcal{M}=5$		
(1)	η (-)	A_1 (-)	A_2 (-)	A_3 (-)	A_4 (-)	F_R (-)	F_R (-)	F_R (-)	F_R (-)		
	χ^2 (-)	$t_{\min,1}$ (y)	$t_{\min,1}$ (y)	$t_{\min,1}$ (y)	$t_{\min,1}$ (y)	Q_F (-)	Q_F (-)	Q_F (-)	Q_F (-)		
	(2)	(3)	(4)	(5)	(6)	(7)	(8)	(9)	(10)		
$\mathcal{M}=1$	$\mathcal{M}_{1,1,0,\chi^2}$	10.8350 ± 0.0089	-	-	-	\uparrow	\uparrow	\uparrow			
	4	121.6 ± 2.9	-	-	-	173	197	210			
	3.71×10^6	1823.730 ± 0.088	-	-	-	$< 10^{-16}$	$< 10^{-16}$	$< 10^{-16}$		CmonthlyK110R14.dat	
$\mathcal{M}=2$	$\mathcal{M}_{2,1,0,\chi^2}$	10.149 ± 0.012	10.8549 ± 0.0078	-	-	-	\uparrow	\uparrow			
	7	53.8 ± 2.5	120.1 ± 2.5	-	-	-	183	189			
	3.06×10^6	1822.40 ± 0.16	1823.63 ± 0.10	-	-	-	$< 10^{-16}$	$< 10^{-16}$		CmonthlyK210R14.dat	
$\mathcal{M}=3$	$\mathcal{M}_{3,1,0,\chi^2}$	10.113 ± 0.010	10.8612 ± 0.0083	120.8 ± 1.7	-	-	-	\uparrow			
	10	58.1 ± 3.1	122.6 ± 2.0	51.1 ± 2.8	-	-	-	160			
	2.50×10^6	1822.91 ± 0.13	1823.516 ± 0.086	1908.0 ± 1.1	-	-	-	$< 10^{-16}$		CmonthlyK310R14.dat	
$\mathcal{M}=4$	$\mathcal{M}_{4,1,0,\chi^2}$	10.0658 ± 0.0077	10.8585 ± 0.0048	11.863 ± 0.021	116.7 ± 1.3	-	-	-			
	13	59.3 ± 2.8	117.5 ± 2.9	43.3 ± 2.0	52.9 ± 2.5	-	-	-			
	2.09×10^6	1823.52 ± 0.12	1823.580 ± 0.053	1818.92 ± 0.20	1911.02 ± 0.74	-	-	-		CmonthlyK410R14.dat	
Data: Non-weighted residuals of $\mathcal{M}=4$ ($n = 2458, \Delta T = 204.8$: CmonthlyK410R14Residuals.dat)											
						$\mathcal{M}=6$	$\mathcal{M}=7$	$\mathcal{M}=8$			
$\mathcal{M}=5$	$\mathcal{M}_{1,1,-1,\chi^2}$	8.009 ± 0.017	-	-	-	\uparrow	\uparrow	\uparrow			
	3	25.6 ± 2.5	-	-	-	64	55	54			
	1.93×10^6	1818.07 ± 0.24	-	-	-	$< 10^{-16}$	$< 10^{-16}$	$< 10^{-16}$		CmonthlyK11-1R58.dat	
$\mathcal{M}=6$	$\mathcal{M}_{2,1,-1,\chi^2}$	8.008 ± 0.014	239 ± 22 LP	-	-	-	\uparrow	\uparrow			
UM	6	25.0 ± 1.9	24.7 ± 2.3	-	-	-	43	46			
	1.79×10^6	1818.07 ± 0.20	1841 ± 11	-	-	-	$< 10^{-16}$	$< 10^{-16}$		CmonthlyK21-1R58.dat	
$\mathcal{M}=7$	$\mathcal{M}_{3,1,-1,\chi^2}$	5.4184 ± 0.0064	8.005 ± 0.018	239 ± 23 LP	-	-	-	\uparrow			
UM	9	20.3 ± 2.3	24.7 ± 2.0	25.4 ± 1.5	-	-	-	46			
	1.70×10^6	1819.89 ± 0.14	1818.10 ± 0.30	1841 ± 10	-	-	-	$< 10^{-16}$		CmonthlyK31-1R58.dat	
$\mathcal{M}=8$	$\mathcal{M}_{4,1,-1,\chi^2}$	5.4187 ± 0.0075	8.002 ± 0.015	38.72 ± 0.58	250 ± 28 LP	-	-	-			
UM	12	20.0 ± 1.8	25.7 ± 2.2	19.5 ± 1.7	24.5 ± 2.0	-	-	-			
	1.61×10^6	1819.88 ± 0.18	1818.16 ± 0.26	1856.2 ± 1.2	1840 ± 12	-	-	-		CmonthlyK41-1R58.dat	

Table 23. Cmonthly2000 analysis for double waves ($K_2 = 2$). Otherwise as in Table 17.

\mathcal{M}	$\mathcal{M}_{K_1, K_2, K_3, \chi^2}$	Period analysis						Fisher-test			Control file		
		Data: Weighted original data before 2000 ($n = 2182, \Delta T = 181.9$: Cmonthly2000.dat)						$\mathcal{M}=2$	$\mathcal{M}=3$	$\mathcal{M}=4$			
		P_1 (y)	P_2 (y)	P_3 (y)	P_4 (y)	A_1 (-)	A_2 (-)	A_3 (-)	A_4 (-)	F_R (-)	F_R (-)	F_R (-)	
(1)	(2)	$t_{\min,1}$ (y)	$t_{\min,1}$ (y)	$t_{\min,1}$ (y)	$t_{\min,1}$ (y)	(3)	(4)	(5)	(6)	(7)	(8)	(9)	(10)
$\mathcal{M}=1$	$\mathcal{M}_{1,2,0,\chi^2}$	10.830 ± 0.010	-	-	-	-	-	-	-	\uparrow	\uparrow	\uparrow	Cmonthly2000K120R14.dat
	6	126.1 ± 4.2	-	-	-	-	-	-	-	125	180	160	
	3.30×10^6	1824.17 ± 0.12	-	-	-	-	-	-	-	$< 10^{-16}$	$< 10^{-16}$	$< 10^{-16}$	
$\mathcal{M}=2$	$\mathcal{M}_{2,2,0,\chi^2}$	10.196 ± 0.017	10.807 ± 0.012	-	-	-	-	-	-	\uparrow	\uparrow	\uparrow	Cmonthly2000K220R14.dat
	11	62.1 ± 3.7	123.5 ± 3.0	-	-	-	-	-	-	183	138		
	2.56×10^6	1822.31 ± 0.17	1824.34 ± 0.10	-	-	-	-	-	-	$< 10^{-16}$	$< 10^{-16}$		
$\mathcal{M}=3$	$\mathcal{M}_{3,2,0,\chi^2}$	10.240 ± 0.017	10.766 ± 0.012	368 ± 1730 LP	-	-	-	-	-	-	\uparrow		
UM	16	67.5 ± 3.2	123.7 ± 2.8	$330 \pm 1.9 \times 10^7$ AD	-	-	-	-	-	-	66	Cmonthly2000K320R14.dat	
	1.80×10^6	1821.92 ± 0.26	1824.63 ± 0.17	2097 ± 92	-	-	-	-	-	-	$< 10^{-16}$		
$\mathcal{M}=4$	$\mathcal{M}_{4,2,0,\chi^2}$	12.01 ± 0.76	20.23 ± 0.54 IF	21.59 ± 0.98 IF	2222 ± 823 LP	-	-	-	-	-	-		
UM	21	39.1 ± 9.2	71 ± 21 AD	130 ± 37 AD	$6 \times 10^5 \pm 3 \times 10^5$ AD	-	-	-	-	-	-	Cmonthly2000K420R14.dat	
	1.56×10^6	1818.4 ± 1.8	1833.22 ± 0.77	1835.2 ± 02.2	3025 ± 191	-	-	-	-	-	-		

Table 24. `Cmonthly` analysis for double waves ($K_2 = 2$). Otherwise as in Table 17.

\mathcal{M}	$\mathcal{M}_{K_1, K_2, K_3, \chi^2}$	Period analysis						Fisher-test			Control file	
		Data: Weighted original data ($n = 2458, \Delta T = 204.8$; <code>Cmonthly.dat</code>)						$\mathcal{M}=2$	$\mathcal{M}=3$	$\mathcal{M}=4$		
		P_1 (y)	P_2 (y)	P_3 (y)	P_4 (y)	A_1 (-)	A_2 (-)	A_3 (-)	A_4 (-)	F_R (-)	Q_F (-)	F_R (-)
(1)	(2)	(3)	(4)	(5)	(6)	(7)	(8)	(9)	(10)			
$\mathcal{M}=1$	$\mathcal{M}_{1,2,0,\chi^2}$	21.667 \pm 0.014	-	-	-	-	-	-	-	-	-	-
	6	132.6 \pm 3.4	-	-	-	-	-	-	140	171	170	<code>CmonthlyK120R14.dat</code>
	3.64×10^6	1823.632 \pm 0.077	-	-	-	-	-	-	$< 10^{-16}$	$< 10^{-16}$	$< 10^{-16}$	
$\mathcal{M}=2$	$\mathcal{M}_{2,2,0,\chi^2}$	10.8110 \pm 0.0092	297 \pm 68 LP	-	-	-	-	-	-	-	-	-
UM	11	125.0 \pm 4.0	152 \pm 380 AD	-	-	-	-	-	157	144	<code>CmonthlyK220R14.dat</code>	
	2.83×10^6	1824.50 \pm 0.13	2067 \pm 32	-	-	-	-	-	$< 10^{-16}$	$< 10^{-16}$	$< 10^{-16}$	
$\mathcal{M}=3$	$\mathcal{M}_{3,2,0,\chi^2}$	10.136 \pm 0.0012	21.6733 \pm 0.0091	323 \pm 44 LP	-	-	-	-	-	-	-	-
UM	16	57.4 \pm 2.6	128.7 \pm 4.0	192 \pm 157 AD	-	-	-	-	-	-	98	<code>CmonthlyK320R14.dat</code>
	2.14×10^6	1822.74 \pm 0.24	1834.774 \pm 0.065	2075 \pm 21	-	-	-	-	-	-	$< 10^{-16}$	
$\mathcal{M}=4$	$\mathcal{M}_{4,2,0,\chi^2}$	20.165 \pm 0.019	21.648 \pm 0.093	23.895 \pm 0.037	322 \pm 59 LP	-	-	-	-	-	-	-
UM	21	62.4 \pm 2.6	129.9 \pm 2.9	45.0 \pm 3.0	214 \pm 392 AD	-	-	-	-	-	-	<code>CmonthlyK420R14.dat</code>
	1.78×10^6	1833.39 \pm 0.11	1834.949 \pm 0.067	1841.86 \pm 0.17	2078 \pm 29	-	-	-	-	-	-	

Table 25. Ryearly2000 analysis for pure sines ($K_2 = 1$). Otherwise as in Table 17

\mathcal{M}	$\mathcal{M}_{K_1, K_2, K_3, R}$	Period analysis						Fisher-test			Control file
		Data: Non-weighted original data ($n = 300, \Delta T = 299$: Ryearly2000.dat)						$\mathcal{M}=2$	$\mathcal{M}=3$	$\mathcal{M}=4$	
		P_1 (y)	P_2 (y)	P_3 (y)	P_4 (y)	A_4 (-)	F_R (-)	F_R (-)	F_R (-)	Q_F (-)	
η (-)	A_1 (-)	A_2 (-)	A_3 (-)	A_4 (-)	F_R (-)	Q_F (-)	Q_F (-)	Q_F (-)	Q_F (-)		
R (-)	$t_{\min,1}$ (y)	$t_{\min,1}$ (y)	$t_{\min,1}$ (y)	$t_{\min,1}$ (y)	$t_{\min,1}$ (y)	F_R (-)	Q_F (-)	Q_F (-)	Q_F (-)		
(1)	(2)	(3)	(4)	(5)	(6)	(7)	(8)	(9)	(10)		
$\mathcal{M}=1$	$\mathcal{M}_{1,1,0,R}$	11.018 ± 0.018	-	-	-	-	\uparrow	\uparrow	\uparrow		
	4	94.7 ± 7.9	-	-	-	-	28	24	26		
	8.26×10^5	1711.46 ± 0.24	-	-	-	-	6.7×10^{-16}	$< 10^{-16}$	$< 10^{-16}$	Ryearly2000K110R14.dat	
$\mathcal{M}=2$	$\mathcal{M}_{2,1,0,R}$	10.001 ± 0.021	11.046 ± 0.020	-	-	-	\uparrow	\uparrow	\uparrow		
	7	71.2 ± 9.2	90.2 ± 5.2	-	-	-	-	15	20		
	6.42×10^5	1704.15 ± 0.34	1711.08 ± 0.31	-	-	-	-	2.9×10^{-9}	$< 10^{-16}$		
$\mathcal{M}=3$	$\mathcal{M}_{3,1,0,R}$	9.982 ± 0.020	10.624 ± 0.029	10.999 ± 0.018	-	-	-	-	\uparrow		
	10	63.9 ± 6.1	53.3 ± 8.4	91.2 ± 6.7	-	-	-	-	22		
	5.54×10^5	1704.54 ± 0.29	1709.62 ± 0.48	1700.71 ± 0.25	-	-	-	-	9.8×10^{-13}	Ryearly2000K310R14.dat	
$\mathcal{M}=4$	$\mathcal{M}_{4,1,0,R}$	9.980 ± 0.016	10.620 ± 0.033	11.006 ± 0.017	100.3 ± 2.1	-	-	-	-		
	13	64.6 ± 7.6	52.4 ± 8.5	90.4 ± 4.7	52.4 ± 6.3	-	-	-	-		
	4.51×10^5	1704.59 ± 0.26	1709.60 ± 0.41	1700.62 ± 0.26	1711.5 ± 3.1	-	-	-	-		
Data: Non-weighted residuals of $\mathcal{M}=4$ ($n = 300, \Delta T = 299$: Ryearly2000K410R14Residuals.dat)											
							$\mathcal{M}=6$	$\mathcal{M}=7$	$\mathcal{M}=8$		
$\mathcal{M}=5$	$\mathcal{M}_{1,1,-1,R}$	11.845 ± 0.039	-	-	-	-	\uparrow	\uparrow	\uparrow		
	3	42.1 ± 5.2	-	-	-	-	14	14	14		
	3.84×10^5	1700.78 ± 0.54	-	-	-	-	1.6×10^{-8}	2.4×10^{-14}	$< 10^{-16}$	Ryearly2000K11-1R58.dat	
$\mathcal{M}=6$	$\mathcal{M}_{2,1,-1,R}$	11.854 ± 0.034	52.98 ± 0.69	-	-	-	\uparrow	\uparrow	\uparrow		
	6	42.5 ± 5.5	35.6 ± 4.6	-	-	-	-	13	13		
	3.36×10^5	1700.64 ± 0.53	1705.4 ± 2.0	-	-	-	-	5.0×10^{-8}	7.8×10^{-13}	Ryearly2000K21-1R58.dat	
$\mathcal{M}=7$	$\mathcal{M}_{3,1,-1,R}$	8.459 ± 0.017	11.860 ± 0.032	52.98 ± 0.67	-	-	-	-	\uparrow		
	9	32.9 ± 4.3	42.7 ± 5.3	35.6 ± 4.8	-	-	-	-	11		
	2.96×10^5	1707.15 ± 0.45	1700.58 ± 0.46	1705.4 ± 2.3	-	-	-	-	5.7×10^{-7}	Ryearly2000K31-1R58.dat	
$\mathcal{M}=8$	$\mathcal{M}_{4,1,-1,R}$	8.460 ± 0.027	11.862 ± 0.034	53.24 ± 0.78	65.4 ± 1.3	-	-	-	-		
	12	33.0 ± 4.4	42.6 ± 4.1	35.3 ± 6.3	29.0 ± 4.7	-	-	-	-		
	2.65×10^5	1707.15 ± 0.40	1700.54 ± 0.46	1705.0 ± 2.7	1754.3 ± 2.5	-	-	-	-		

Table 26. Ryearly analysis for pure sines ($K_2 = 1$). Otherwise as in Table 17.

\mathcal{M}	$\mathcal{M}_{K_1, K_2, K_3, R}$	Period analysis						Fisher-test			Control file
		Data: Non-weighted original data ($n = 322, \Delta T = 321$: Ryearly.dat)						$\mathcal{M}=2$	$\mathcal{M}=3$	$\mathcal{M}=4$	
		P_1 (y)	P_2 (y)	P_3 (y)	P_4 (y)	A_4 (-)	F_R (-)	F_R (-)	F_R (-)	Q_F (-)	
η (-)	A_1 (-)	A_2 (-)	A_3 (-)	A_4 (-)	F_R (-)	Q_F (-)	Q_F (-)	Q_F (-)	Q_F (-)	Q_F (-)	
R (-)	$t_{\min,1}$ (y)	$t_{\min,1}$ (y)	$t_{\min,1}$ (y)	$t_{\min,1}$ (y)	$t_{\min,1}$ (y)	Q_F (-)	Q_F (-)	Q_F (-)	Q_F (-)	Q_F (-)	
(1)	(2)	(3)	(4)	(5)	(6)	(7)	(8)	(9)	(10)		
$\mathcal{M}=1$	$\mathcal{M}_{1,1,0,R}$	11.003 ± 0.017	-	-	-	-	\uparrow	\uparrow	\uparrow		
	4	95.9 ± 7.4	-	-	-	-	26	26	29		
	8.65×10^5	1700.60 ± 0.31	-	-	-	-	6.1×10^{-15}	$< 10^{-16}$	$< 10^{-16}$		RyearlyK110R14.dat
$\mathcal{M}=2$	$\mathcal{M}_{2,1,0,R}$	10.018 ± 0.018	11.024 ± 0.011	-	-	-	-	\uparrow	\uparrow		
	7	66.0 ± 6.4	94.1 ± 5.0	-	-	-	-	21	25		
	6.94×10^5	1703.97 ± 0.38	1711.30 ± 0.21	-	-	-	-	2.6×10^{-12}	$< 10^{-16}$		RyearlyK210R14.dat
$\mathcal{M}=3$	$\mathcal{M}_{3,1,0,R}$	9.974 ± 0.017	10.665 ± 0.032	10.973 ± 0.026	-	-	-	-	\uparrow		
	10	62.4 ± 6.2	61.8 ± 8.8	100.2 ± 9.9	-	-	-	-	24		
	5.78×10^5	1704.61 ± 0.31	1709.27 ± 0.44	1700.96 ± 0.43	-	-	-	-	3.4×10^{-14}		RyearlyK310R14.dat
$\mathcal{M}=4$	$\mathcal{M}_{4,1,0,R}$	9.975 ± 0.017	10.659 ± 0.031	10.981 ± 0.020	101.4 ± 2.4	-	-	-	-		
	13	62.8 ± 6.1	59.9 ± 8.6	98.3 ± 7.8	51.7 ± 4.9	-	-	-	-		
	4.67×10^5	1704.63 ± 0.35	1709.27 ± 0.44	1700.86 ± 0.24	1710.5 ± 3.4	-	-	-	-		RyearlyK410R14.dat
Data: Non-weighted residuals of $\mathcal{M}=4$ ($n = 322, \Delta T = 321$: RyearlyK410R14Residuals.dat)											
							$\mathcal{M}=6$	$\mathcal{M}=7$	$\mathcal{M}=8$		
$\mathcal{M}=5$	$\mathcal{M}_{1,1,-1,R}$	11.814 ± 0.034	-	-	-	-	\uparrow	\uparrow	\uparrow		
	3	41.0 ± 5.2	-	-	-	-	15	15	14		
	3.99×10^5	1701.13 ± 0.47	-	-	-	-	3.6×10^{-9}	5.1×10^{-15}	$< 10^{-16}$		RyearlyK11-1R58.dat
$\mathcal{M}=6$	$\mathcal{M}_{2,1,-1,R}$	11.826 ± 0.028	53.15 ± 0.56	-	-	-	-	\uparrow	\uparrow		
	6	40.5 ± 5.1	35.1 ± 5.2	-	-	-	-	13	12		
	3.49×10^5	1700.95 ± 0.44	1705.2 ± 2.1	-	-	-	-	4.5×10^{-8}	2.3×10^{-12}		RyearlyK21-1R58.dat
$\mathcal{M}=7$	$\mathcal{M}_{3,1,-1,R}$	8.465 ± 0.018	11.816 ± 0.033	53.19 ± 0.50	-	-	-	-	\uparrow		
	9	31.2 ± 3.6	40.8 ± 4.7	35.0 ± 5.3	-	-	-	-	10		
	3.10×10^5	1707.11 ± 0.48	1701.06 ± 0.44	1705.1 ± 1.4	-	-	-	-	1.9×10^{-6}		RyearlyK31-1R58.dat
$\mathcal{M}=8$	$\mathcal{M}_{4,1,-1,R}$	8.466 ± 0.016	11.820 ± 0.027	53.83 ± 0.76	66.7 ± 1.4	-	-	-	-		
	12	31.1 ± 4.8	40.5 ± 3.3	34.3 ± 3.6	26.7 ± 4.4	-	-	-	-		
	2.82×10^5	1707.10 ± 0.35	1701.01 ± 0.42	1704.5 ± 2.7	1753.0 ± 3.8	-	-	-	-		RyearlyK41-1R58.dat

Table 27. Cyearly2000 analysis for pure sines ($K_2 = 1$). Otherwise as in Table 17.

\mathcal{M}	$\mathcal{M}_{K_1, K_2, K_3, \chi^2}$	Period analysis						Fisher-test			Control file								
		P_1 (y)	P_2 (y)	P_3 (y)	P_4 (y)	$\mathcal{M}=2$	$\mathcal{M}=3$	$\mathcal{M}=4$											
(1)	η (-)	A_1 (-)	A_2 (-)	A_3 (-)	A_4 (-)	F_R (-)	F_R (-)	F_R (-)	(2)	(3)	(4)	(5)	(6)	(7)	(8)	(9)	(10)		
$\mathcal{M}=1$	$\mathcal{M}_{1,1,0,\chi^2}$	10.835 ± 0.030	-	-	-	-	-	-	4	123.5 ± 8.7	1823.75 ± 0.31	$t_{\min,1}$ (y)	$t_{\min,1}$ (y)	$t_{\min,1}$ (y)	$t_{\min,1}$ (y)	7.4×10^{-12}	$< 10^{-16}$	$< 10^{-16}$	Cyearly2000K110R14.dat
	4	10.835 ± 0.030	-	-	-	-	-	-											
	2.30×10^5	123.5 ± 8.7	-	-	-	-	-	-											
$\mathcal{M}=2$	$\mathcal{M}_{2,1,0,\chi^2}$	10.184 ± 0.064	10.813 ± 0.029	-	-	-	-	-	7	62.3 ± 6.8	1822.19 ± 0.64	$t_{\min,1}$ (y)	$t_{\min,1}$ (y)	$t_{\min,1}$ (y)	$t_{\min,1}$ (y)	21	24	21	Cyearly2000K210R14.dat
	7	10.184 ± 0.064	10.813 ± 0.029	-	-	-	-	-											
	1.68×10^5	62.3 ± 6.8	119.2 ± 8.5	-	-	-	-	-											
$\mathcal{M}=3$	$\mathcal{M}_{3,1,0,\chi^2}$	10.244 ± 0.059	10.780 ± 0.043	248 ± 1700 LP	-	-	-	-	10	70 ± 10	1821.62 ± 0.47	$t_{\min,1}$ (y)	$t_{\min,1}$ (y)	$t_{\min,1}$ (y)	$t_{\min,1}$ (y)	20	16	8.9	Cyearly2000K310R14.dat
	10	10.244 ± 0.059	10.780 ± 0.043	248 ± 1700 LP	-	-	-	-											
	1.24×10^5	70 ± 10	118 ± 10	51 ± 4300 AD	-	-	-	-											
$\mathcal{M}=4$	$\mathcal{M}_{4,1,0,\chi^2}$	10.217 ± 0.050	10.783 ± 0.037	99 ± 19	8100 ± 3600 LP	-	-	-	13	68 ± 12	1821.93 ± 0.48	$t_{\min,1}$ (y)	$t_{\min,1}$ (y)	$t_{\min,1}$ (y)	$t_{\min,1}$ (y)	18000 ± 14000 AD	$-$	$-$	Cyearly2000K410R14.dat
	13	10.217 ± 0.050	10.783 ± 0.037	99 ± 19	8100 ± 3600 LP	-	-	-											
	1.07×10^5	68 ± 12	119 ± 11	36.2 ± 8.0	18000 ± 14000 AD	-	-	-											

Table 28. Cyearly analysis for pure sinusoids ($K_2 = 1$). Otherwise as in Table 17.

\mathcal{M}	$\mathcal{M}_{K_1, K_2, K_3, \chi^2}$	Period analysis						Fisher-test			Control file	
		Data: Weighted original data ($n = 204, \Delta T = 203$: Cyearly.dat)						$\mathcal{M}=2$	$\mathcal{M}=3$	$\mathcal{M}=4$		
		P_1 (y)	P_2 (y)	P_3 (y)	P_4 (y)	A_1 (-)	A_2 (-)	A_3 (-)	A_4 (-)	F_R (-)	F_R (-)	
(1)	η (-)	$t_{\min,1}$ (y)	$t_{\min,1}$ (y)	$t_{\min,1}$ (y)	$t_{\min,1}$ (y)	(2)	(3)	(4)	(5)	(6)	(7)	Q_F (-)
χ^2 (-)												Q_F (-)
												(8)
												(9)
												(10)
$\mathcal{M}=1$	$\mathcal{M}_{1,1,0,\chi^2}$	10.832 ± 0.022	-	-	-	-	-	-	-	\uparrow	\uparrow	\uparrow
	4	123 ± 11	-	-	-	-	-	-	-	18	22	25
	2.55×10^5	1823.76 ± 0.29	-	-	-	-	-	-	-	1.5×10^{-10}	$< 10^{-16}$	$< 10^{-16}$
$\mathcal{M}=2$	$\mathcal{M}_{2,1,0,\chi^2}$	10.150 ± 0.042	10.854 ± 0.018	-	-	-	-	-	-	\uparrow	\uparrow	\uparrow
	7	55.0 ± 5.3	121.5 ± 9.1	-	-	-	-	-	-	20	22	$CyearlyK210R14.dat$
	1.99×10^5	1822.24 ± 0.50	1823.64 ± 0.22	-	-	-	-	-	-	1.5×10^{-11}	$< 10^{-16}$	
$\mathcal{M}=3$	$\mathcal{M}_{3,1,0,\chi^2}$	10.107 ± 0.031	10.863 ± 0.019	119.6 ± 5.6	-	-	-	-	-	-	\uparrow	
	10	59.7 ± 7.3	124.2 ± 6.5	51.7 ± 6.1	-	-	-	-	-	-	25	$CyearlyK310R14.dat$
	1.51×10^5	1822.93 ± 0.40	1823.51 ± 0.23	1907.6 ± 3.2	-	-	-	-	-	-	$< 10^{-16}$	
$\mathcal{M}=4$	$\mathcal{M}_{4,1,0,\chi^2}$	10.058 ± 0.026	10.863 ± 0.022	11.856 ± 0.068	115.6 ± 3.6	-	-	-	-	-	-	
	13	61.0 ± 9.6	119.3 ± 7.5	43.8 ± 7.9	53.8 ± 5.2	-	-	-	-	-	-	$CyearlyK410R14.dat$
	1.17×10^5	1823.55 ± 0.25	1823.56 ± 0.20	1818.95 ± 0.69	1910.4 ± 2.1	-	-	-	-	-	-	
Data: Weighted residuals of $\mathcal{M}=4$ ($n = 204, \Delta T = 203$: CyearlyK410R14Residuals.dat)												
								$\mathcal{M}=6$	$\mathcal{M}=7$	$\mathcal{M}=8$		
$\mathcal{M}=5$	$\mathcal{M}_{1,1,-1,\chi^2}$	8.005 ± 0.058	-	-	-	-	-	\uparrow	\uparrow	\uparrow		
	3	24.0 ± 7.0	-	-	-	-	-	6.4	6.4	6.4	$CyearlyK11-1R58.dat$	
	1.05×10^5	1826.09 ± 0.68	-	-	-	-	-	3.8×10^{-4}	3.4×10^{-6}	6.4×10^{-8}		
$\mathcal{M}=6$	$\mathcal{M}_{2,1,-1,\chi^2}$	8.002 ± 0.090	239 ± 86 LP	-	-	-	-	-	\uparrow	\uparrow		
UM	6	23.3 ± 5.0	22.5 ± 4.2	-	-	-	-	-	6.0	5.9	$CyearlyK21-1R58.dat$	
	9.57×10^4	1826.1 ± 1.1	1839.4 ± 28	-	-	-	-	-	6.4×10^{-4}	1.1×10^{-5}		
$\mathcal{M}=7$	$\mathcal{M}_{3,1,-1,\chi^2}$	7.998 ± 0.044	38.7 ± 2.1	253 ± 1700 LP	-	-	-	-	-	\leftarrow		
UM	9	24.5 ± 6.5	20.6 ± 6.8	22 ± 50 AD	-	-	-	-	-	5.4	$CyearlyK31-1R58.dat$	
	8.76×10^4	1826.19 ± 0.69	1856.3 ± 4.3	1875 ± 428	-	-	-	-	-	0.0013		
$\mathcal{M}=8$	$\mathcal{M}_{4,1,-1,\chi^2}$	7.991 ± 0.048	8.819 ± 0.070	48.7 ± 2.1	2400 ± 1700 LP	-	-	-	-	-		
UM	12	23.0 ± 7.0	20.7 ± 4.8	21.0 ± 4.8	22 ± 29 AD	-	-	-	-	-	$CyearlyK41-1R58.dat$	
	8.07×10^4	1826.03 ± 0.62	1819.3 ± 1.1	1824.1 ± 5.0	1842 ± 433	-	-	-	-	-		

A. Additional statements

Author Contribution L.J. analysed the data, prepared the figures and the tables, wrote the manuscript, as well as revised the manuscript.

Data Availability All analysed data are stored in Zenodo database <https://zenodo.org/uploads/11503698>.

Code Availability The Zenodo database <https://zenodo.org/uploads/11503698> also supplies our Discrete Chi-square Method (DCM) Python code. Our DCM manual gives full instructions for repeating the DCM analysis presented in Tables 17 - 28.

Declarations

Conflict of interest The author declares no competing interests.

References

Aguilar, L.M., Robledo-Sánchez, C., Carrasco, M.L., Otero, M.M.: 2012, The principle of superposition for waves: The amplitude and phase modulation phenomena. *Applied Mathematics and Information Sciences* **6**, 307.

Akhavan-Tafti, M., Slavin, J.A., Le, G., Eastwood, J.P., Strangeway, R.J., Russell, C.T., Nakamura, R., Baumjohann, W., Torbert, R.B., Giles, B.L., Gershman, D.J., Burch, J.L.: 2018, MMS Examination of FTEs at the Earth's Subsolar Magnetopause. *Journal of Geophysical Research (Space Physics)* **123**, 1224. [DOI](#). [ADS](#).

Alfvén, H.: 1942, On the cosmogony of the solar system. *Stockholms Observatoriums Annaler* **14**, 2.1. [ADS](#).

Allen, M.P.: 2004, *Understanding Regression Analysis*, Springer US, 113. ISBN 9780306484339. [URL](#).

Asikainen, T., Mantere, J.: 2023, Prediction of even and odd sunspot cycles. *arXiv e-prints*, arXiv:2309.04208. [DOI](#). [ADS](#).

Babcock, H.W.: 1961, The Topology of the Sun's Magnetic Field and the 22-Year Cycle. *Astrophys. J.* **133**, 572. [DOI](#). [ADS](#).

Bai, T.: 1987, Distribution of Flares on the Sun: Superactive Regions and Active Zones of 1980–1985. *Astrophys. J.* **314**, 795. [DOI](#). [ADS](#).

Baliunas, S.L., Vaughan, A.H.: 1985, Stellar activity cycles. *ARA&A* **23**, 379. [DOI](#). [ADS](#).

Bhowmik, P., Jiang, J., Upton, L., Lemerle, A., Nandy, D.: 2023, Physical Models for Solar Cycle Predictions. *Space Sci. Rev.* **219**, 40. [DOI](#). [ADS](#).

Birch, M.J., Bromage, B.J.I.: 2022, Sunspot numbers and proton events in solar cycles 19 to 24. *Journal of Atmospheric and Solar-Terrestrial Physics* **236**, 105891. [DOI](#). [ADS](#).

Biswas, A., Karak, B.B., Usoskin, I., Weisshaar, E.: 2023, Long-Term Modulation of Solar Cycles. *Space Sci. Rev.* **219**, 19. [DOI](#). [ADS](#).

Breger, M., Garrido, R., Handler, G., Wood, M.A., Shobbrook, R.R., Bischof, K.M., Rodler, F., Gray, R.O., Stankov, A., Martinez, P., O'Donoghue, D., Szabó, R., Zima, W., Kaye, A.B., Barban, C., Heiter, U.: 2002, 29 frequencies for the δ Scuti variable BI CMi: the 1997-2000 multisite campaigns. *Mon. Not. R. Astron. Soc.* **329**, 531. [DOI](#). [ADS](#).

Charbonneau, P.: 2010, Dynamo Models of the Solar Cycle. *Living Reviews in Solar Physics* **7**, 3. [DOI](#). [ADS](#).

Charbonneau, P.: 2022, External Forcing of the Solar Dynamo. *Frontiers in Astronomy and Space Sciences* **9**, 853676. [DOI](#). [ADS](#).

Cionco, R.G., Kudryavtsev, S.M., Soon, W.W.-H.: 2023, Tidal Forcing on the Sun and the 11-Year Solar-Activity Cycle. *Sol. Phys.* **298**, 70. [DOI](#). [ADS](#).

Cranmer, S.R., Saar, S.H.: 2007, Exoplanet-Induced Chromospheric Activity: Realistic Light Curves from Solar-type Magnetic Fields. *arXiv e-prints*, astro. [DOI](#). [ADS](#).

Cuntz, M., Saar, S.H., Musielak, Z.E.: 2000, On Stellar Activity Enhancement Due to Interactions with Extrasolar Giant Planets. *Astrophys. J. Lett.* **533**, L151. [DOI](#). [ADS](#).

DiBraccio, G.A., Slavin, J.A., Imber, S.M., Gershman, D.J., Raines, J.M., Jackman, C.M., Boardsen, S.A., Anderson, B.J., Korth, H., Zurbuchen, T.H., McNutt, R.L., Solomon, S.C.: 2015, MESSENGER observations of flux ropes in Mercury's magnetotail. *Planetary and Space Science* **115**, 77. [DOI](#). [ADS](#).

Dimitropoulou, M., Moussas, X., Strintzi, D.: 2008, Enhanced Rieger type periodicities' detection in X-ray solar flares and statistical validation of Rossby waves' existence. *Proceedings of the International Astronomical Union* **4**, 159–163. [DOI](#).

Draper, N.R., Smith, H.: 1998, *Applied Regression Analysis*, John Wiley & Sons, Inc. [DOI](#).

Dungey, J.W.: 1961, Interplanetary Magnetic Field and the Auroral Zones. *Phys. Rev. Lett.* **6**, 47. [DOI](#). [URL](#).

Efron, B., Tibshirani, R.: 1986, Bootstrap Methods for Standard Errors, Confidence Intervals, and Other Measures of Statistical Accuracy. *Statistical Science* **1**, 54.

Fear, R.C., Palmroth, M., Milan, S.E.: 2012, Seasonal and clock angle control of the location of flux transfer event signatures at the magnetopause. *Journal of Geophysical Research (Space Physics)* **117**, A04202. [DOI](#). [ADS](#).

Feth, L.L.: 1974, Frequency discrimination of complex periodic tones. *Perception & Psychophysics* **15**, 375.

Gillies, G.T.: 1997, The Newtonian gravitational constant: recent measurements and related studies. *Reports on Progress in Physics* **60**, 151. [DOI](#). [ADS](#).

Gleissberg, W.: 1945, Evidence for a long solar cycle. *The Observatory* **66**, 123. [ADS](#).

Glenn, G.S.: 2019, Mysterious High Energy Gamma Rays Might Help Explain What Drives Solar Cycles. *arXiv e-prints*, arXiv:1901.10574. [DOI](#). [ADS](#).

Gnevyshev, M.N., Ohl, A.I.: 1948, On the 22-year cycle of solar activity. *Astron. Zh.* **25**, 18.

Gurgenashvili, E., Zaqrashvili, T.V., Kukhianidze, V., Oliver, R., Ballester, J.L., Dikpati, M., McIntosh, S.W.: 2017, North-South Asymmetry in Rieger-type Periodicity during Solar Cycles 19-23. *Astrophys. J.* **845**, 137. [DOI](#). [ADS](#).

Hale, G.E., Ellerman, F., Nicholson, S.B., Joy, A.H.: 1919, The Magnetic Polarity of Sun-Spots. *Astrophys. J.* **49**, 153. [DOI](#). [ADS](#).

Handler, G.: 2003, Merging Data from Large and Small Telescopes – Good or Bad? And: How Useful is the Application of Statistical Weights to Time-Series Photometric Measurements? *Baltic Astronomy* **12**, 253. [DOI](#). [ADS](#).

Hansson, J.: 2022, The 11-Year Magnetic Solar Cycle: Chaos Control Due to Jupiter. *Solar System Research* **56**, 191. [DOI](#). [ADS](#).

Hantzsche, E.: 1978, On the Tidal Theory of Solar Activity. *Astronomische Nachrichten* **299**, 259. [DOI](#). [ADS](#).

Hasegawa, H., Sonnerup, B.U.Ö., Eriksson, S., Nakamura, T.K.M., Kawano, H.: 2015, Dual-spacecraft reconstruction of a three-dimensional magnetic flux rope at the Earth's magnetopause. *Annales Geophysicae* **33**, 169. [DOI](#). [ADS](#).

Horne, J.H., Baliunas, S.L.: 1986, A Prescription for Period Analysis of Unevenly Sampled Time Series. *Astrophys. J.* **302**, 757. [DOI](#). [ADS](#).

Ip, W.-H., Kopp, A., Hu, J.-H.: 2004, On the Star-Magnetosphere Interaction of Close-in Exoplanets. *Astrophys. J. Lett.* **602**, L53. [DOI](#). [ADS](#).

Javaaraiah, J.: 2023, Prediction for the amplitude and second maximum of Solar Cycle 25 and a comparison of the predictions based on strength of polar magnetic field and low-latitude sunspot area. *Mon. Not. R. Astron. Soc.* **520**, 5586. [DOI](#). [ADS](#).

Jayalekshmi, G.L., Pant, T.K., Prince, P.R.: 2022, Sunspot-Cycle Evolution of Major Periodicities of Solar Activity. *Sol. Phys.* **297**, 85. [DOI](#). [ADS](#).

Jenkins, J.M., Twicken, J.D., Batalha, N.M., Caldwell, D.A., Cochran, W.D., Endl, M., Latham, D.W., Esquerdo, G.A., Seader, S., Bieryla, A., Petigura, E., Ciardi, D.R., Marcy, G.W., Isaacson, H., Huber, D., Rowe, J.F., Torres, G., Bryson, S.T., Buchhave, L., Ramirez, I., Wolfgang, A., Li, J., Campbell, J.R., Tenenbaum, P., Sanderfer, D., Henze, C.E., Catanzarite, J.H., Gilliland, R.L., Borucki, W.J.: 2015, Discovery and Validation of Kepler-452b: A 1.6 R_\oplus Super Earth Exoplanet in the Habitable Zone of a G2 Star. *Astron. J.* **150**, 56. [DOI](#). [ADS](#).

Jephcoat, A., Olson, P.: 1987, Is the inner core of the Earth pure iron? *Nature* **325**, 332. [DOI](#). [ADS](#).

Jetsu, L.: 2020, Discrete Chi-square Method for Detecting Many Signals. *The Open Journal of Astrophysics* **3**, 4. [DOI](#). [ADS](#).

Jetsu, L.: 2021, Say Hello to Algol's New Companion Candidates. *Astrophys. J.* **920**, 137. [DOI](#). [ADS](#).

Jetsu, L., Pelt, J.: 1999, Three stage period analysis and complementary methods. *Astron. Astrophys. Suppl.* **139**, 629. [DOI](#). [ADS](#).

Jetsu, L., Pohjolainen, S., Pelt, J., Tuominen, I.: 1997, Is the longitudinal distribution of solar flares nonuniform? *Astron. Astrophys.* **318**, 293. [ADS](#).

Kivelson, M.G., Bagenal, F.: 2007, Planetary Magnetospheres. In: McFadden, L.-A.A., Weissman, P.R., Johnson, T.V. (eds.) *Encyclopedia of the Solar System*, 519. [DOI](#). [ADS](#).

Komitov, B., Kaftan, V.: 2004, The Sunspot Activity in the Last Two Millenia on the Basis of Indirect and Instrumental Indexes: Time Series Models and Their Extrapolations for the 21st Century. In: Stepanov, A.V., Benevolenskaya, E.E., Kosovichev, A.G. (eds.) *Multi-Wavelength Investigations of Solar Activity* **223**, 113. [DOI](#). [ADS](#).

Korhonen, H., Andersen, J.M., Piskunov, N., Hackman, T., Juncher, D., Järvinen, S.P., Jørgensen, U.G.: 2015, Stellar activity as noise in exoplanet detection - I. Methods and application to solar-like stars and activity cycles. *Mon. Not. R. Astron. Soc.* **448**, 3038. [DOI](#). [ADS](#).

Krasheninnikov, I.V., Chumakov, S.O.: 2023, Predicting the Functional Dependence of the Sunspot Number in the Solar Activity Cycle Based on Elman Artificial Neural Network. *Geomagnetism and Aeronomy* **63**, 215. [DOI](#). [ADS](#).

Ku, J.G., Liu, X.Y., Chen, H.H., Deng, R.D., Yan, Q.X.: 2016, Interaction between two magnetic dipoles in a uniform magnetic field. *AIP Advances* **6**, 025004. [DOI](#). [URL](#).

Lassen, K., Friis-Christensen, E.: 1995, Variability of the solar cycle length during the past five centuries and the apparent association with terrestrial climate. *Journal of Atmospheric and Terrestrial Physics* **57**, 835. [DOI](#). [ADS](#).

Lehtinen, J., Jetsu, L., Hackman, T., Kajatkari, P., Henry, G.W.: 2011, The continuous period search method and its application to the young solar analogue HD 116956. *Astron. Astrophys.* **527**, A136. [DOI](#). [ADS](#).

Leighton, R.B.: 1969, A Magneto-Kinematic Model of the Solar Cycle. *Astrophys. J.* **156**, 1. [DOI](#). [ADS](#).

Li, J.: 2018, A Systematic Study of Hale and Anti-Hale Sunspot Physical Parameters. *Astrophys. J.* **867**, 89. [DOI](#). [ADS](#).

Lockwood, M., Wild, M.N.: 1993, On the quasi-periodic nature of magnetopause flux transfer events. *J. Geophys. Res.* **98**, 5935. [DOI](#). [ADS](#).

Loumos, G.L., Deeming, T.J.: 1978, Spurious results from Fourier analysis of data with closely spaced frequencies. *Astrophys. Space Sci.* **56**, 285. [DOI](#). [ADS](#).

Luminița, D., Laurențiu, N.E., Constantina, F.: 2023, The use of Ap geomagnetic indices for the characterization and ranking of major geomagnetic disturbances from 1932 to 2022. *Oltenia, Studii si Comunicari Seria Stiintele Naturii* **39**.

Macdonald, L.: 2012, *How to Observe the Sun Safely*. [DOI](#). [ADS](#).

Muñoz, J.M., Wagemakers, A., Sanjuán, M.A.F.: 2023, Planetary influences on the solar cycle: A nonlinear dynamics approach. *Chaos* **33**, 123102. [DOI](#). [ADS](#).

Murphy, S.J.: 2012, Kepler Fourier concepts: The performance of the Kepler data pipeline. *Astronomische Nachrichten* **333**, 1057. [DOI](#). [ADS](#).

Nakariakov, V.M., Pilipenko, V., Heilig, B., Jelínek, P., Karlický, M., Klimushkin, D.Y., Kolotkov, D.Y., Lee, D.-H., Nisticò, G., Van Doorsselaere, T., Verth, G., Zimovets, I.V.: 2016, Magnetohydrodynamic Oscillations in the Solar Corona and Earth's Magnetosphere: Towards Consolidated Understanding. *Space Sci. Rev.* **200**, 75. [DOI](#). [ADS](#).

Ohtomo, N., Terachi, S., Tanaka, Y., Tokiwano, K., Kaneko, N.: 1994, New Method of Time Series Analysis and Its Application to Wolf's Sunspot Number Data. *Japanese Journal of Applied Physics* **33**, 2821. [DOI](#). [ADS](#).

Parker, E.N.: 1955, Hydromagnetic Dynamo Models. *Astrophys. J.* **122**, 293. [DOI](#). [ADS](#).

Parker, E.N.: 1958, Dynamics of the Interplanetary Gas and Magnetic Fields. *Astrophys. J.* **128**, 664. [DOI](#). [ADS](#).

Paul, A., Vaidya, B., Strugarek, A.: 2022, A Volumetric Study of Flux Transfer Events at the Dayside Magnetopause. *Astrophys. J.* **938**, 130. [DOI](#). [ADS](#).

Pease, G.E., Glenn, G.S.: 2016, Long Term Sunspot Cycle Phase Coherence with Periodic Phase Disruptions. *arXiv e-prints*, arXiv:1610.03553. [DOI](#). [ADS](#).

Petrovay, K.: 2020, Solar cycle prediction. *Living Reviews in Solar Physics* **17**, 2. [DOI](#). [ADS](#).

Phan, T.-D., Paschmann, G., Baumjohann, W., Sckopke, N., Luehr, H.: 1994, The magnetosheath region adjacent to the dayside magnetopause: AMPTE/IRM observations. *J. Geophys. Res.* **99**, 121. [DOI](#). [ADS](#).

Raeder, J.: 2006, Flux Transfer Events: 1. generation mechanism for strong southward IMF. *Annales Geophysicae* **24**, 381. [DOI](#). [ADS](#).

Reegen, P.: 2007, SigSpec. I. Frequency- and phase-resolved significance in Fourier space. *Astron. Astrophys.* **467**, 1353. [DOI](#). [ADS](#).

Rieger, E., Kanbach, G., Reppin, C., Share, G.H., Forrest, D.J., Chupp, E.L.: 1984, A 154-day periodicity in the occurrence of hard solar flares? *Nature* **312**, 623. [DOI](#). [ADS](#).

Rijnbeek, R.P., Cowley, S.W.H., Southwood, D.J., Russell, C.T.: 1984, A survey of dayside transfer events observed by ISEE 1 and 2 magnetometers. *J. Geophys. Res.* **89**, 786. [DOI](#). [ADS](#).

Rodríguez, E., Costa, V., Handler, G., García, J.M.: 2003, Simultaneous uvby photometry of the new delta Sct-type variable HD 205. *Astron. Astrophys.* **399**, 253. [DOI](#). [ADS](#).

Russell, C.T.: 1995, A study of flux transfer events at different planets. *Advances in Space Research* **16**, 159. [DOI](#). [ADS](#).

Russell, C.T.: 2003, The structure of the magnetopause. *Planetary and Space Science* **51**, 731. [DOI](#). [ADS](#).

Rutkowski, L.: 2014, Symmetry and asymmetry as a physical and perceptual feature of the complementary pair of bearing sinusoids. Part I. Amplitude and frequency envelope relations. *Archives of Acoustics* **23**, 51.

Sarkango, Y., Slavin, J.A., Jia, X., DiBraccio, G.A., Gershman, D.J., Connerney, J.E.P., Kurth, W.S., Hospodarsky, G.B.: 2021, Juno Observations of Ion-Inertial Scale Flux Ropes in the Jovian Magnetotail. *Geophys. Res. Lett.* **48**, e89721. [DOI](#). [ADS](#).

Sarkango, Y., Slavin, J.A., Jia, X., DiBraccio, G.A., Clark, G.B., Sun, W., Mauk, B.H., Kurth, W.S., Hospodarsky, G.B.: 2022, Properties of Ion-Inertial Scale Plasmoids Observed by the Juno Spacecraft in the Jovian Magnetotail. *Journal of Geophysical Research (Space Physics)* **127**, e30181. [DOI](#). [ADS](#).

Scafetta, N., Bianchini, A.: 2022, The Planetary Theory of Solar Activity Variability: A Review. *Frontiers in Astronomy and Space Sciences* **9**, 937930. [DOI](#). [ADS](#).

Scargle, J.D.: 1982, Studies in astronomical time series analysis. II - Statistical aspects of spectral analysis of unevenly spaced data. *Astrophys. J.* **263**, 835. [DOI](#). [ADS](#).

Schubert, G., Soderlund, K.M.: 2011, Planetary magnetic fields: Observations and models. *Physics of the Earth and Planetary Interiors* **187**, 92. [DOI](#). [ADS](#).

Schuster, A.: 1911, The Influence of Planets on the Formation of Sun-Spots. *Proceedings of the Royal Society of London Series A* **85**, 309. [DOI](#). [ADS](#).

Schwabe, M.: 1844, Sonnenbeobachtungen im Jahre 1843. Von Herrn Hofrat Schwabe in Dessau. *Astronomische Nachrichten* **21**, 233. [ADS](#).

Schwär, S., Müller, M., Schlecht, S.: 2023, Modifying Partials for Minimum-Roughness Sound Synthesis. In: *Proceedings of Timbre 2023, 3rd International Conference on Timbre, Thessaloniki, Greece*, 1.

Scurry, L., Russell, C.T., Gosling, J.T.: 1994, A statistical study of accelerated flow events at the dayside magnetopause. *J. Geophys. Res.* **99**, 14,815. [DOI](#) [ADS](#).

Slavin, J.A., Lepping, R.P., Wu, C.-C., Anderson, B.J., Baker, D.N., Benna, M., Boardsen, S.A., Killen, R.M., Korth, H., Krimigis, S.M., McClintock, W.E., McNutt, R.L., Sarantos, M., Schriver, D., Solomon, S.C., Trávníček, P., Zurbuchen, T.H.: 2010, MESSENGER observations of large flux transfer events at Mercury. *Geophys. Res. Lett.* **37**, L02105. [DOI](#) [ADS](#).

Slavin, J.A., Anderson, B.J., Baker, D.N., Benna, M., Boardsen, S.A., Gold, R.E., Ho, G.C., Imber, S.M., Korth, H., Krimigis, S.M., McNutt, J. Ralph L., Raines, J.M., Sarantos, M., Schriver, D., Solomon, S.C., Trávníček, P., Zurbuchen, T.H.: 2012, MESSENGER and Mariner 10 flyby observations of magnetotail structure and dynamics at Mercury. *Journal of Geophysical Research (Space Physics)* **117**, A01215. [DOI](#) [ADS](#).

Stefani, F., Giesecke, A., Weier, T.: 2019, A Model of a Tidally Synchronized Solar Dynamo. *Sol. Phys.* **294**, 60. [DOI](#) [ADS](#).

Sun, W., Slavin, J.A., Nakamura, R., Heyner, D., Trattner, K.J., Mieth, J.Z.D., Zhao, J., Zong, Q.-G., Aizawa, S., Andre, N., Saito, Y.: 2022, Dayside magnetopause reconnection and flux transfer events under radial interplanetary magnetic field (IMF): BepiColombo Earth-flyby observations. *Annales Geophysicae* **40**, 217. [DOI](#) [ADS](#).

Usoskin, I.G., Solanki, S.K., Kovaltsov, G.A.: 2007, Grand minima and maxima of solar activity: new observational constraints. *Astron. Astrophys.* **471**, 301. [DOI](#) [ADS](#).

Van Geel, B., Raspovov, O., Renssen, H., Van der Plicht, J., Dergachev, V., Meijer, H.: 1999, The role of solar forcing upon climate change. *Quaternary Science Reviews* **18**, 331.

Vasil, G., Lecoanet, D., Augustson, K., Burns, K., Oishi, J., Brown, B., Brummell, N., Julien, K.: 2024, The solar dynamo begins near the surface. *Nature* **629**, 769. [DOI](#).

Vaughan, S.: 2005, A simple test for periodic signals in red noise. *Astron. Astrophys.* **431**, 391. [DOI](#) [ADS](#).

Vogt, M.F., Jackman, C.M., Slavin, J.A., Bunce, E.J., Cowley, S.W.H., Kivelson, M.G., Khurana, K.K.: 2014, Structure and statistical properties of plasmoids in Jupiter's magnetotail. *Journal of Geophysical Research (Space Physics)* **119**, 821. [DOI](#) [ADS](#).

Wagner, G., Beer, J., Masarik, J., Muscheler, R., Kubik, P.W., Mende, W., Laj, C., Raisbeck, G.M., Yiou, F.: 2001, Presence of the Solar de Vries Cycle (\sim 205 years) during the Last Ice Age. *Geophys. Res. Lett.* **28**, 303. [DOI](#) [ADS](#).

Weisshaar, E., Cameron, R.H., Schüssler, M.: 2023, No evidence for synchronization of the solar cycle by a “clock”. *Astron. Astrophys.* **671**, A87. [DOI](#) [ADS](#).

Wolf, R.: 1852, Bericht über neue Untersuchungen über die Periode der Sonnenflecken und ihrer Bedeutung von Herrn Prof. Wolf. *Astronomische Nachrichten* **35**, 369. [DOI](#) [ADS](#).

Wolf, R.: 1859, Extract of a Letter to Mr. Carrington. *Mon. Not. R. Astron. Soc.* **19**, 85. [DOI](#) [ADS](#).

Xiang, N.B., Ning, Z.J., Li, F.Y.: 2020, Temporal Evolution of the Rotation of the Interplanetary Magnetic Field B_x , B_y , and B_z Components. *Astrophys. J.* **896**, 12. [DOI](#) [ADS](#).

Zhang, H., Zong, Q., Connor, H., Delamere, P., Facskó, G., Han, D., Hasegawa, H., Kallio, E., Kis, Á., Le, G., Lembège, B., Lin, Y., Liu, T., Oksavik, K., Omidi, N., Otto, A., Ren, J., Shi, Q., Sibeck, D., Yao, S.: 2022, Dayside Transient Phenomena and Their Impact on the Magnetosphere and Ionosphere. *Space Sci. Rev.* **218**, 40. [DOI](#) [ADS](#).

Zhu, F.R., Jia, H.Y.: 2018, Lomb-Scargle periodogram analysis of the periods around 5.5 year and 11 year in the international sunspot numbers. *Astrophys. Space Sci.* **363**, 138. [DOI](#) [ADS](#).